Membrane Potential Dynamics of Hippocampal Neurons During Ripples in Awake Mice

Brad K. Hulse

In Partial Fulfillment of the Requirements
for the Degree of
Doctor of Philosophy

California Institute of Technology
Pasadena, California

2017
Defended November 14th, 2016

To my parents, Steve and Lori Hulse.

Acknowledgements

Graduate school has been a phenomenally transformative experience, and I am deeply indebted to the amazing people responsible. I'd like to thank my advisor, Thanos Siapas, for performing the science that first attracted me to Caltech and for providing me with an intellectual home when I had none. Your experiment-driven mentality, analytical rigor, and undying skepticism were the primary drivers of my scientific development, and the kindness and respect you show people is inspirational. For your guidance and mentorship, thank you Professors David Prober, Henry Lester, Christof Koch, Michael Dickinson, and Paul Sternberg. Thank you David Prober, for a great rotation experience and professional support; Henry Lester, for showing me the ropes during my first year, sharing your teaching expertise, and providing me with scientific feedback over the years; Christof Koch, for opening your lab to me; and Michael Dickinson and Paul Sternberg, for your sound advice and encouragement. To my undergraduate mentors, Giulio Tononi, Chiara Cirelli, Eric Landsness, and Brady Riedner, thanks for your support and for introducing me to the joys of neuroscience.

To my labmates and collaborators, thanks for being generous with your time, providing critical and insightful feedback, and creating an enjoyable lab culture. Thank you Eugene Lubenov, my main collaborator on this work, for sharing your knowledge of extracellular recordings, for outstanding scientific guidance, for possessing an inspirational clarity of thought, and for many wonderful pontoon-related discussions; Laurent Moreaux, my experimental mentor, for teaching me the importance of working cleanly, the art of scavenging, the beauty of imaging, and how to stay on the rock (and, most importantly, thanks for braving the experimental trenches with me and Johnny Cash); Andreas Tolias

and Jake Reimer, for help with the head-fixed preparation; Jonathan Bradley, for showing me around Paris in style; the ENP spring school, for a great experience and kindling my obsession with access resistance; Mike Walsh, for your unmatched inventiveness and professionalisms; Koichiro Kajikawa, my experimental collaborator, for your imperturbable calm, candor, and for leaving a few unpatched neurons for the rest of us; Stijn Cassenaer, for your inspiring experimental prowess, beautiful science, professional guidance, and characteristic humor; Andreas Hoenselaar, for computer whispering, instrumentation support, software development, your desk chair, and for starting our lunch tradition; Maria Papadopoulou, for advice on immunohistochemistry, lab comradery, and your infectious energy; Jenn Mok, for help with tissue processing and many laughs; Gustavo Rios, for an engineer's perspective on life and science; Britton Sauerbrei, for your contagious passion, outrageous sense of style, scholarly pursuits, and for proving that everything's fine; and Kevin Shan, for your company at lunch, honest and detailed feedback, computer whispering, solidarity, and knowledge of Morse code. This thesis would not have been possible without my closest colleagues and stars of the show, the mice, to whom I am very grateful.

Finally, I'd like to thank my amazing friends and family for their continuous love and support. To Alyson Weidmann, thank you for your unmatched wisdom, patience, uplifting sense of humor, and many fascinating octopus- and rabies-related discussions; Guy Edouard, for going as hard in the paint and as you do in life and lab; Khai Chiong, for sharing your perspective on life and being a great friend; and Red, for good company. To my grandmothers, Marilyn Kline and Doreen Hulse, thanks for reminding me of what matters most; to my parents, Steve and Lori Hulse, for providing me with the freedom and encouragement to pursue my chosen path and instilling me with the work ethic required to

follow it; my brother, Jake Franklin, for teaching me when to put up a fight, when to take flight, and when to ask for help (thanks again, Mom); my sister, Sara Franklin, for humbling documentary photography; my nephew, Andrew Sachs, for your undeniable swagger; my sister-in-law, Leah Franklin, for demonstrating the power of reason over the unreasonable; and my nieces, for perspective. One of my few regrets in moving away for graduate school is that I couldn't see you grow up in real time.

Abstract

During periods of slow wave sleep and quiet wakefulness, the hippocampal formation generates spontaneous population bursts that are organized as a high-frequency "ripple" oscillation. The neurons that participate in these bursts often replay previously experienced activity patterns encoded during alert behavior, and interfering with ripple generation produces deficits in learning and memory tasks. For these reasons, ripples play a prominent role in theories of memory consolidation and retrieval. While spiking during ripples has been extensively studied, our understanding of the subthreshold behavior of hippocampal neurons during these events remains incomplete. Here, we combine in vivo whole-cell recordings with multisite extracellular and behavioral measurements to study the membrane potential dynamics of hippocampal neurons during ripples in awake mice. We find that the subthreshold depolarization of CA1 pyramidal neurons is uncorrelated with net excitatory input, clarifying the circuit mechanism keeping most neurons silent during ripples. On a finer time scale, the phase delay between intracellular and extracellular ripple oscillations varies systematically with the membrane potential, which is inconsistent with models of intracellular ripple generation involving perisomatic inhibition alone. In addition, we find that membrane potential statistics (mean, variability, distance to threshold) of CA1 pyramidal neurons and dentate granule cells are systematically modulated across brain states, that rapid variations in pupil diameter are reflected in subthreshold fluctuations, and that many neurons begin depolarizing about one second before ripple onset. These results provide evidence that coordinated shifts in the subthreshold dynamics of individual neurons may contribute to the emergence of state-dependent hippocampal activity patterns. Finally, we present evidence that area CA3 provides the major excitatory input to dentate granule cells

during ripples and that there are coordinated interactions between hippocampal ripples and population events in the dentate gyrus, both of which inform network-level models of ripple generation.

Published Content and Contributions

Chapter 2 has been modified from a previously published manuscript (Hulse et al., 2016). Manuscripts based on Chapters 3 and 4 are in submission and preparation, respectively. In all studies, I contributed to experimental design, data collection and analysis, modeling, interpretation of results, figure design, and writing.

Hulse, B. K., Moreaux, L. C., Lubenov, E. V. Siapas, A. G. (2016). Membrane Potential Dynamics of CA1 Pyramidal Neurons during Hippocampal Ripples in Awake Mice. Neuron. 89, 800-13. DOI: 10.1016/j.neuron.2016.01.014

B.K.H. contributed to experimental design, data collection and analysis, modeling, interpretation of results, figure design, and writing.

Contents

List of Figures

1 Introduction

The hippocampal formation plays a critical role for the encoding, consolidation, and initial retrieval of episodic memories (Squire, 1992). However, over time, memories are gradually transferred to distributed neocortical circuits. While the neuronal mechanisms remain poorly understood, each of these mnemonic functions is likely subserved by hippocampal activity patterns characteristic of different brain states (Buzsaki, 1989). During periods of slow wave sleep and quiet wakefulness, the hippocampus generates spontaneous populations bursts, known as sharp-wave/ripples (SWRs)(O'Keefe, 1976, O'Keefe and Nadel, 1978, Buzsaki et al., 1983). These population bursts produce coordinated output within the windows of synaptic integration and plasticity, and powerfully entrain downstream brain regions, including the neocortex (Chrobak and Buzsaki, 1996, Siapas and Wilson, 1998, Wierzynski et al., 2009, Logothetis et al., 2012). Intriguingly, the neurons that participate in these bursts often "replay" previously experienced activity patterns encoded during alert behavior (Wilson and McNaughton, 1994b, Lee and Wilson, 2002, Foster and Wilson, 2006, Diba and Buzsaki, 2007), and interfering with their generation produces deficits in learning and memory tasks (Girardeau et al., 2009, Ego-Stengel and Wilson, 2010, Jadhav et al., 2012). For these reasons, SWRs are key players in memory consolidation and retrieval (Diekelmann and Born, 2010, Carr et al., 2011, Buzsaki, 2015).

The function of the hippocampal formation, including in SWR generation, depends upon the architecture of its microcircuits and how they are interconnected (Andersen, 2007). Despite over a century of investigation, the neuroanatomy of the hippocampus is still being worked out. However, several general observations have emerged. First, the hippocampal

formation is a predominantly unidirectional, feed-forward network composed of several subregions: the entorhinal cortex, dentate gyrus, areas CA3 to CA1, and subicular complex. The entorhinal cortex serves as the main relay between the hippocampus and neocortex. It receives multimodal sensory information through its recurrent connections with higher-order neocortical associational areas and sends excitatory projections from its superficial layers to the dentate gyrus and areas CA3-CA1. The principal neurons of the dentate gyrus are known as dentate granule cells. Granule cells receive excitatory projections from entorhinal cortex and make powerful, excitatory synapses onto CA3 pyramidal neurons. CA3 pyramidal neurons, in turn, send excitatory projections to CA1 pyramidal neurons. CA1 pyramidal neurons send excitatory projections to the subicular complex, medial prefrontal cortex, deep layers of entorhinal cortex, and a few other structures, and serve as the main output of the hippocampus. While such feed-forward projections are the rule, there are exceptions. For example it is known that CA3 pyramidal neurons can project back to dentate granule cells, either directly or through mossy cells (Scharfman, 2007).

A second general observation is that hippocampal principal neurons differ in their overall numbers, firing rates, and recurrent connections across subregions. For example, in the rat, there are about 1,200,000 million dentate granule cells, 250,000 CA3 pyramidal neurons, and 390,000 CA1 pyramidal neurons (Andersen, 2007). In addition to their large numbers, dentate granule cells are known to fire very sparsely in vivo compared to their CA3 and CA1 counterparts (Kowalski et al., 2016). Moreover, while granule cells and CA1 pyramidal neurons are thought to have relatively sparse recurrent connections, CA3 pyramidal neurons connect to one another with a higher probability, forming a recurrent network (Miles and Wong, 1986, Le Duigou et al., 2014). Such differences have inspired influential conceptual

models of hippocampal function (Marr, 1971, Mcnaughton and Morris, 1987). Due to their low firing rates and large numbers, granule cells are thought to support pattern separation, such that two similar inputs from entorhinal cortex are represented by different subsets of granule cells. Because of its recurrent connectivity, area CA3 is thought to support pattern completion, whereby the activation of a few pyramidal cells allows the network to recall previously stored patterns. Pattern completion is thought to underlie SWR-associated replay in support of memory consolidation and retrieval. Finally, area CA1 is thought to readout CA3 activity, amplify it, and broadcast it to downstream brain regions.

Third, in addition to principal cells, there exists a plethora of inhibitory interneurons that provide feed-forward and feed-back inhibition to specific principal cell domains (Freund and Buzsaki, 1996). These interneurons are thought to be particularly important for the generation of state-dependent network oscillations, including SWRs, in addition to keeping excitation and inhibition approximately balanced (Isaacson and Scanziani, 2011, Somogyi et al., 2014). Forth, and finally, the hippocampal formation receives neuromodulatory input from many subcortical nuclei, such as the medial septum and median raphe, which release acetylcholine and serotonin, respectively. This neuromodulatory input is thought to support state-dependent activity patterns in the hippocampus (Saper et al., 2010, Lee and Dan, 2012, Teles-Grilo Ruivo and Mellor, 2013).

Importantly, most of what is known about the activity of hippocampal neurons and circuits in vivo comes from experiments that employ extracellular electrical recording techniques. Extracellular recordings monitor neuronal activity by measuring the electrical potential from an electrode positioned nearby, but still outside, neurons of interest, relative to a reference electrode often placed far away (Nunez and Srinivasan, 2006, Buzsaki et

al., 2012). The signal that is obtained is composed of two components. First, the high-frequency content of the signal (above ∼600 Hz) reflects neuronal spiking and allows for the monitoring of individual action potentials from individual neurons. Second, the low-frequency content of the signal (below ∼250 Hz) is known as the local field potential (LFP) and mostly reflects synaptic currents. The major benefit of this technique is that it allows for the stable measurement of neuronal activity from awake and naturally sleeping animals across many days and even months with high temporal resolution. Using this technique, early experiments established that different behavioral states are characterized by distinct LFP patterns. For example, during periods of active wakefulness and rapid eye movement (REM) sleep, continuous 5-12 Hz oscillations appear in the LFP, known as theta oscillations (Vanderwolf, 1969). In contrast, periods of slow wave sleep and quiet wakefulness are characterized by intermittent SWRs: large amplitude sharp waves occasionally accompanied by high-frequency (80-250 Hz) "ripple" oscillations lasting 50-100 ms (O'Keefe and Nadel, 1978). With further technical development, experimenters began using microelectrodes, wire bundles (stereotrodes, tetrodes, etc.), and multi-site silicone probes to record the spiking activity individual neurons, in addition to LFPs (O'Keefe and Dostrovsky, 1971, Buzsaki et al., 1983, Mcnaughton et al., 1983, Buzsaki et al., 1992, Wilson and Mcnaughton, 1994a). Using this technique, pioneering work discovered that, during theta-associated locomotor periods, individual hippocampal principal cells fire at particular spatial locations in a given environment and were termed "place cells" (O'Keefe and Nadel, 1978). Later, it was shown that place-cell sequences generated during active wakefulness are replayed, in both forward and reverse order, during periods of slow wave sleep and quiet wakefulness as part of the SWR-associated population burst (Wilson and McNaughton, 1994b, Lee and Wilson, 2002,

Foster and Wilson, 2006, Diba and Buzsaki, 2007). While extracellular recordings have provided a wealth of information regarding the spiking output of hippocampal neurons in vivo, these recordings provide very little insight into how these neurons process their inputs to generate an output.

Intracellular recordings of the neuronal membrane potential in vivo can address this. Intracellular "whole-cell" recordings use glass pipettes filled with a cytoplasm-mimicking solution to first form a tight seal with the neuronal membrane and then rupture a small whole in it, which provides electrical access to the inside of the neuron. These recordings allow for direct measurement of neuronal subthreshold activity, reflecting synaptic input, as well as the spiking output. Importantly, such recordings have only recently become feasible in awake animals (Steriade et al., 2001, Margrie et al., 2002, Lee et al., 2006). Previous to this, in vivo intracellular recordings from hippocampal neurons were performed in anesthetized animals (Kandel and Spencer, 1961, Kandel et al., 1961, Spencer and Kandel, 1961a, Spencer and Kandel, 1961b, Soltesz et al., 1993, Soltesz and Deschenes, 1993, Ylinen et al., 1995, Penttonen et al., 1997, Kamondi et al., 1998, Kowalski et al., 2016). However, using an anesthetized preparation prevents the study of awake behavior and its associated neuronal activity patterns. To overcome this, recent studies have performed intracellular recordings from hippocampal neurons in awake animals, mostly to study spatial processing during locomotion (Harvey et al., 2009, Lee et al., 2009, Epsztein et al., 2010, Epsztein et al., 2011, Lee et al., 2012, Domnisoru et al., 2013, Schmidt-Hieber and Hausser, 2013, Bittner et al., 2015).

In comparison, few studies have measured the membrane potential dynamics of hippocampal neurons during SWRs in awake animals, which is the subject of this dissertation

(Maier et al., 2011, English et al., 2014). Chapter 2 characterizes the subthreshold activity of CA1 pyramidal neurons during SWRs and discusses the implications for circuit models of ripple generation. Chapter 3 is concerned with the state-dependent patterns of subthreshold activity in CA1 pyramidal neurons and dentate granule cells and provides evidence that coordinated shifts in the membrane potential dynamics of individual neurons support hippocampal activity patterns characteristic of different brain states. Finally, Chapter 4 describes the membrane potential dynamics of dentate granule cells during SWRs and provides evidence for coordinate interactions between SWRs and dentate LFP spikes during quiet wakefulness.

2 Membrane Potential Dynamics of CA1 Pyramidal Neurons During Hippocampal Ripples in Awake Mice

2.1 Summary

Ripples are high-frequency oscillations associated with population bursts in area CA1 of the hippocampus that play a prominent role in theories of memory consolidation. While spiking during ripples has been extensively studied, our understanding of the subthreshold behavior of hippocampal neurons during these events remains incomplete. Here, we combine in vivo whole-cell and multisite extracellular recordings to characterize the membrane potential dynamics of identified CA1 pyramidal neurons during ripples. We find that the subthreshold depolarization during ripples is uncorrelated with the net excitatory input to CA1, while the post-ripple hyperpolarization varies proportionately. This clarifies the circuit mechanism keeping most neurons silent during ripples. On a finer time scale, the phase delay between intracellular and extracellular ripple oscillations varies systematically with membrane potential. Such smoothly varying delays are inconsistent with models of intracellular ripple generation involving perisomatic inhibition alone. Instead, they suggest that ripple-frequency excitation leading inhibition shapes intracellular ripple oscillations.

2.2 Introduction

The hippocampal formation plays a critical role for the encoding, consolidation, and retrieval of new episodic memories (Squire, 1992), but the underlying neuronal mechanisms remain elusive. During quiet wakefulness and slow-wave sleep, brief (50-100 ms), high-frequency (80-250 Hz) ripple oscillations appear in the local field potential (LFP) and are

associated with the near-synchronous discharge of principal cells (O'Keefe, 1976, Buzsaki et al., 1983). These population bursts produce coordinated output within the windows of synaptic integration and plasticity, powerfully entrain downstream brain regions, and are believed to contribute to the gradual establishment of memory representations across distributed neocortical circuits (Buzsaki, 1989, Chrobak and Buzsaki, 1996, Siapas and Wilson, 1998, Wierzynski et al., 2009, Diekelmann and Born, 2010, Carr et al., 2011, Logothetis et al., 2012, Buzsaki, 2015).

The circuit mechanisms generating ripple events have been the subject of much inquiry. The predominant conjecture is that hippocampal ripples are spontaneously initiated within the recurrent CA3 network. A population burst in CA3 provides excitatory input onto the dendrites of CA1 pyramidal cells, producing an intracellular depolarization and an associated negative sharp wave in the LFP of stratum radiatum (Buzsaki, 1986, Ylinen et al., 1995). Consequently, the amplitude of the LFP sharp wave correlates with the magnitude of net excitatory input to CA1. In support of this, the depth profile and pharmacological dependence of spontaneous sharp waves are very similar to field EPSPs evoked by stimulation of the Schaffer collaterals (Buzsaki, 1984, Buzsaki, 2015). The amplitude and slope of field EPSPs have been used extensively as a proxy for synaptic strength, since their size correlates with the magnitude of the synaptic currents and the number of activated input fibers (Bliss and Collingridge, 1993). Similarly, previous slice work has reported a correlation between the size of spontaneous sharp waves and the amplitude of excitatory currents in CA1 pyramidal cells (Mizunuma et al., 2014). The CA3 burst also recruits local CA1 interneurons, providing a source of feed-forward inhibition with a short delay ($\sim$2ms) to CA1 pyramidal neurons (Alger and Nicoll, 1982, Pouille and Scanziani, 2001, Somogyi

et al., 2014). Since CA3 exerts both direct excitatory and indirect feed-forward inhibitory influence on CA1 pyramidal cells, the consequences of scaling the magnitude of CA3 input on the membrane potential (Vm) of CA1 neurons are hard to predict in vivo. Individual CA1 pyramidal neurons receive ∼30,000 excitatory inputs (Megias et al., 2001), and hence have the potential to be activated by many combinations of presynaptic partners. However, previous experiments suggest that CA1 pyramidal neurons fire only in a small subset of ripples, in a way that reflects previous experience (Wilson and McNaughton, 1994, Foster and Wilson, 2006, O'Neill et al., 2006, Diba and Buzsaki, 2007). The mechanisms enforcing such sparseness and selectivity of CA1 firing during ripples remain unknown.

Spiking of pyramidal cells and specific classes of interneurons is phase-locked to LFP ripple oscillations recorded in the pyramidal cell layer (Buzsaki et al., 1992, Klausberger et al., 2003). Hence, ripple oscillations coordinate spike timing within the CA1 population bursts. Three models of ripple generation have been proposed, each making different predictions regarding the spatiotemporal distribution of inputs onto CA1 neurons and their impact on membrane potential dynamics. First, sparse axo-axonal gap junctions between CA1 pyramidal neurons are thought to aid in the generation and propagation of ripple-frequency action potentials (Draguhn et al., 1998, Traub and Bibbig, 2000). This model predicts the presence of "spikelets" reflecting the antidromic propagation of action potentials from ectopic generation sites. Second, pyramidal cells receive ripple-frequency somatic inhibition due to reciprocal interactions within interneuron networks, pyramidal-interneuron interactions, or both (Ylinen et al., 1995, Stark et al., 2014, Buzsaki, 2015). According to this model, as neurons are hyperpolarized towards the reversal potential for inhibition, the phase of intracellular ripple oscillations should remain constant. Below the inhibitory rever-

sal potential, their phase should abruptly flip 180 degrees. A third model, based on in vitro slice experiments, suggests that, in addition to inhibition, CA1 pyramidal cells might also receive ripple-frequency excitation (Maier et al., 2011). If this were true, the phase of intracellular ripple oscillations should vary continuously with Vm, as the relative contribution of excitation and inhibition changes due to differences in electrical driving force.

These competing hypotheses regarding the spatiotemporal distribution of excitatory and inhibitory inputs onto CA1 pyramidal neurons make specific predictions regarding their impact on the membrane potential. Yet, few studies have examined the membrane potential dynamics of CA1 pyramidal neurons during ripples in vivo (Ylinen et al., 1995, Kamondi et al., 1998, Maier et al., 2011, English et al., 2014, Valero et al., 2015). Here, we combine multisite LFP measurements with simultaneous whole-cell recordings in awake mice. Using this approach, we characterize the relationship between the strength of net excitatory input to CA1 and the membrane potential dynamics around ripples. In addition, we provide the first quantitative description of the phase relationship between spiking, intracellular, and LFP ripple oscillations in awake animals. Lastly, we discuss the consequences of our experimental observations for circuit models of ripple generation.

2.3 Results

The Average Membrane Potential Response During Ripples Has Three Components

To investigate the membrane potential dynamics of pyramidal cells during ripple events, we combined whole-cell recordings from identified CA1 pyramidal neurons with simultaneous LFP measurements from a nearby (200-250 μm) multisite silicon probe in awake, head-fixed mice (Figure 1 A-C). Before performing whole-cell recordings, a recording site

Figure 1: In vivo whole-cell recordings from identified CA1 pyramidal neurons with simultaneous multisite extracellular measurements in awake mice (Continued on following page).

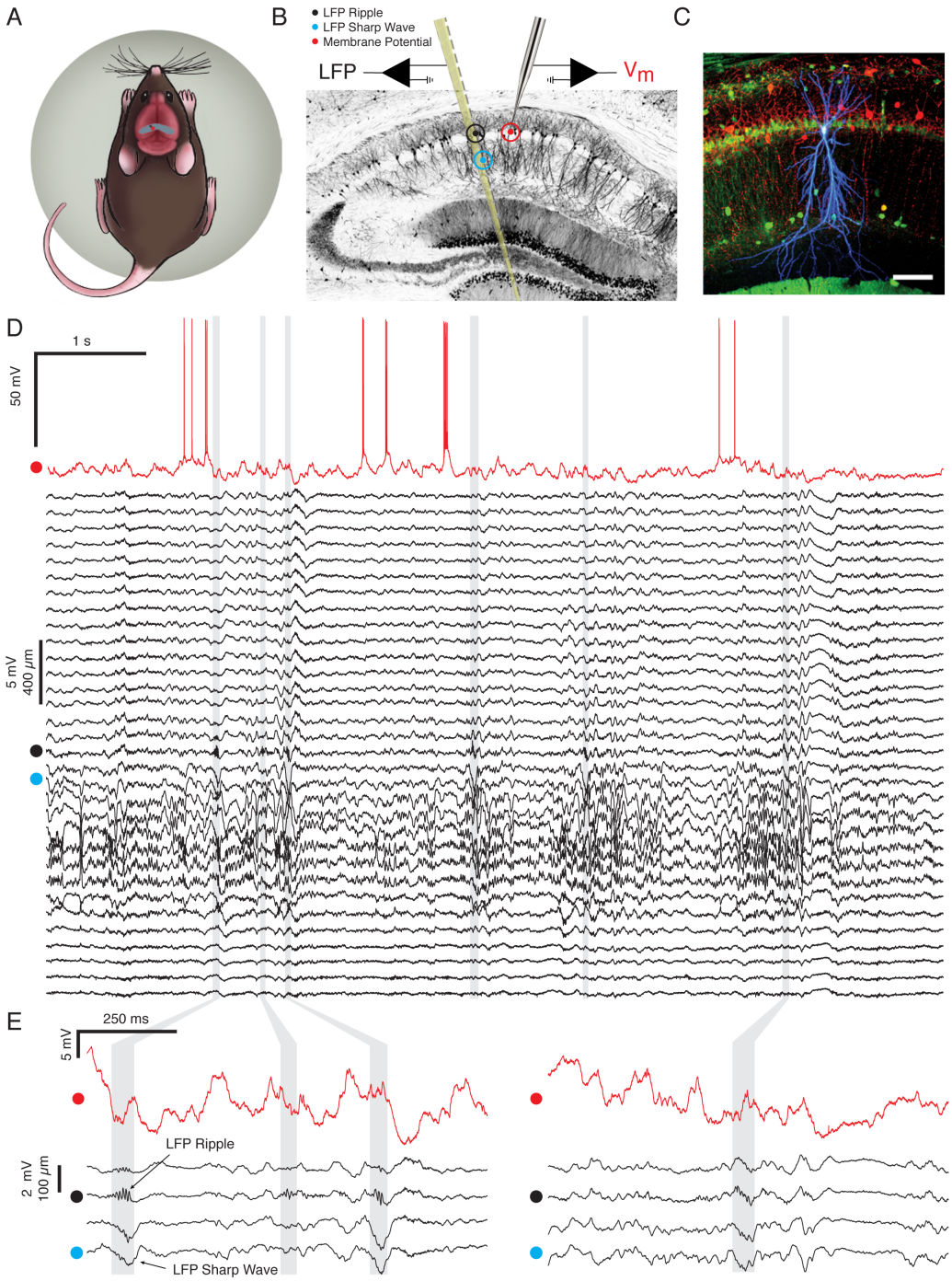

Figure 1: **(A)** Schematic of a mouse on the spherical treadmill. The approximate whole-cell (red dot) and LFP (black dot) recording locations are marked on top of dorsal CA1. **(B)** Illustration of the placement of the multisite silicon probe and patch pipette on a coronal slice of the dorsal hippocampus. Black, cyan, and red dots mark the locations of LFP ripple, LFP sharp wave, and whole-cell recordings, respectively. **(C)** Confocal image of 100 μm thick coronal section showing biocytin stained CA1 pyramidal neuron (blue) with combined immunohistochemistry against parvalbumin (red) and calbindin (green). Scale bar is 100 μm. **(D)** Example of simultaneous intracellular (red) and multisite LFP (black) recordings of spontaneous activity in an awake mouse. LFPs come from 32 channels spanning the neocortex, the hippocampal formation, and parts of the thalamus. The red dot next to the intracellular recording marks -55 mV. The black dot marks the channel within the CA1 pyramidal cell layer showing LFP ripple oscillations. The cyan dot marks the channel showing LFP sharp waves. Grey vertical bands mark the ripples detected in this segment. **(E)** Same as in (D), but enlarged to show subthreshold Vm (red), and sharp waves and ripples in the LFP (black traces are 4 of the 32 LFP channels shown in D).

from the silicon probe was carefully positioned within the CA1 pyramidal cell layer, where LFP ripple oscillations are reliably observed. Negative sharp waves, reflecting excitatory input onto the dendrites of CA1 pyramidal neurons, were observed in stratum radiatum and often co-occurred with ripples (Figure 1 D-E). Mice were free to walk or run on a spherical treadmill, but spent the majority of their time in a state of quiet wakefulness, when the hippocampal LFP showed large irregular activity with associated high-frequency ripples in the CA1 pyramidal cell layer. Figure 1 D shows an example of simultaneous whole-cell and LFP recordings from 32 sites spanning the neocortex, hippocampal formation, and parts of thalamus during a period of quiet wakefulness with six ripples. While the occurrence of ripples is apparent by inspecting the LFP, large ongoing membrane potential fluctuations and the diversity in the intracellular response during ripples make it harder to identify these events in the Vm (Figure 1 E; Figure 2).

Across a total of $\sim$8 hours of spontaneous activity from 30 neurons, we detected 4769 LFP ripples based on ripple-band power from the probe site located in the CA1 pyramidal cell layer. We then analyzed the membrane potential triggered on LFP ripples. Despite

Figure 2: Membrane potential dynamics during single ripples are highly diverse **(A1)** Example of intracellular activity during four LFP ripples from a single neuron. LFPs from the four channels around the CA1 pyramidal cell layer are shown in black. The black dot marks the channel showing LFP ripples, which occur at time 0. The cyan dot marks the channel with LFP sharp waves. The membrane potential is shown in red below. Note that while ripples are readily detected in the LFP, they are much less obvious in the membrane potential. **(A2-3)** Same as in (A1) but for an additional two neurons.

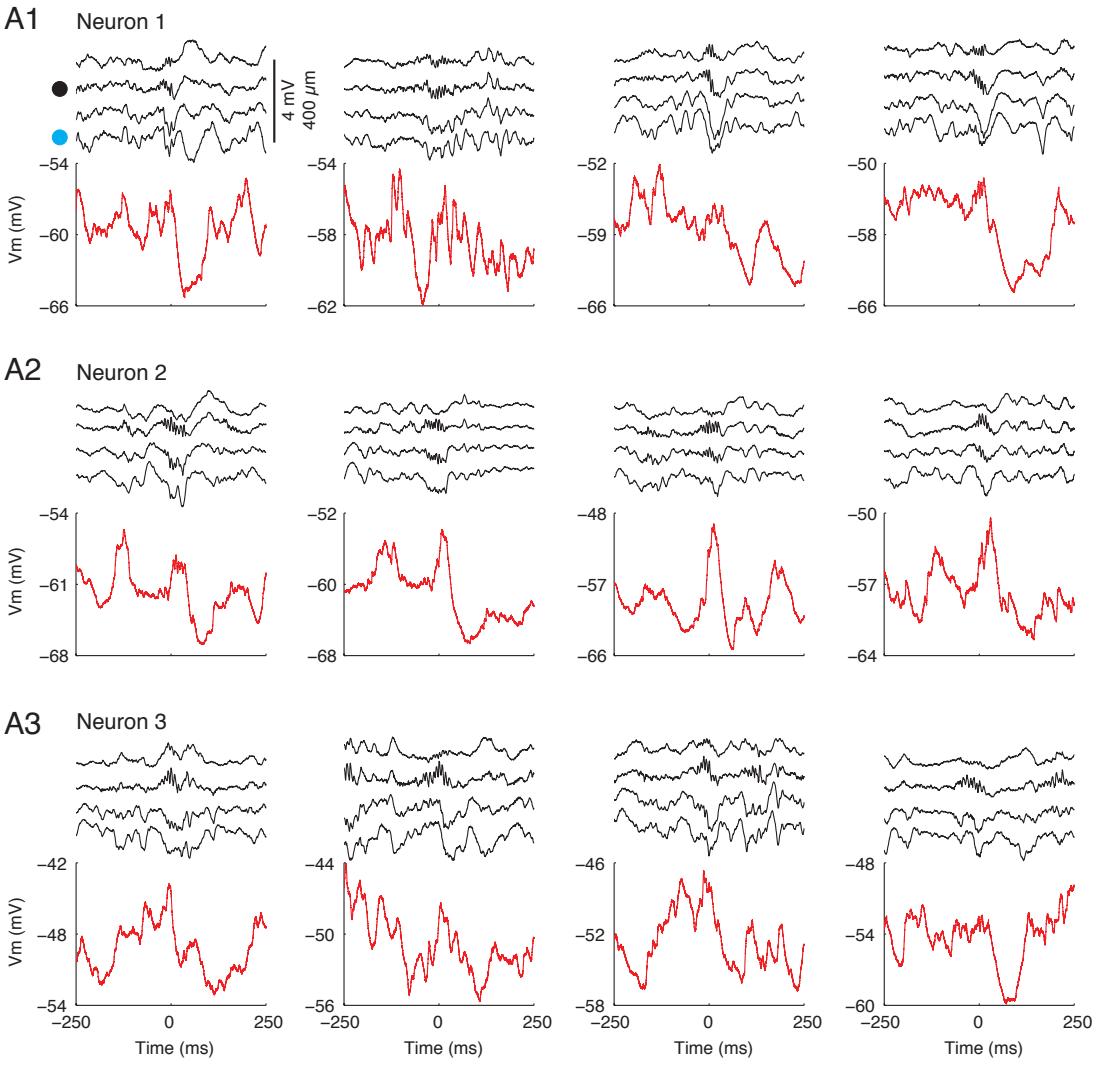

the variability in the membrane potential dynamics during single ripples, averaging across all ripples revealed a stereotyped waveform composed of three components: a sharp wave-associated depolarization (depolarization), superimposed ripple-frequency Vm oscillations (intracellular ripple), and a post-ripple hyperpolarization (hyperpolarization) lasting hundreds of milliseconds (Figure 3 A)(Ylinen et al., 1995, Maier et al., 2011, English et al., 2014). A time-frequency decomposition showed that LFP ripple oscillations (LFP ripples) and intracellular ripples are restricted in both time and frequency and have similar structure (Figure 3 B).

Diverse Single Neuron Membrane Potential Dynamics During Ripples

Pyramidal neurons in CA1 are a heterogeneous population of cells that differ in terms of their morphology, connectivity, and gene expression patterns (Graves et al., 2012, Lee et al., 2014). Therefore, individual pyramidal neurons may show cell-specific responses during ripples (Valero et al., 2015). To investigate this possibility, we computed the average ripple-triggered Vm for each neuron. Figure 3 C1-C8 shows example neuron-averages arranged according to their pre-ripple Vm. The intracellular depolarization, ripple, and hyperpolarization could be identified for nearly every neuron, but with a range of amplitudes that showed no obvious clustering of response type. This analysis also revealed a subset of neurons that slowly ramp their Vm beginning approximately one second before ripple onset. Three neurons had significant depolarizing ramps (Figure 3 C1, C2, C5) and two neurons had significant hyperpolarizing ramps (Figure 3 C6, C8), though most neurons showed no obvious ramping on average (N=25).

What underlies the diversity in single neuron responses during ripples? One contributing factor could be the resting membrane potential via its effect on the electrical driving

Figure 3: Average membrane potential dynamics during ripples (Continued on following page)

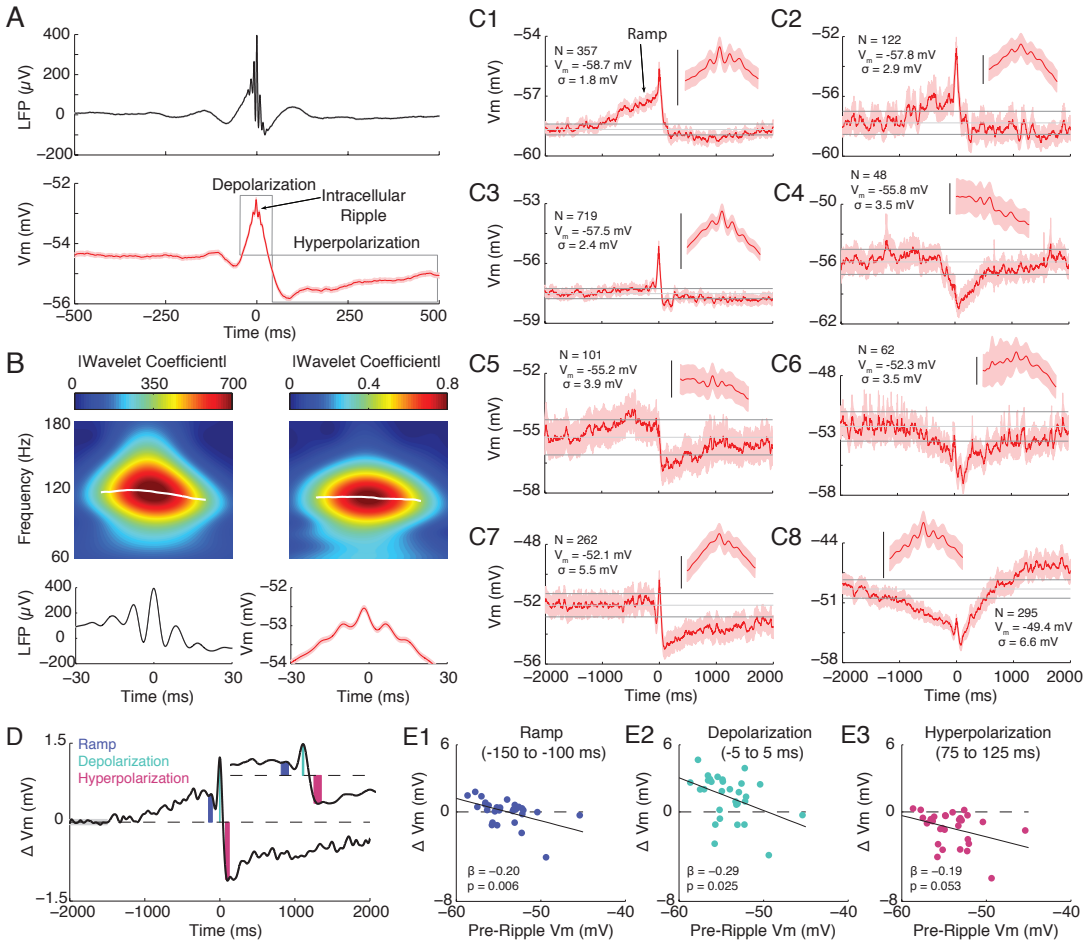

Figure 3: **(A)** Ripple-triggered averages of the LFP from the CA1 pyramidal cell layer (top) and subthreshold Vm (bottom) for 4769 ripples. Shaded regions mark mean ± SEM. Note 3 components to the average intracellular response: a sharp wave associated depolarization (depolarization), superimposed ripple-frequency Vm oscillations (intracellular ripple), and a prolonged, post-ripple hyperpolarization (hyperpolarization). **(B)** Enlarged view from (A) showing average ripple oscillations in the LFP (bottom, left) and Vm (bottom, right). Above each average are the wavelet-derived spectrograms showing that the average LFP and intracellular ripple are restricted in time/frequency. The magnitude of the wavelet coefficient was used as the instantaneous power. The white traces on the spectrograms mark the instantaneous frequency with the largest power at each sample. **(C1-C8)** Examples of ripple-triggered averages of the subthreshold Vm for individual neurons, arranged according to their pre-ripple Vm (-2 to -1.5 s). The shaded region marks the 95% confidence intervals for each sample. The upper and lower horizontal grey lines are the mean confidence intervals of the pre-ripple Vm. The middle grey line marks the mean Vm from this same interval. The inset shows a magnification (± 30 ms) of intracellular ripple oscillations. Scale bars are 2 mV. The number of ripples, the pre-ripple Vm, and the standard deviation of the pre-ripple Vm are listed for each neuron. Note the presence of depolarizing (C1, C2, C5) and hyperpolarizing (C6, C8) ramps in the Vm for a subset of neurons starting approximately 1 second before the ripple event. Note also that more hyperpolarized neurons (top panels) tend to have depolarizing ramps and larger sharp-wave associated depolarizations, while more depolarized neurons (bottom panels) tend to have larger post-ripple hyperpolarizations. **(D)** Schematic showing quantification of intracellular response amplitude in short windows at the end of the ramp (blue; -150 to -100 ms), and during the depolarization (turquoise; -5 to 5 ms) and hyperpolarization (pink; 75 to 125 ms). The component amplitudes (colored bars) were computed as the difference between the median Vm in these windows and the pre-ripple Vm (grey bar; average from -2 to -1.5 s). The inset shows a magnified view around the component windows. **(E1-E3)** Scatter plots showing the relationship between pre-ripple Vm and the amplitude of the ramp (E1), the depolarization (E2), and the hyperpolarization (E3).

Figure 4: The average membrane potential dynamics during ripples are robust with respect to LFP ripple detection criteria **(A1-A8)** Examples of ripple-triggered averages of the subthreshold Vm for individual neurons, as in Figure 3 C1-C8, but using more stringent (blue) or less stringent (red) ripple detection criteria. For each neuron, we detected LFP ripples greater than 4 times the median of the ripple-band envelope, resulting in 40% more ripples than in the main text. Shown in red is the average of all detected ripples. Shown in blue is the average of the largest half of ripples. Neurons are arranged according to their pre-ripple Vm. Shaded regions mark mean ± SEM. Insets show the average intracellular ripple oscillation for all ripples (red) and the largest half (blue), from -25 to 25 ms. Each legend lists the number of ripples entering the averages and LFP ripple detection threshold. Note that the shape of the average membrane potential is very similar for both low and high detection thresholds, suggesting that the observed neuron-to-neuron diversity is not a result of different detection thresholds. **(B1)** Correlation between the amplitude of the ramp using more stringent (x-axis) and less stringent (y-axis) ripple detection criteria. Each dot is a neuron. Note that most neurons lie along the diagonal, indicating that the amplitude of the ramp is similar, independent of ripple detection threshold. **(B2)** Same as in B1, but for the amplitude of the depolarization. **(B3)** Same as in B1, but for the amplitude of the hyperpolarization. **(B4)** Same as in B1, but for the amplitude of the intracellular ripple oscillation. Note: all amplitudes are computed as in Figures 3/5.

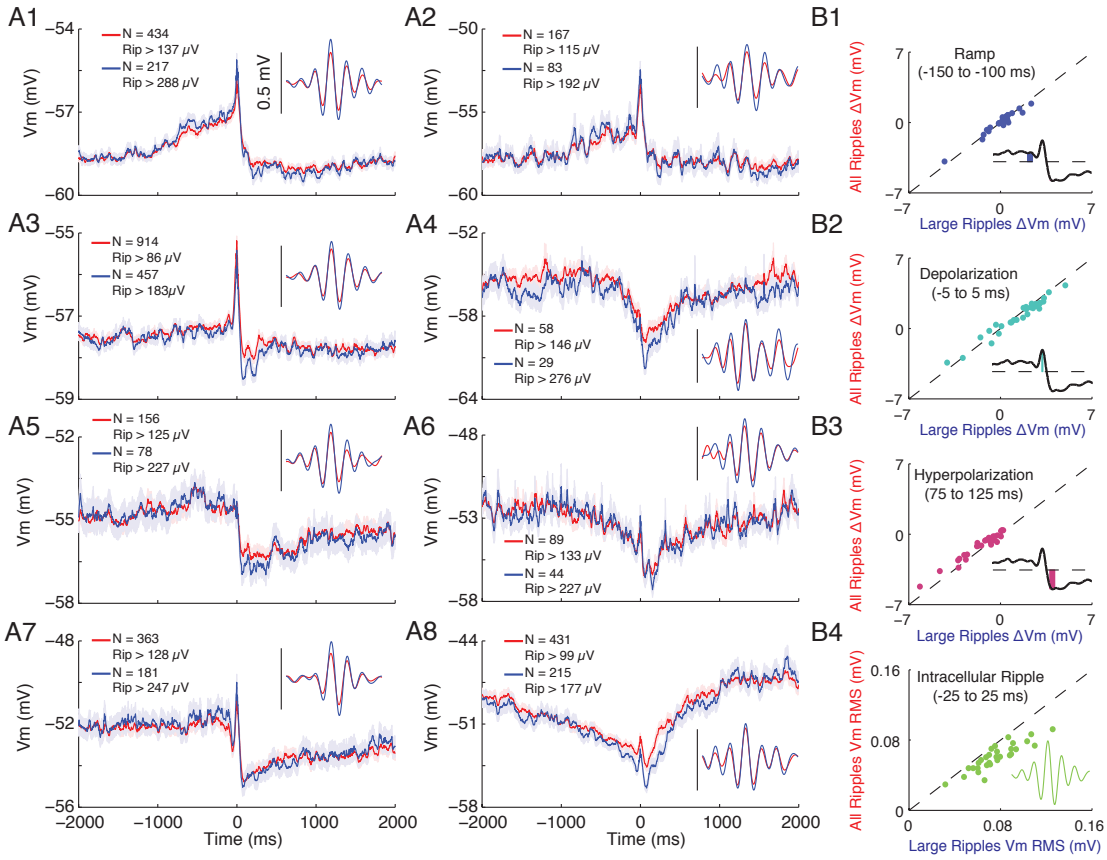

Figure 5: Membrane potential dependence of intracellular ripple oscillation amplitude **(A)** Average ripple-band Vm (intracellular ripple) from the most depolarized half (black) and hyperpolarized half (red) of ripples from a single neuron. **(B)** Scatter plot showing relationship between peri-ripple Vm (± 25 ms average) and intracellular ripple RMS for all single ripples from the same neuron as in (A). Note that ripples occurring at more depolarized levels tend to be larger, giving rise to a positive slope estimate (β>0; p<0.001). **(C)** Comparison of slope estimates (β) computed as in (B) across all 30 neurons, sorted by the number of ripples for each neuron. Neurons with the largest number of ripples are on top. Green dots mark slope estimates. Rectangles are the 95% confidence intervals. Black rectangles indicate slope estimates that are significantly different from 0 (grey otherwise). Black dot marks location of neuron used in (A-B). Note that the majority of neurons (26 of 30) tended to have larger intracellular ripples at more depolarized levels, as indicated by positive slope estimates ($\beta > 0$), which is statistically different (p<0.01) from the expected proportion of 0.5 using a two-sided binomial test.

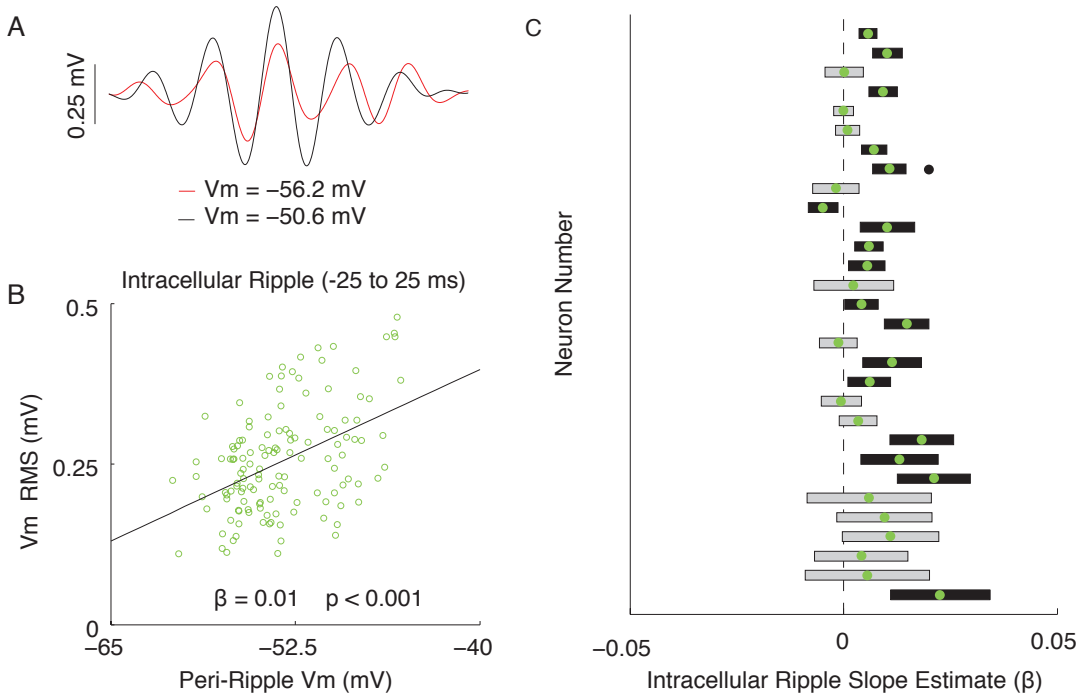

force for excitation and inhibition. Indeed, more hyperpolarized neurons (top panels of Figure 3 C) have depolarizing ramps and bigger sharp wave associated depolarizations, while depolarized neurons (bottom panels of Figure 3 C) tend to have larger post-ripple hyperpolarizations (Figure 3 D-E). Similarly, the majority of neurons (16 of 30) had significantly larger intracellular ripples when they were more depolarized (Figure 5), though this was not observed in the neuron averages ($p=0.91$; not shown). Together, these results further support the notion that CA1 pyramidal neurons are a heterogeneous population and suggest the state of individual neurons, as reflected in their resting membrane potential, affects the intracellular response during ripples.

Membrane Potential Dynamics Vary With LFP Sharp Wave Amplitude

Hippocampal ripples often co-occur with negative sharp waves in the LFP of stratum radiatum (Figure 1). Sharp waves reflect excitatory input from area CA3 impinging on the dendrites of CA1 pyramidal neurons, and their amplitude correlates with, and therefore serves as a proxy for, the magnitude of the excitatory synaptic currents (Figure 7). Excitatory input from CA3 also recruits local CA1 interneurons, producing feed-forward inhibition onto CA1 pyramidal neurons. Therefore, by characterizing how the intracellular response varies as a function of sharp wave amplitude, we can assess the interplay between excitation and inhibition as a function of input strength.

To characterize how the membrane potential dynamics change with input strength, we sorted all 4769 intracellular responses by the amplitude of the LFP sharp wave and examined how the shape of the intracellular response varied (Figure 6 A-C). Surprisingly, the amplitude of the intracellular depolarization was relatively independent of sharp wave amplitude. In contrast, larger LFP sharp waves were associated with a larger post-ripple

Figure 6: Membrane potential dynamics vary with sharp wave amplitude **(A)** Top: Ripple-triggered LFP from stratum radiatum, sorted by sharp wave amplitude for all 4769 ripples. Bottom: Quartile averages color coded according to dots above. The inset to the left shows the average LFP sharp wave (bottom trace) along with its amplitude (vertical grey line). The inset to the right shows a magnified view of the quartile averages (± 100 ms). **(B)** Top: Subthreshold Vm sorted by sharp wave amplitude from (A). Each row is normalized to have 0 mean (Vm Norm). Quartile averages shown below. The inset shows a magnified view of the depolarization (± 100 ms). Note that larger sharp waves are associated with a larger post-ripple hyperpolarization, while the depolarization is relatively unaffected. **(C)** Top: Ripple-band Vm sorted by sharp wave amplitude from (A). Quartile averages shown below. **(D)** Scatter plot between LFP sharp wave amplitude and intracellular ramp amplitude. For D-G, to get an estimate of the component's amplitude, the sharp wave sorted response matrices (from A-C) were divided into 190 blocked averages of 25 sharp waves each, and the amplitude of each component was computed as in Figures 3/5. The inset shows a schematic of how ramp amplitude was computed. **(E)** Same as in D, but for the amplitude of the depolarization. **(F)** Same as in D, but for the amplitude of the hyperpolarization. **(G)** Same as in D, but for the RMS amplitude of intracellular ripples. Notice that only the hyperpolarization and intracellular ripple change systematically as a function of sharp wave amplitude, while the ramp and depolarization remain invariant.

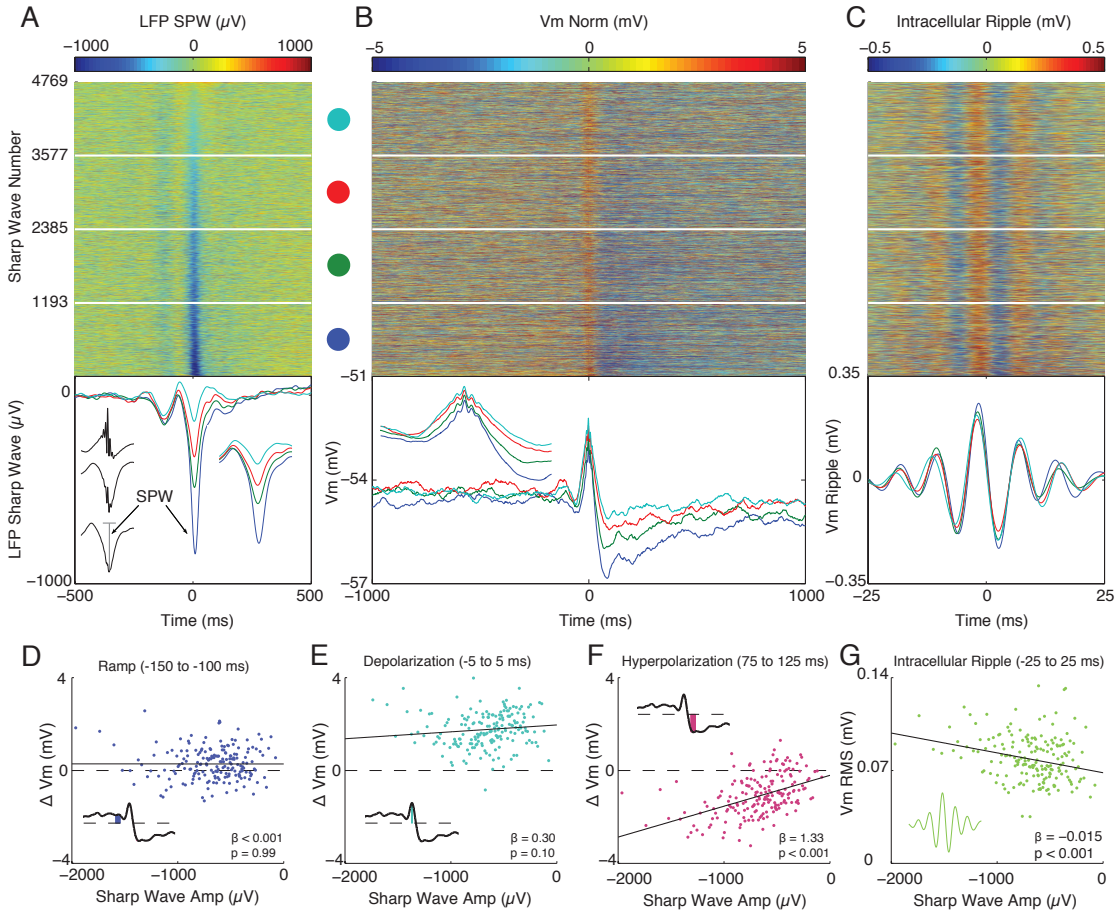

Figure 7: The intracellular depolarization scales with LFP sharp wave amplitude under hyperpolarizing current injection (Continued on following page)

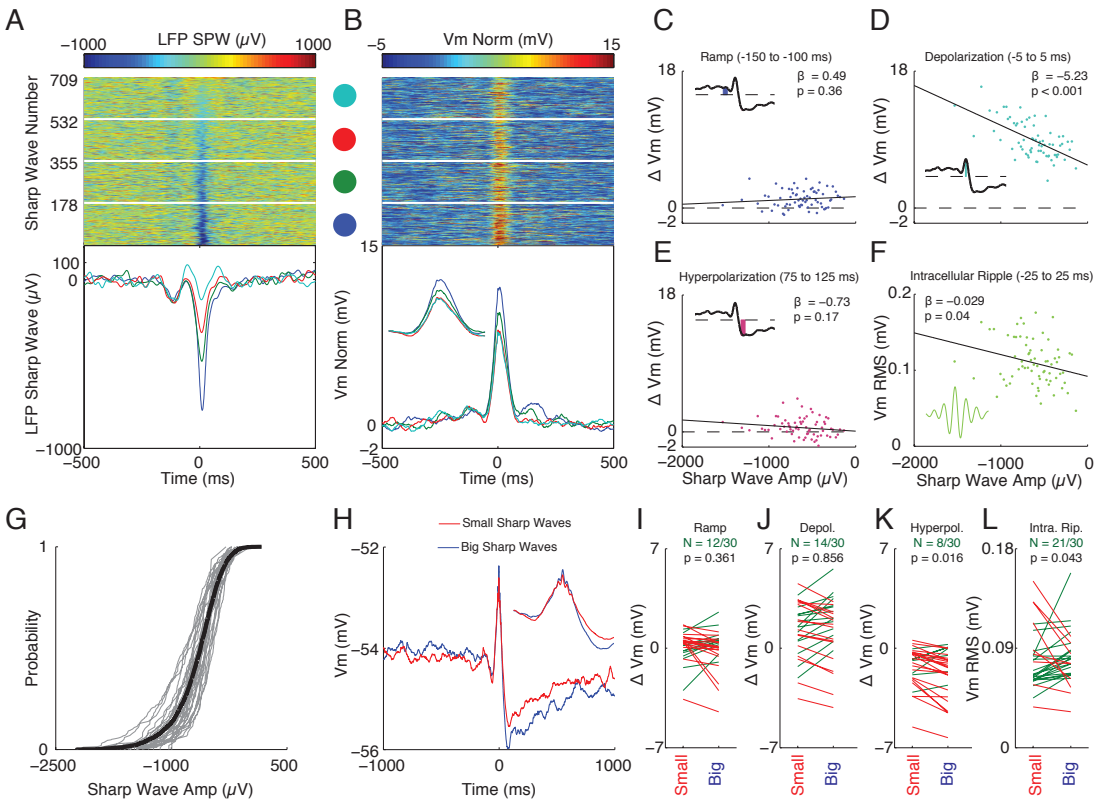

Figure 7: **(A)** Top: Ripple-triggered LFP from stratum radiatum sorted by sharp wave amplitude for all 709 ripples during hyperpolarizing current injection (N=10 neurons). Bottom: Quartile averages color coded according to dots above. **(B)** Top: Subthreshold Vm sorted by sharp wave amplitude from (A). Each row is normalized to have 0 mean (Vm Norm). Quartile averages shown below. The inset shows a magnified view of the depolarization ($\pm$ 100 ms). Note that, under hyperpolarizing current injection, which decreases the driving force for inhibition, larger sharp waves are associated with a larger intracellular depolarization, which further supports the notion that sharp wave amplitude correlates with net excitatory current. It also provides further support for the conceptual model in Figure 14. **(C)** Scatter plot between LFP sharp wave amplitude and intracellular ramp amplitude. For C-F, the sharp wave sorted response matrices (from A-B) were divided into 70 blocked averages of 10 sharp waves each, and the amplitude of each component was computed as in Figures 3/5. The inset shows a schematic of how ramp amplitude was computed. **(D)** Same as in C, but for the amplitude of the depolarization. **(E)** Same as in C, but for the amplitude of the hyperpolarization. **(F)** Same as in C, but for the amplitude of the intracellular ripple. **(G)** Cumulative distribution function (CDF) of each neuron's LFP sharp wave amplitudes (grey). The CDF for all sharp waves is shown in black. **(H)** Grand average of the subthreshold Vm from the smallest (red) and largest (blue) half of sharp waves, averaged across neurons. For each neuron, the ripple-triggered subthreshold Vm was sorted by the amplitude of the neuron's LFP sharp waves and broken into two averages: one from the smallest half and one from the largest half of sharp waves. The amplitudes of the four intracellular components from these two averages are compared in (I-L) for all 30 neurons. This procedure controls for differences in sharp wave amplitude across neurons. Note that only the post-ripple hyperpolarization shows an obvious modulation with sharp wave amplitude, consistent with grouped data from Figure 6. **(I)** The intracellular ramp amplitude is plotted for the smallest and largest half of LFP sharp waves for all 30 neurons. Neurons whose ramp amplitude was more hyperpolarized for big sharp waves are shown in red. Neurons whose ramp amplitude is more depolarized for big sharp waves are shown in green. The number of neurons with more depolarized ramps with big sharp waves is reported in the inset above, along with a p-value testing whether the proportion of neurons is significantly different expected proportion of 0.5 using a two-sided binomial test. **(J)** Same as in (I), but for the amplitude of the depolarization. Note that about as many neurons show larger depolarizations with big sharp waves as show smaller depolarizations, consistent with a balance of excitation and inhibition across neurons. **(K)** Same as in (I), but for the amplitude of the hyperpolarization. Note that a significant majority of neurons show larger hyperpolarizations for big sharp waves. **(L)** Same as in (I), but for the amplitude of the intracellular ripple oscillation. Note that a significant majority of neurons show larger intracellular ripple oscillations with big sharp waves.

hyperpolarization and larger intracellular ripple oscillations (Figure 6 B-C). Only a negligible post-ripple hyperpolarization occurred with the smallest sharp waves. To statistically assess these relationships, we performed linear regressions between sharp wave amplitude and the amplitude of the intracellular components (Figure 6 D-G). Consistent with the quartile-averages, larger sharp waves were associated with larger post-ripple hyperpolarizations ($p<0.001$) and intracellular ripples ($p<0.001$), while the ramp ($p=0.99$) and intracellular depolarization ($p= 0.10$) were invariant. These results suggest that larger excitatory currents are balanced by a proportional inhibition, such that the net current depolarizing the soma is invariant to sharp wave amplitude, on average. Under hyperpolarizing current injection, when the driving force for inhibition is reduced and this balance is altered, larger LFP sharp waves are associated with a larger intracellular depolarization (Figure 7).

Phase Relationships Between Spiking, Intracellular, and LFP Ripple Oscillations

Ripple oscillations are thought to be functionally important for controlling spike timing and bringing CA1 output within the windows of synaptic integration and plasticity, but the factors that determine whether and when a neuron fires during a given ripple remain poorly understood. As shown in Figure 8 A, ripples where the neuron fired had an intracellular depolarization several times larger than the average intracellular depolarization in ripples with no spikes. Moreover, the ripple-triggered raster plot of pyramidal cell firing (Figure 8 B) demonstrates that spikes occurred around the trough of LFP ripples (Figure 8 C; Figure 9). Importantly, this occurred when the slope of the membrane potential was near its maximum. This suggests that the amplitude of the intracellular depolarization is primarily responsible for bringing neurons to spike threshold while the fast, transient depolarizations during intracellular ripple oscillations are particularly effective at controlling spike timing.

Figure 8: Large intracellular depolarizations bring neurons to spike threshold, while intracellular ripple oscillations control the precise spike timing **(A)** Averages of the subthreshold Vm for ripples where the neuron fired at least one action potential (red; N=1057) or did not fire (blue; N=3712). Shaded regions mark mean ± SEM. Note that for ripples with at least one spike, the Vm had a depolarization several times larger than the average depolarization for ripples with no spikes. **(B)** Ripple-triggered raster plot of spike times from whole-cell recordings. **(C)** Average LFP ripple (black), intracellular ripple (red), and firing rate (green). The firing rate was computed by smoothing spike times with a gaussian (σ=1 ms) and averaging across all ripples. Vertical dashed lines mark the time of the peak firing rate and peak LFP ripple oscillation. Note that the peak firing rate occurs near the trough of LFP ripple oscillation, when the slope of the intracellular ripple is near its maximum.

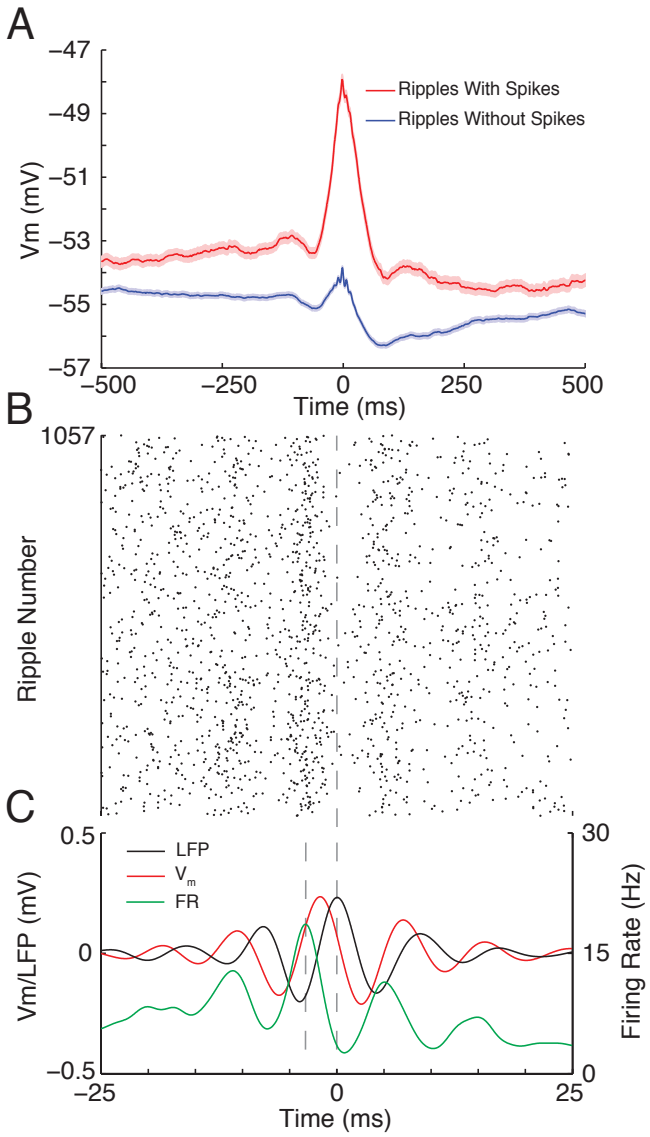

Figure 9: Spikes are phase-locked near the trough of LFP ripple oscillations **(A)** Distribution of spike phases relative to the LFP ripple oscillation from whole-cell recordings. **(B)** Same as in (A), but for N=28 putative CA1 pyramidal neurons from juxtacellular recordings in the same mice used for whole-cell recordings. Note that for both whole-cell and juxtacellular recordings, spikes occur ∼0.8 ms after the trough of LFP ripple oscillations.

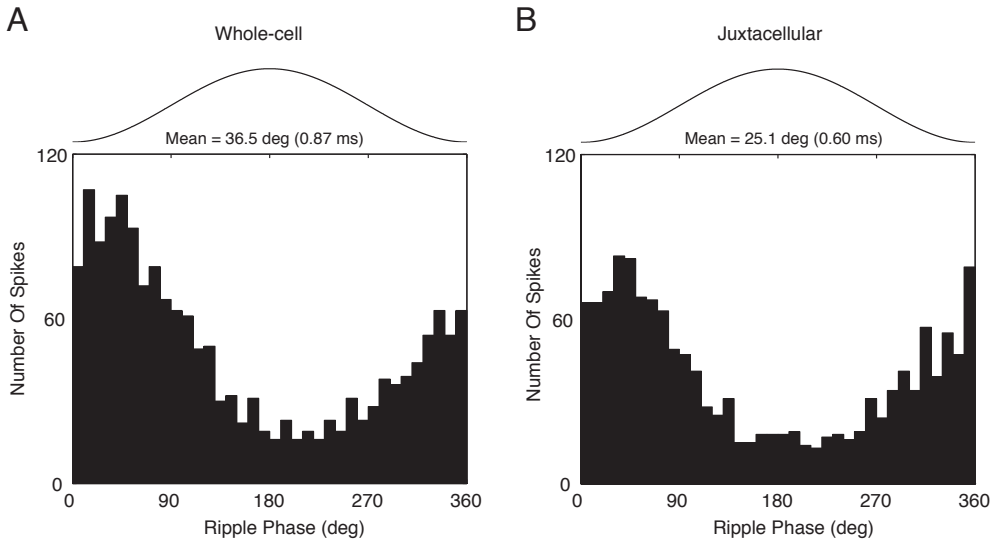

Figure 10: Intracellular ripple oscillations lead LFP ripple oscillations by ∼90 degrees and are ∼5 Hz slower **(A)** Each neuron's average intracellular ripple (red) and LFP ripple (black) from -25 to 25 ms around LFP ripple center. Ripples where the intracellularly recorded neuron fired were excluded since action potentials have a duration comparable to a ripple cycle, making phase estimation of the intracellular ripple difficult. Note that for all neurons the central peak in the LFP lags behind the central peak in the Vm. **(B)** Instantaneous frequency of LFP ripples for each neuron. Time 0 marks the ripple center (time of central LFP peak). For B-E, Each neuron's average is grey scaled according to its LFP ripple frequency at time 0. Averages are shown in red. Only neurons (22/30) with reliable phase/frequency estimates in a ± 20 ms window were included in B-E. Instantaneous frequency and phase are computed from a continuous wavelet transform using complex Morlet wavelets. For each sample, the frequency with the largest power was identified and its phase and frequency taken as the waveform's instantaneous value (white lines shown in Figure 3 B). **(C)** Instantaneous frequency of intracellular ripples for each neuron. **(D)** Difference between LFP and intracellular ripple frequency for each neuron. Note that LFP ripples are initially faster than intracellular ripples, and the frequency difference decreases with time. **(E)** Instantaneous phase difference between intracellular and LFP ripples. **(F)** LFP ripple frequency (at time 0) plotted as a function of its LFP ripple RMS for each neuron. **(G)** Intracellular ripple frequency (at time 0) plotted as a function of LFP ripple frequency for each neuron. Note that for all but one neuron, intracellular ripples are slower than LFP ripples. **(H)** Intracellular-LFP ripple phase difference (at time 0) for all 30 neurons (black lines). Average shown in red. **(I)** Juxtacellular ripple - LFP ripple phase difference (at time 0) for all 28 juxtacellular recordings (black lines) performed in same mice and anatomical location as whole-cell recordings and with similar glass pipettes. Average shown in red.

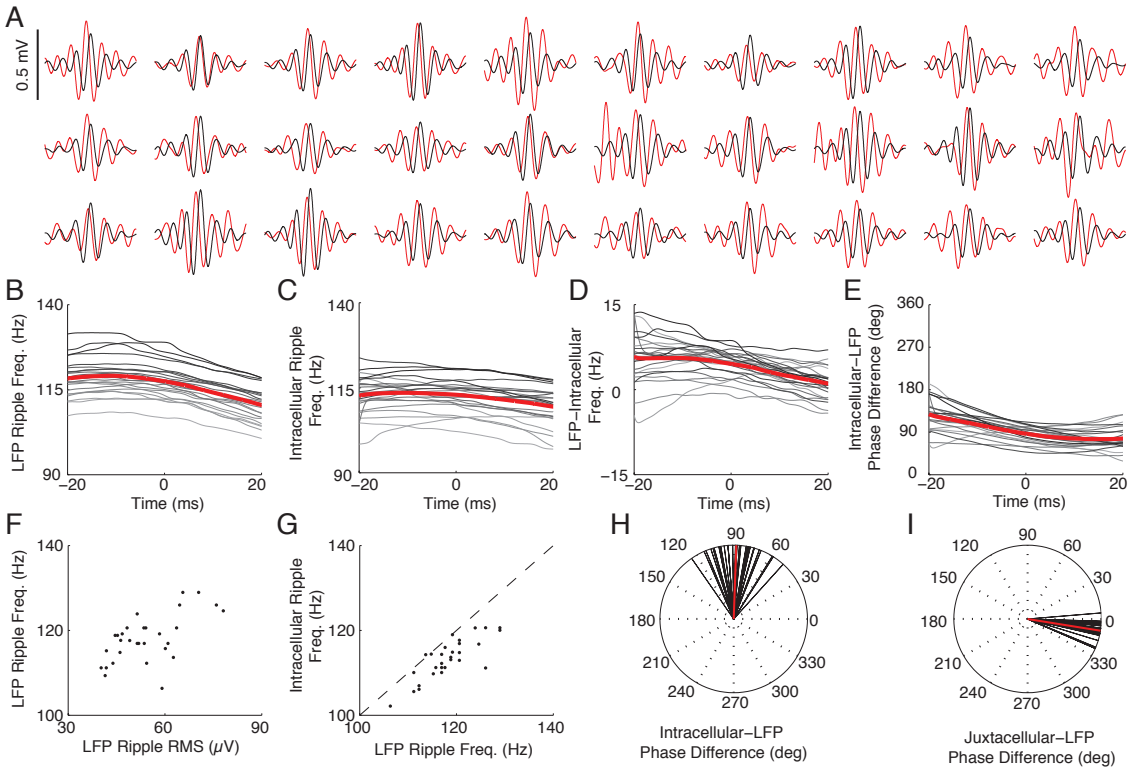

To investigate the relationship between intracellular and LFP ripple oscillations in more detail, we computed the average Vm and LFP in the ripple frequency band for each neuron. As shown in Figure 10 A, LFP ripples lagged intracellular ripples for all 30 neurons. A time-frequency decomposition of intracellular and LFP ripples revealed significant differences in their frequencies, relative phases, and their temporal evolution. As shown in Figure 10 B, LFP ripple frequency decreased from 118.3 ± 1.15 Hz near the beginning (-20 ms) of ripples to 110.5 ± 1.07 Hz near the end (20 ms) of ripples ($p<10^{-13}$; paired t-test). In contrast, the frequency of intracellular ripples was more stable, but still showed a significant decline from 112.5 ± 1.22 Hz to 109.4 ± 1.23 Hz ($p<0.001$, paired t-test; Figure 10 C). Hence, LFP ripples were initially faster than intracellular ripples (5.7 ± 0.96 Hz; $p<0.01$; unpaired t-test), but as their frequencies converged, the difference became insignificant (1.0 ± 0.59 Hz, $p=0.52$ unpaired t-test). Consistent with this observation, LFP ripples lagged intracellular ripples by 128.0 degrees (111.7 to 144.4; 95% CI) near the beginning of the ripples, compared to 76.7 degrees (65.6 to 87.8; 95% CI) near the end (Figure 10 E). At LFP ripple center, LFP ripples (117.5 ± 1.09 Hz) were 4.5 ± 0.50 Hz faster ($p<0.01$; unpaired t-test) than intracellular ripples (112.9 ± 1.00 Hz; Figure 10 D), and lagged intracellular ripples by 86.8 degrees (79.3 to 94.3; 95% CI; Figure 10 H). Across the population, larger LFP ripples had a faster frequency ($p<10^{-3}$; Figure 10 F), and faster LFP ripples were associated with faster Vm ripples ($p<10^{-7}$; Figure 10 G). These findings highlight the dynamic nature of ripple generation and regulation, and reveal important differences between the intracellular and LFP ripple oscillations.

While the distance between the probe site measuring LFP ripples and the whole-cell recording in CA1 was small (200-250 μm), the spatial separation could introduce biases in

Figure 11: Juxtacellular LFP ripples are synchronous with probe LFP ripples. Relationship between input and access resistance and the intracellular-LFP ripple phase difference **(A)** Each juxtacellular recording's average LFP ripple (red) and the probe's LFP ripple (black) from -25 to 25 ms. For all recordings, juxtacellular LFP ripples were recorded from the same anatomical location where whole-cell recordings were performed. Note that juxtacellular ripples and ripples recorded from probe are nearly synchronous. **(B)** Instantaneous LFP ripple frequency recorded on extracellular probe. For B-D, each recording's average is grey scaled according to its probe LFP ripple frequency at time 0. Averages are shown in red. **(C)** Same as in B, but for juxtacellular LFP ripples. **(D)** Same as in B, but showing the difference between probe LFP and juxtacellular ripple frequency. Notice that ripples recorded on the extracellular multisite probe and juxtacellularly on a pipette are very similar, in contrast to the differences observed in the whole-cell recordings. **(E)** Scatter plot of each neuron's input resistance (Rm) and phase delay between its intracellular ripples and LFP ripples. **(F)** Scatter plot of each neuron's access resistance (Ra) and the intracellular-LFP ripple phase delay.

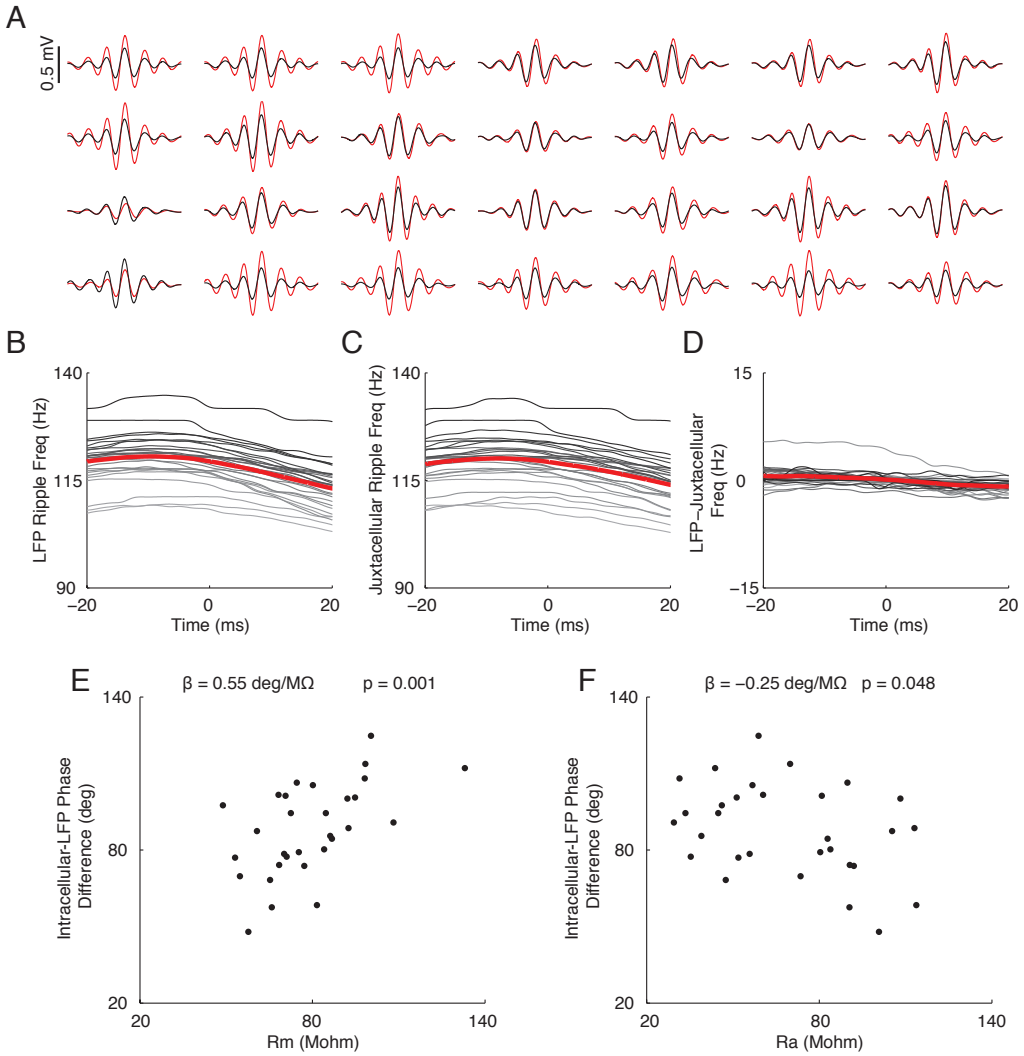

the phase and frequency comparisons. To address this, we performed juxtacellular recordings from putative CA1 pyramidal neurons and LFP ripples (Juxtacellular ripples) from the same anatomical location and with similar glass pipettes as whole-cell recordings and compared them to LFP ripples occurring simultaneously on the probe site in the CA1 pyramidal cell layer (probe ripples). On average, LFP ripples on the probe led Juxtacellular ripples by just 9.1 degrees (6.66 to 11.53; 95% CI; Figure 10 I) and had nearly identical frequencies as ripples recorded on the probe (Figure 11 A-D), ruling out biases in the phase/frequency comparisons due to the spatial separation between the multisite probe and pipette. Taking this 9 degree distance-related phase difference into account suggests that LFP ripples lag intracellular ripples by 96 degrees on average.

Though the time constant of the patch pipettes was considerably faster than ripples, the low-pass filtering properties of patch pipettes could in principle reduce the frequency and introduce phase delays in intracellular ripples. However, there was only a weak relationship between the magnitude of the access resistance and the phase difference between intracellular and LFP ripples (Figure 11 F). Moreover, juxtacellular ripples, which were subject to similar low-pass filtering since they were recorded with similar pipettes, had frequencies that were nearly identical to ripples from the probe, as noted above. There was a stronger relationship between the neuron's input resistance and the intracellular-LFP phase delay (Figure 11 E), suggesting that passive properties of the neurons may contribute to the observed phase delays. However, this cannot explain the evolution of intracellular and LFP ripple frequency and relative phase across time.

The Phase Difference Between Intracellular And LFP Ripple Oscillations Changes Systematically With Membrane Potential

Figure 12: Intracellular ripple phase changes systematically with membrane potential **(A)** Top: Average intracellular ripple (from -8 to 12 ms) plotted as a function of Vm for the range of spontaneous Vm fluctuations. All ripples lacking intracellular action potentials were sorted by their peri-ripple Vm (±25 ms average), and 29 averages of 125 ripples each are displayed. Traces are separated by 0.1 mV (scale bar in upper right is 0.5 mV) and colored according to their peri-ripple Vm. The central peak and the preceding/subsequent troughs are marked by black dots for each trace. Vertical bars mark average time of preceding trough (-6.1 ms), central peak (-1.7 ms), and subsequent trough (2.6 ms). Note that hyperpolarized ripples (cyan) are phase delayed relative to depolarized ripples (pink). Bottom: Average LFP ripple (black) and intracellular ripple (light blue). **(B)** Intracellular-LFP ripple phase difference plotted as a function of Vm for traces in (A). **(C)** Average intracellular (red) and LFP (black) ripple at resting Vm, along with the intracellular (cyan) and LFP (grey) ripple with hyperpolarizing current injection (N=10 neurons). Scale bar marks 0.5 mV. Note that the central peak of intracellular ripples occurring under hyperpolarizing current injection (cyan) nearly aligns with LFP ripples (black/gray). **(D)** Each neuron's Intracellular-LFP ripple phase difference (at time 0) for intracellular ripples during hyperpolarizing current injection (cyan; N=10 neurons). The average is shown in black.

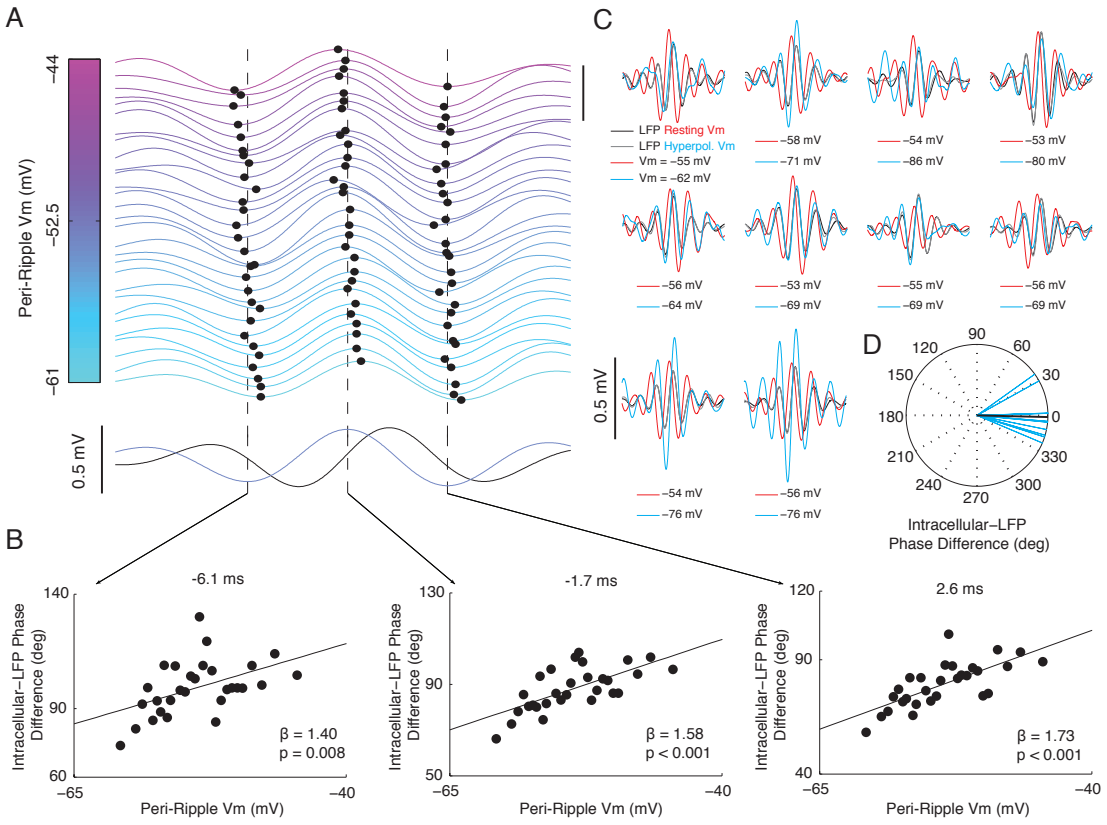

Figure 13: Intracellular blockade of voltage-gated sodium channels using QX-314 has no effect on intracellular ripple oscillations (Continued on following page)

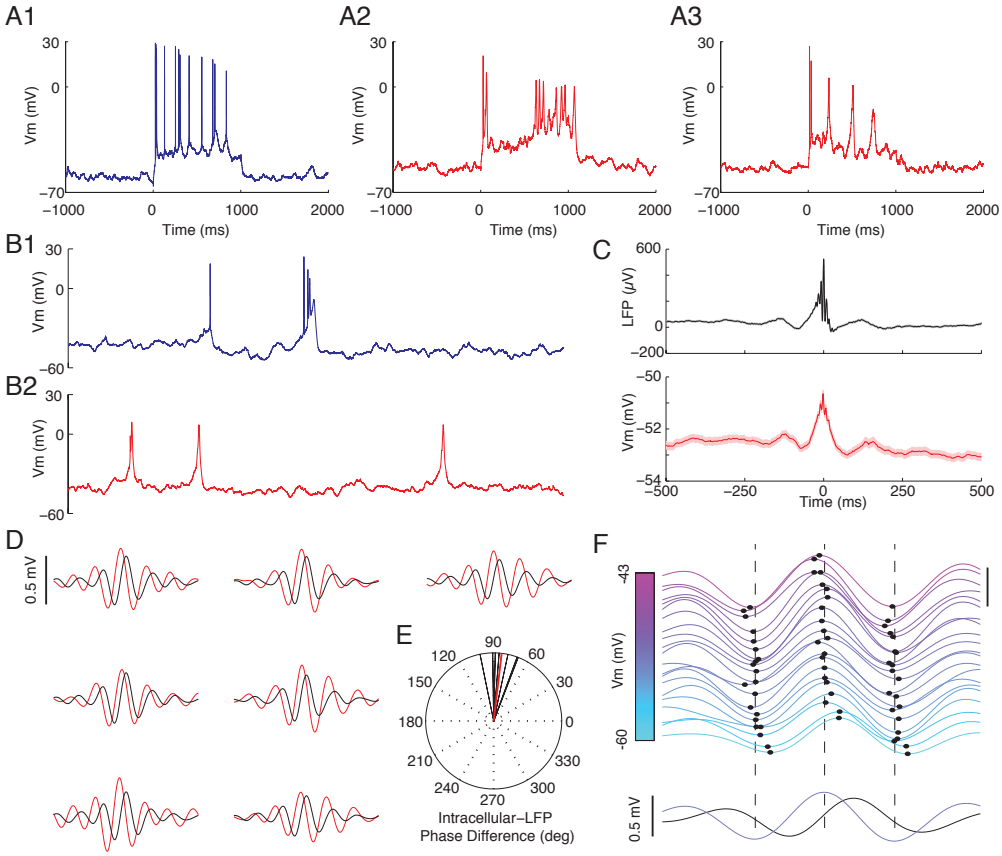

Figure 13: **(A1)** Example of an intracellular response to a 1-second depolarizing current step, immediately after breaking into the neuron. Note the presence of large sodium spikes of attenuating amplitude. **(A2-A3)** Same as in (A1), but a couple minutes after breaking into a neuron. While depolarizing current occasionally evoked 1-2 sodium spikes immediately after the start of the pulse, sodium spikes were largely replaced with slower, putative calcium spikes. **(B1)** Three second example of spontaneous activity immediately after breaking into the neuron. Note the presence of a single sodium spike and a complex burst. **(B2)** Same as in (B1), but after full QX-314 wash in. Note that sodium spikes have been replaced with slower, putative calcium spikes, similar to previous reports (Grienberger et al., 2014). Combined with the intracellular current steps, this demonstrates the effectiveness of QX-314 in blocking voltage-gated sodium channels. **(C)** Ripple-triggered averages of the LFP from the CA1 pyramidal cell layer (top) and subthreshold Vm (bottom) for 1070 ripples recorded from 7 neurons with intracellular QX-314. Shaded regions mark mean ± SEM. Note that while the intracellular depolarization and ripple oscillations are largely unaffected, the post-ripple hyperpolarization is diminished, consistent with the ability of QX-314 to block GABAb-mediated conductances. **(D)** Each neuron's average intracellular ripple (red) and LFP ripple (black) from -25 to 25 ms around LFP ripple center. Note that for all neurons the central peak in the LFP lags behind the central peak in the Vm, as in drug-free neurons (Figure 10). **(E)** Intracellular-LFP ripple phase difference (at time 0) for all 7 neurons (black lines). Average shown in red. Note that intracellular ripples lead LFP ripples by ∼90 degrees, similar to drug-free neurons (Figure 10). If voltage-gated sodium contributed to intracellular ripples around resting Vm, then blocking them should have shifted the intracellular-LFP ripple phase difference. **(F)** Top: Average intracellular ripple (from -8 to 12 ms) plotted as a function of Vm for the range of spontaneous Vm fluctuations. All ripples lacking intracellular action potentials were sorted by their peri-ripple Vm (±25 ms average), and 21 averages of 50 ripples each are displayed. Traces are separated by 0.1 mV (scale bar in upper right is 0.5 mV) and colored according to their peri-ripple Vm. The central peak and the preceding/subsequent troughs are marked by black dots for each trace. Vertical bars mark average time of preceding trough, central peak, and subsequent trough. Note that hyperpolarized ripples (cyan) are phase delayed relative to depolarized ripples (pink). Bottom: Average LFP ripple (black) and intracellular ripple (light blue). Note that the voltage dependence of intracellular ripple phase in QX-314 neurons is almost identical to drug-free neurons (Figure 12), which further demonstrates that voltage-gated sodium channels do not appreciably contribute to intracellular ripple oscillations.

Competing models of ripple oscillation generation offer different predictions regarding how the phase of intracellular ripple oscillations should vary with membrane potential (Figure 15). In order to evaluate these competing hypotheses, we investigated how intracellular ripple phase depends on Vm in vivo. As shown in Figure 12 A, ripples occurred at spontaneous membrane potential levels ranging from -61 mV to -44 mV. Interestingly, the time of the central Vm peak and the preceding/subsequent troughs varied systematically with Vm. Indeed, at more hyperpolarized levels, the phase lag between intracellular and LFP ripples was smaller compared to more depolarized levels (Figure 12 B). In particular, a 1 mV hyperpolarization in Vm was associated with approximately a 1.6 degree phase shift of intracellular ripples towards LFP ripples.

To further test the voltage dependence of intracellular ripple phase, we injected hyperpolarizing DC currents into a subset of neurons (N=10) to bring them between 7 mV to 32 mV below their resting Vm. Hyperpolarization resulted in intracellular ripples that had almost zero phase difference with LFP ripples, without producing consistent changes in intracellular ripple amplitude (Figure 12 C-D). At the time of the central LFP peak, intracellular ripples lagged LFP ripples by 1.4 degrees (-14.5 to 11.7; 95% CI). To examine the possibility that the voltage dependence of intracellular ripple phase is due to the activation of fast voltage-gated sodium channels, we blocked their activity intracellularly using QX-314 in an additional 7 neurons (Figure 13). Intracellular QX-314 abolished sodium spikes (Grienberger et al., 2014), but had no effect on the average intracellular-LFP phase difference or its voltage dependence.

As discussed below, these results are inconsistent with models of ripple generation involving rhythmic inhibition alone. Instead, they suggest that an interplay between rhythmic

excitation leading inhibition shapes intracellular ripples in vivo (Figure 15).

2.4 Discussion

By combining in vivo whole-cell recordings from identified CA1 pyramidal neurons with nearby multisite extracellular measurements of network activity, we investigated the membrane potential dynamics underlying hippocampal ripples and found that: (1) the average membrane potential around ripples is composed of a sharp wave associated depolarization, superimposed intracellular ripple oscillations, and a post-ripple hyperpolarization. (2) Individual neurons have diverse intracellular responses, which can be partially explained by differences in membrane potential. (3) Bigger LFP sharp waves are associated with a larger post-ripple hyperpolarization and larger intracellular ripples, while the amplitude of the depolarization stays relatively constant. (4) Pyramidal neuron spikes phase-lock near the trough of LFP ripples, when the slope of the membrane potential is near its maximum. (5) The phase delay between intracellular and LFP ripples changes systematically with membrane potential.

What gives rise to the three components of the intracellular response during ripples? Ripples in CA1 are thought to be driven by excitatory input arising from a population burst spontaneously generated through the recurrent network of area CA3. Synaptic input from CA3 terminates on the apical dendrites of CA1 pyramidal neurons, and the associated synaptic currents produce a negative sharp wave in the LFP of stratum radiatum (Buzsaki, 1986). The intracellular depolarization likely reflects this excitatory input (Ylinen et al., 1995, Maier et al., 2011, English et al., 2014, Valero et al., 2015). As excitation builds up in CA1, populations of pyramidal cells and interneurons begin firing at ripple frequency, phase-

locked to LFP ripple oscillations (Buzsaki et al., 1992, Klausberger et al., 2003, Klausberger et al., 2004, Somogyi et al., 2014). Consistent with this, we observe intracellular ripple-frequency oscillations superimposed on the sharp wave associated depolarization. Inhibition also produces a hyperpolarization lasting hundreds of milliseconds beyond the end of the ripple, suggesting a dependence on GABAB receptor activation (Ulrich and Bettler, 2007, English et al., 2014). The shape of the average intracellular response varied across individual neurons. One contributing factor to this variability is differences in membrane potential through its effects on the electrical driving forces for excitation and inhibition, while other factors likely include differences in gene expression and connectivity (Lee et al., 2014). Indeed, a recent study found a difference in the ripple response between superficial and deep pyramidal cells (Valero et al., 2015), consistent with our observed neuron-to-neuron variability (Figure 3).

One key finding is that the amplitude of the intracellular depolarization is insensitive to the magnitude of the sharp wave observed in stratum radiatum. This is particularly striking because the amplitudes of the intracellular ripple and post-ripple hyperpolarization scale with sharp wave amplitude (Figure 6). This indicates the presence of a circuit mechanism that provides an intricate balance between excitation and inhibition during the ripple. In particular, larger excitatory currents must be balanced by proportional inhibitory currents during the population burst, such that the net current depolarizing the soma is independent of input strength. One way to achieve this is for inhibition to be negligible up to a threshold input magnitude, and grow at the same rate as excitation beyond this threshold (Figure 14). This would ensure that the difference between excitation and inhibition (net somatic current) would stay constant as a function of input strength. What are the cir-

cuit elements that could account for this? Area CA3 provides direct excitatory input to CA1 neurons, and proportional feed-forward inhibition through local interneurons (Alger and Nicoll, 1982, Maccaferri and Dingledine, 2002, Pouille et al., 2009). Since feed-forward interneurons will fire in proportion to CA3 input only past the threshold for spiking, the resulting inhibition is a likely candidate for the requisite inhibitory current (Mizunuma et al., 2014). Consistent with this view, at resting Vm the post-ripple hyperpolarization scales with input size, when excitation has already decayed. Furthermore, under hyperpolarizing current injection, when the inhibitory driving force for the balancing inhibition is reduced, the amplitude of the intracellular depolarization scales with sharp wave amplitude (Figure 7). For low input strengths, the post-ripple hyperpolarization is negligible, further indicating the involvement of GABAB receptors, which are selectively activated under strong stimulus intensities (Dutar and Nicoll, 1988, Ulrich and Bettler, 2007).

What controls if and when neurons fire during ripples? The intracellular depolarization during ripples in which a neuron fires is significantly larger compared to ripples in which the neuron remained silent (Figure 8). Furthermore, when neurons do not fire during ripples, they exhibit a remarkably consistent subthreshold depolarization over a wide range of input strengths, suggesting an intricate balance of excitation and inhibition as discussed above. This ensures that neurons remain silent for most ripples, and fire only when specific subsets of synapses are co-activated to overcome the balancing inhibition. Hence, the specific identity, rather than the sheer number, of active CA3 neurons likely determines whether a postsynaptic CA1 neuron fires or not. We hypothesize that the depolarization brings neurons close to firing threshold, while the superimposed intracellular ripple oscillations control the precise spike timing. Indeed, we observe that spikes preferentially occur on the

Figure 14: Conceptual model explaining a potential mechanism balancing exaction and inhibition as a function of CA3 input strength **(A)** The amplitude of the net excitatory current from direct CA3 input (green), the amplitude of feed-forward inhibition through local CA1 interneurons (red), and the total net somatic current driving CA1 pyramidal neurons (blue) are plotted as a function of CA3 input strength, as assessed experimentally using the amplitude of LFP sharp waves. Due to direct excitatory input, the amplitude of excitatory current grows linearly with input strength. Due to the fact that weak CA3 inputs won't bring CA1 interneurons to spike threshold, their output is constant up to a threshold (arrow), and grows at the same rate as excitation beyond this point. The combination of such direct excitation and indirect inhibition ensures that the total somatic current is constant above a certain threshold. Ripples are hypothesized to occur in this range, under strong input strengths. This mechanism can potentially explain why the amplitude of the intracellular depolarization is independent of input strength on average. In contrast, for a neuron to fire during a given ripple, it must receive an excitation that is much greater than the average excitation shown in green. **(B)** Diagram showing direct excitatory input onto a CA1 pyramidal neuron (blue) with feed-forward inhibition through a local CA1 interneuron (red). The output firing rate of the local CA1 interneuron is constant below a certain threshold, and grows linearly above this threshold.

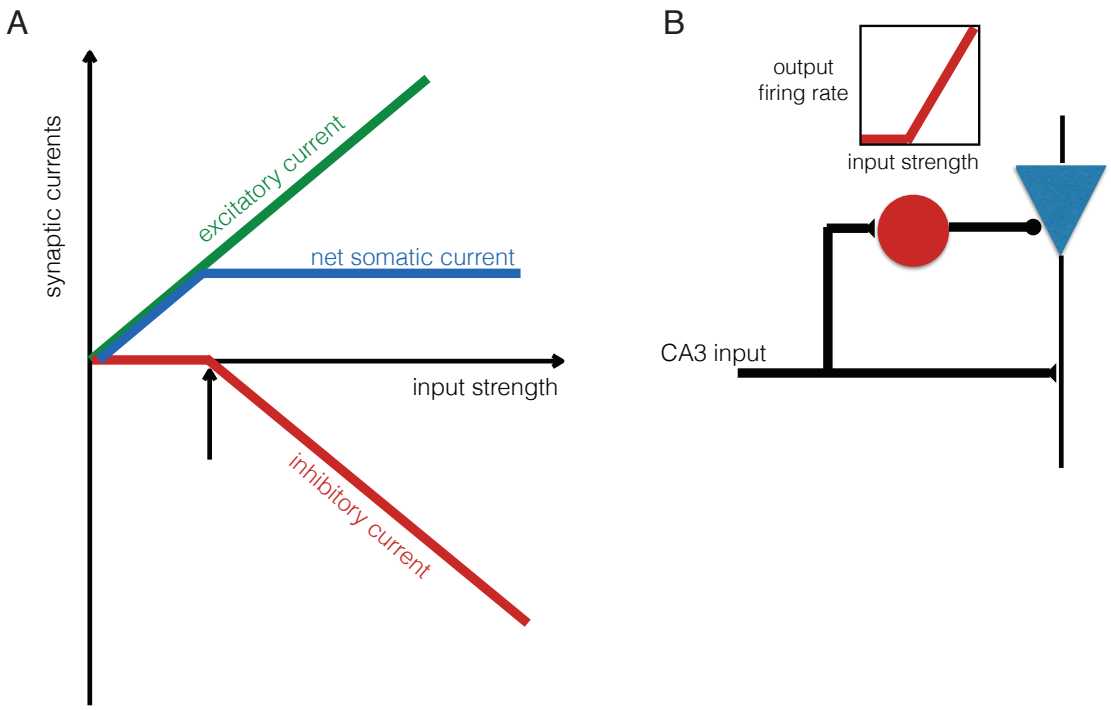

rising phase of the intracellular ripple oscillation, when the slope of the membrane potential is near its maximum. This is consistent with previous slice work showing that spike-timing precision is enhanced by fast, transient depolarizations (Mainen and Sejnowski, 1995).

How do the experimental observations fit with circuit models of ripple oscillations (Cutsuridis and Taxidis, 2013, Buzsaki, 2015, Gulyas and Freund, 2015, Patel, 2015)? Three main classes of models of ripple oscillations have been proposed, each making different predictions regarding the types of input CA1 pyramidal neurons receive. First, previous studies have proposed that the axons of CA1 pyramidal neurons are electrically coupled through sparse axo-axonal gap junctions, endowing the resulting axonal plexus with the ability to propagate action potentials and oscillate at ripple frequency (Draguhn et al., 1998, Traub and Bibbig, 2000). These models predict the presence of‘ “spikelets” representing the antidromic propagation of action potentials from ectopic generation sites to the soma. Spikelets have been demonstrated in vitro (Schmitz et al., 2001) and in vivo (Spencer and Kandel, 1961, Epsztein et al., 2010, Chorev and Brecht, 2012), but at present there is little direct evidence linking their generation to the existence of pyramidal axo-axonal gap junctions, especially during ripples in vivo (English et al., 2014). Our data do not support a role for spikelets and axo-axonal gap junctions in ripple generation, since none of our 30 neurons showed spikelets during ripples, and, unlike previous slice work (Bahner et al., 2011), hyperpolarizing current injection completely abolished spiking, arguing against an ectopic site of action potential generation.

A second class of models suggests that rhythmic perisomatic inhibition alone is responsible for intracellular ripple oscillations (Ylinen et al., 1995, Stark et al., 2014, Buzsaki, 2015). Pyramidal cells are hypothesized to receive strong ripple-frequency somatic inhi-

bition due to reciprocal interactions within interneuron networks, pyramidal-interneuron feedback loops, or both. And while several classes of interneurons, each targeting specific subcellular pyramidal cell domains, are known to be active during ripples, a prominent role for fast-spiking, parvalbumin (PV)-positive positive basket cells has emerged. Indeed, these interneurons have reciprocal connections with pyramidal cells, target their axons to the pyramidal cell soma, fire at ripple-frequency phase locked to LFP ripple oscillations, inhibit other PV-positive basket cells, and are endowed with a host of conductances supporting fast rhythmogenesis (Klausberger et al., 2003, Chiovini et al., 2014, Hu et al., 2014, Lee et al., 2014). As shown with a three-compartment conductance-based model in Figure 15, with perisomatic inhibition alone (Figure 15 B1), as the membrane potential is hyperpolarized towards the inhibitory reversal potential, the phase difference between intracellular and LFP ripple oscillations remains constant (red trace; Figure 15 D). Below this level, it abruptly flips 180 degrees, as claimed in previous work in anesthetized rats (Ylinen et al., 1995). In contrast, our data demonstrates that the phase difference varies smoothly with membrane potential, and approaches zero (rather than -90) degrees below the reversal potential for inhibition. Therefore, our data provides strong evidence against models based on perisomatic inhibition alone.

Is there a simple addition to the perisomatic inhibition model that can account for the data? Recent in vitro work has suggested that CA1 pyramidal neurons receive ripple-frequency excitation in addition to inhibition (Maier et al., 2011). Moreover, because most interneurons, including PV-positive basket cells, fire 1-2 ms after pyramidal neurons (Csicsvari et al., 1999, Klausberger et al., 2004, Sullivan et al., 2011, Varga et al., 2012, Stark et al., 2014, Varga et al., 2014), excitation should lead inhibition (Maier et al., 2011).

As shown in Figure 15 B2, with weak ripple-frequency excitation leading inhibition by 90 degrees (∼2 ms), intracellular ripples show a systematic phase shift with membrane potential. As the membrane potential is hyperpolarized towards the reversal potential for inhibition, the phase difference between intracellular and LFP ripples approaches zero (green trace; Figure 15 D), as observed experimentally (colored dots in Figure 15 D; Figure 12). This occurs because the phase of intracellular ripple oscillations depends upon the relative contribution of the excitatory and inhibitory currents, which varies with membrane potential due to corresponding changes in electrical driving force. The direction of the experimentally observed phase shift is non-trivial, as an identical model with inhibition leading excitation gives rise to a phase shift of the opposite direction. Moreover, the fact that the amplitude of intracellular ripples grows with membrane depolarization around resting Vm argues for weaker excitatory influence at the soma relative to inhibition (Figure 15 C, Figure 5). Hence, rhythmic excitation leading inhibition provides one possible explanation for the data.

What could be the source of ripple-frequency excitation? First, CA1 pyramidal neurons are known to have sparse recurrent connections (Deuchars and Thomson, 1996, Yang et al., 2014). The phase-locked firing of CA1 neurons during ripples would produce rhythmic excitatory inputs in the recurrently connected CA1 cells. In agreement with this, slice work has demonstrated that ripples and ripple-frequency excitatory post-synaptic currents (EPSCs) persist in CA1 mini-slices presumed to be devoid of CA3 input (Maier et al., 2011). Second, rhythmic excitation might also come from CA3 pyramidal neurons bursting at ripple frequency (Sullivan et al., 2011). To the extent that this input could survive passive dendritic filtering, CA3 could provide a source of ripple-frequency excitation to the soma. Third, ripple-frequency shunting inhibition may modulate slow dendritic excitation

Figure 15: A simple conductance-based model of ripple generation consistent with the experimental data (Continued on following page)

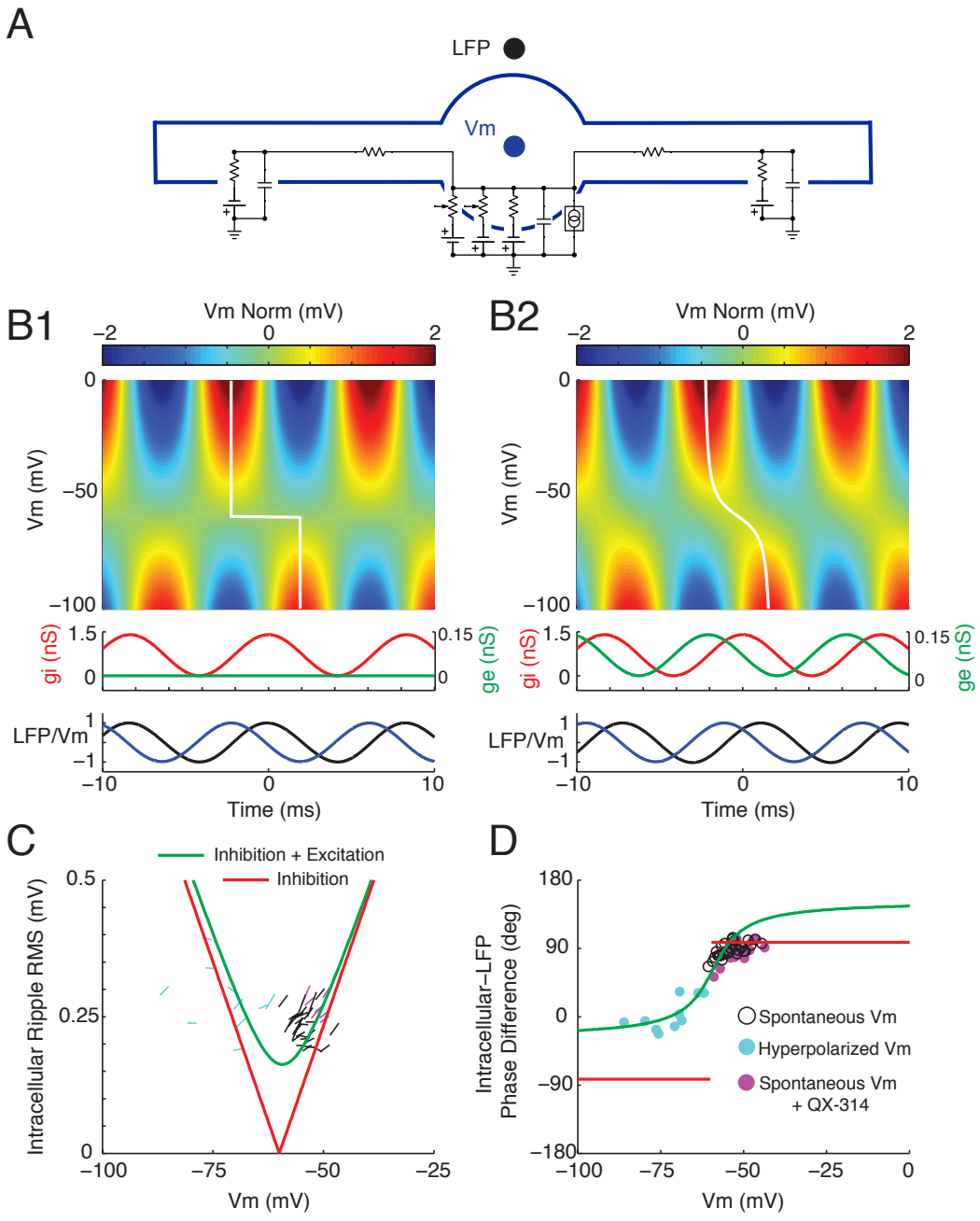

Figure 15: **(A)** Schematic of three-compartment model used in simulations (see experimental procedures). **(B1)** Model with ripple-frequency (120 Hz) perisomatic inhibition. Top: intracellular ripples as a function of Vm. Each row is normalized to have 0 mean (Vm Norm). White line marks the timing of the intracellular ripple peak for each Vm level. Middle: Perisomatic synaptic conductances. Peak inhibitory (gi) amplitude of 1.4 nS. Peak excitatory (ge) amplitude of 0 nS. Bottom: Intracellular and LFP ripples at resting Vm (-55 mV) normalized to have a peak of 1. The peak in the inhibitory conductance was used as time 0. **(B2)** Model with ripple-frequency perisomatic excitation leading inhibition. Same as in B1, but the excitatory conductance was 0.14 nS and led the inhibitory conductance by 90 degrees. Note the phase shift of intracellular ripples as a function of Vm. **(C)** Amplitude of intracellular ripples as a function of Vm for the perisomatic inhibition model from B1 (red) and the model combining excitation leading inhibition from B2 (green). The slopes of the black lines are the estimates for all 30 neurons from Figure 5. Cyan lines are slope estimates from 10 neurons during hyperpolarizing current injection. Magenta lines are slope estimates from 7 neurons with intracellular QX-314 to block voltage-gated sodium channels (Figure 13). Note that both models predict that intracellular ripples should be larger at more depolarized levels within the range of spontaneous Vm fluctuations, consistent with black lines and Figure 5. **(D)** Phase difference between intracellular ripples and LFP ripples as a function of Vm for the perisomatic inhibition model from B1 (red) and the model combining excitation leading inhibition from B2 (green). The black dots are the intracellular-LFP phase difference from Figure 12 B at the time of the central intracellular peak (-1.7 ms; middle panel). The cyan dots are the intracellular-LFP phase difference for the 10 neurons under hyperpolarizing current injection at the time of the central intracellular peak. Similarly, the magenta dots are the intracellular-LFP phase difference at spontaneous Vm levels with intracellular QX-314 from Figure 13 F. Notice that the data are consistent with the model involving rhythmic excitation leading inhibition (B2; green), but not rhythmic inhibition alone (B1; red).

to cause ripple-frequency depolarizing currents to enter the soma (but see Maier et al., 2011). Regardless of its source, our data suggests that ripple-frequency excitation plays a key role in shaping intracellular ripple oscillations, thereby contributing to the regulation of spike timing across the subset of active cells.

The proposed simple model does not capture the full complexity of the intact circuit. In particular, a number of additional factors will influence the phase of the extracellular and intracellular ripples. First, the detailed cell morphology and the precise spatiotemporal distribution of excitatory and inhibitory synaptic currents will shape both intracellular and LFP ripples. Second, active conductances can have important effects on how these synaptic inputs are integrated at the soma. Third, currents associated with the synaptic inputs and spiking of multiple nearby neurons will influence the extracellular LFP (Schomburg et al., 2012). Future studies are needed to characterize the detailed contributions of these factors.

By combining in vivo whole-cell recordings with multisite LFP measurements, we reveal the presence of a circuit mechanism providing an intricate balance between excitation and inhibition during ripples. This mechanism ensures that the majority of ripples results in only a modest subthreshold depolarization, independent of input size. In contrast, firing within a ripple requires a much larger depolarization that must be sensitive to the precise identity of CA3 inputs, as opposed to their sheer number. The spike timing within a ripple is controlled by intracellular ripple oscillations, which in turn likely depend on the combination of both ripple-frequency excitation and inhibition. This could be particularly important for determining the firing order of active cells, which has functional implications for the mechanisms of ripple-induced plasticity and the circuit mechanisms of replay.

2.5 Experimental Procedures

All animal procedures were performed in accordance with National Institute of Health guidelines and with approval of the Caltech Institutional Animal Care and Use Committee.

Head fixation surgery

Sixteen male C57Bl/6 mice (Charles River Laboratories) were surgically implanted with a lightweight, stainless steel ring embedded in dental cement, which allowed for mechanically stable head-fixation in the recording apparatus, as previously described (Froudarakis et al., 2014). A stainless steel wire was implanted over the right cerebellum. The skull was leveled and the locations of the pipette (-1.9 mm posterior, 1.5 mm lateral from Bregma) and probe exposures (-1.7 mm posterior, 2.0 mm lateral from Bregma) were marked on the skull over the left hemisphere. Following surgery, mice were returned to their home cage, maintained on a 12 hour light/dark cycle, and given access to food and water ad libitum. Ibuprofen (0.2 mg/mL) was added to the water as a long-term analgesic. Mice were given at least 48 hours to recover before the day of the experiment.

Exposure surgery

On the day of the experiment, mice (age P28 to P37) first underwent a short surgery to expose the brain. While anesthetized with 1% isoflurane and head-fixed in the stereotaxic apparatus, two small exposures were drilled (pipette: 500 μm diameter; probe: 200 μm diameter) over the left hippocampus at the previously marked locations. A recording chamber was secured on top of the head-fixation device and filled with pre-oxygenated (95% O2, 5% CO2), filtered (0.22 μm) artificial cerebrospinal fluid (aCSF) containing (in mM): 125 NaCl, 26.2 NaHCO3, 10 Dextrose, 2.5 KCl, 2.5 CaCl2, 1.3 MgSO4, 1.0 NaH2PO4.

Awake, in vivo recordings

Mice were head-fixed on top of a spherical treadmill secured on an air table (TMC). The ball could rotate along a single axis, allowing the mice to run and walk freely. On either side of the ball, two platforms supporting micromanipulators (Sutter Instrument Company) allowed for precise positioning of a silicon probe (mouse's left) and glass pipettes (mouse's right). A single-shank, 32-site silicon probe (NeuroNexus) with 100 μm site spacing was inserted in the coronal plane ($\sim$ 15 degree angle pointing towards the midline) to a depth of 2600-3000 μm. Sites spanned all of neocortex, area CA1, the dentate gyrus, and parts of the thalamus. The probe was adjusted so that a recording site was positioned within the CA1 pyramidal cell layer for reliably recording LFP ripple oscillations. Sharp waves were evident on the sites spanning stratum radiatum. The probes were grounded to the recording table and referenced to a wire implanted over the cerebellum.

To find the depth of the CA1 cell layer and compare the structure of LFP ripples recorded on the probe versus those from a pipette, we used artificial cerebrospinal spinal fluid (aCSF) filled pipettes to perform one to three juxtacellular (Pinault, 1996) recordings per mouse from putative CA1 pyramidal neurons (N=28). Long-taper pipettes (for juxtacellular and whole-cell recordings) were pulled from borosilicate capillaries (OD: 1.0 mm, ID: 0.58 mm; Sutter Instrument Company) using a Model P-2000 puller (Sutter Instrument Company) to an inner tip diameter of $\sim$0.8-1.5 μm and outer diameter of $\sim$2 μm (5-8 MΩ), and inserted into the brain in the coronal plane with a $\sim$15 degree angle pointing away from the midline. The location of the CA1 layer was signaled by the occurrence of large amplitude ripples that appeared synchronously on the pipette and probe site in the CA1 cell layer. At the depth of the CA1 layer, the probe and patch pipette were separated by approximately 200 μm in the anterior-posterior direction and 100 μm in the medial-lateral. The pipette was advanced

at 1-2 μm/s until a putative CA1 pyramidal neuron was encountered, which was evident from the appearance of complex spikes and ripple-associated action potentials. Recordings (juxtacellular and whole-cell) were made with a MultiClamp 700B amplifier (Molecular Devices). For juxtacellular recordings, the capacitance neutralization circuit was off and the output was AC coupled and amplified 100x.

Whole-cell recordings were performed after the depth of the CA1 layer had been identified. Pipettes were filled with an internal solution containing (in mM): 115 K-Gluconate, 10 KCl, 10 NaCl, 10 Hepes, 0.1 EGTA, 10 Tris-phosphocreatine, 5 KOH, 13.4 Biocytin, 5 Mg-ATP, 0.3 Tris-GTP. The internal solution had an osmolarity of 300 mOsm and a pH of 7.27 at room temperature. In a subset of experiments (Figure 13), 2 mM of QX-314 (Tocris) was added to the internal solution to block voltage-gated sodium channels. The membrane potential was not corrected for the liquid junction potential. Whole-cell recordings were obtained "blind" according to previously described methods (Margrie et al., 2002) in current clamp mode (Schramm et al., 2014). Capacitance neutralization was set prior to establishing the GΩ seal. After obtaining the whole-cell configuration, the neuron's membrane potential was recorded in current clamp mode. Access resistance was estimated online by fitting the voltage response to hyperpolarizing current steps (see below). Recordings were aborted when the access resistance exceeded 120 MΩ or the action potential peak dropped below 0 mV. One to five whole-cell recordings (N=37) were performed per mouse.

Signal acquisition

All electrophysiological signal acquisition was performed with custom Labview software (National Instruments) that we developed. Electrophysiological signals were sampled simultaneously at 25 kHz with 24 bit resolution using AC (PXI-4498, internal gain: 30 dB,

range: +/- 316 mV) or DC-coupled (PXIe-4492, internal gain: 0 dB, range: +/- 10 V) analog-to-digital data acquisition cards (National instruments) with built-in anti-aliasing filters for extracellular and intracellular/juxtacellular recordings, respectively.

Histology and imaging

Following the experiment, mice were deeply anesthetized with 5% isoflurane, decapitated, and the brain extracted to 4% PFA. Staining of biocyin-filled cells for morphological identification was performed according to previously described methods (Horikawa and Armstrong, 1988). Brains were fixed at 4 C in 4% paraformaldehyde overnight and transferred to 0.01 M (300 mOsm) phosphate buffered saline (PBS) the next day. Up to one week later, brains were sectioned coronally (100 μm) on a vibrating microtome (Leica), permeabilized with 1% Triton X-100 (v/v) in PBS for 1-2 h, and incubated overnight at room temperature in PBS containing avidin-fluorescein (1:200, Vector Laboratories), 5% (v/v) normal horse serum (NHS), and 0.1% Triton X-100. Sections were rinsed in PBS between each step. The next day, sections containing biocytin stained neurons were identified on an inverted epifluorescent microscope (Olympius IX51) for further immunohistochemical processing.

To aid in classifying recorded neurons as CA1 pyramidal neurons, we performed immunohistochemical staining against calbindin (CB) and parvalbumin (PV). Sections containing biocytin-stained neurons were first incubated in blocking solution containing 5% NHS, 0.25% Triton X-100, and 0.02% (wt/v) sodium azide in PBS. Next, slices were incubated in PBS containing primary antibodies against CB (Rabbit anti-Calbindin D-28k, 1:2000, Swant) and PV (Goat anti-parvalbumin, 1:2000, Swant) overnight. After thorough rinsing in PBS, slices were incubated in PBS containing secondary anitbodies CF543 don-

key anti-rabbit (1:500, Biotium) and CF633 donkey anti-goat (1:500, Biotium). Processed slices were rinsed and mounted in antifading mounting medium (EverBrite, Biotium).

Stained slices were imaged on an inverted confocal laser-scanning microscope (LSM 710, Zeiss). Biocytin-stained neurons were unambiguously classified as CA1 pyramidal neurons if their soma was located in the CA1 pyramidal cell layer, showed a morphology characteristic of these neurons (bifurcating apical dendrites, dendritic spines, etc.), had PV-negative soma, and showed electrophysiological properties consistent with CA1 pyramidal neurons.

Measuring and setting access resistance

Access resistance was estimated online using custom-written software in Labview that communicated with the software (Commander, Molecular Devices) controlling the Multi-Clamp 700B amplifier through an application programming interface (API). To estimate the access resistance, the bridge balance was temporarily turned off. Then, two -100 pA current pulses (250 ms duration, 250 ms inter-pulse interval) were delivered, the first 50 ms of the hyperpolarizing voltage responses was fit using a simple model, and if the r^2 fit exceeds 0.99, the bridge balance was set to its new value, otherwise it was returned to the previous value. This procedure was performed once every minute during whole-cell recordings. In addition, all recording parameters in the Commander software were acquired once every second using the API, time stamped to electrophysiological signals, and saved for offline review. The pipette's voltage response to hyperpolarizing current steps was fit online using a simple double exponential model (Anderson et al., 2000). The computational simplicity of this model sped online fitting. For offline estimates, we used a biophysically-inspired, single-compartment model (de Sa and MacKay, 2001). The results obtained from the two models were nearly identical under our recording conditions.

Ripple detection

All offline analysis was performed in Matlab (MathWorks). LFP ripple oscillations were detected as transient increases in ripple-band power from the probe site located in the CA1 pyramidal cell layer. To compute ripple band power, LFPs were filtered between 80-180 Hz (Parks-McClellan optimal equiripple FIR filter, 80-180 Hz pass band, 50-80 and 180-200 Hz transition bands, 60 dB minimum attenuation in the stop bands), the ripple-band envelope was computed as the instantaneous amplitude from the Hilbert transform, and the envelope was low-pass filtered (Parks-McClellan optimal equiripple FIR filter, 20-30 Hz transition band, 40 dB minimum attenuation in the stop bands). From this signal, an upper threshold was set as 4.5-5.5 times the median. A lower threshold was set as half the upper threshold. Ripples were detected as peaks in the ripple band envelope above the upper threshold, and with time between positive-going and negative-going lower threshold crossings longer than 30 ms. Ripples meeting these criteria, but with peaks less than 60 ms, apart were merged. The time of ripple occurrence was defined as the sample with the largest amplitude (positive peak) in the ripple band within the detected ripple and used as time 0 for all plots (ripple center).

Having multiple extracellular recording sites aided in ripple detection for several reasons. First, it allowed us to precisely position a single LFP electrode in the CA1 pyramidal cell layer based on the well-known inversion of sharp wave polarity across the cell layer. Second, it allowed us to confirm that the detected ripples were localized to the CA1 pyramidal cell layer, which helps exclude electrical artifacts. Third, it enabled monitoring LFPs across the neocortex and hippocampal subfields to confirm that the whole network was in a healthy state, as established by previous multisite recordings.

Quantification of intracellular and LFP waveforms

To quantify the intracellular response during ripples, we computed the change in subthreshold Vm relative to baseline in short time windows for the pre-ripple ramp (-150 to -100 ms), the sharp wave associated depolarization (-5 to 5 ms), and the post-ripple hyperpolarization (75 to 125 ms). The baseline Vm was subtracted from the median Vm in each component's time window to yield the component's amplitude. For neuron averaged (Figure 3) and block-averaged (Figure 6) Vm waveforms, the baseline Vm was defined as the average from -2 to -1.5 s. For intracellular ripples, the baseline was defined as the average Vm from -25 to 25 ms (Figure 5). To quantify the amplitude of intracellular ripple and LFP ripples, the root mean square of the ripple-band signal was computed from -25 to 25 ms.

The instantaneous phase, frequency, and power of juxtacellular, LFP, and intracellular ripples were measured using the continuous wavelet transform and complex Morlet wavelets with central frequencies from 60 to 200 Hz in 0.025 Hz steps and a length of 5 cycles. For each sample, the frequency with the largest power was identified and its phase and frequency taken as the waveform's instantaneous value. For Figure 10 B-E and Figure 11, the instantaneous estimates were Gaussian smoothed ($\sigma = 1$ ms). 8 neurons were excluded from Figure 10 B-E due to poor instantaneous estimates in the beginning or end of the $\pm$ 20 ms window, though this did not change the major results, as evidence from Figure 10 F-H, which includes all neurons.

Intracellular spike detection and subthreshold Vm calculation

Spikes from whole-cell recordings were detected as peaks greater than 10 mV after high-pass filtering the Vm (Parks-McClellan optimal equiripple FIR filter, 20-50 Hz transition

band, 40 dB minimum attenuation in the stop bands). The subthreshold membrane potential was compute by linearly interpolating periods with action potentials from 3 ms before to 5 ms after the spike peak. For spikes occurring within 20 ms of each other, as during complex bursts, the first spike was linearly interpolated from 3 ms before its peak until the sample showing the minimum value before the next spike. This procedure provided a lower bound on complex spike waveforms, effectively revealing the slow, depolarizing component underlying them while excluding fast action potential waveforms (Epsztein et al., 2011). Following linear interpolation, the signals were low-pass filtered (Parks-McClellan optimal equiripple FIR filter, 250-350 Hz transition band, 40 dB minimum attenuation in the stop bands).

Juxtacellular spike detection

Juxtacellular spikes were detected as peaks greater than 0.25 mV after high-pass filtering (Parks-McClellan optimal equiripple FIR filter, 60-80 Hz transition band, 40 dB minimum attenuation in the stop bands). Single-unit isolation and stable spike waveform were confirmed offline.

Conductance-based Vm/LFP model

The conductance-based "ball-and-stick" model (Figure 15 A) was composed of a spherical perisomatic compartment with a radius of 10 μm and cylindrical apical and basal dendritic compartments with 2 μm radii and lengths of 50 μm. 50 μm separated the center of the perisomatic compartment and the center of the dendritic compartments, giving rise to an axial resistance of 2.8 MΩ (intracellular resistivity = 0.7 Ω-m). Each compartment contained a resting conductance with a reversal potential of -55 mV and a magnitude given by the ratio of its surface area and the specific membrane resistance (15 kΩ-cm^2). Similarly,

each compartment had a capacitance given by the product of its surface area and the specific membrane capacitance (1 μF/cm^2). Additionally, the perisomatic compartment had an excitatory synaptic conductance with a reversal potential of 10 mV and an inhibitory synaptic conductance with a reversal potential of -60 mV. These synaptic conductances served as the source of ripple-frequency (120 Hz) input to the model. To assess the dependence of intracellular ripple phase on Vm, the model was run at perisomatic Vm ranges from -150 to 50 mV in steps of 0.5 mV accomplished through DC current injection into the perisomatic compartment (Figure 15 B1-B2), as done experimentally (Figure 12 C). Using the model with zero DC current injection, the LFP at an electrode 50 μm from the perisomatic compartment and equidistance from the dendritic compartments (ie in the middle of the "cell layer") was calculated using the transmembrane currents from each compartment at each point in time. The extracellular space was assumed to be isotropic, uniform, and purely resistive (ohmic) with a resistivity of 0.333 Ω-m. The perisomatic compartment was approximated as a point source of current, while the dendritic compartments were approximated as line sources (Holt and Koch, 1999, Einevoll et al., 2013).

Statistical analysis

To assess the significance of pre-ripple ramping in the neuron-averaged, ripple-triggered Vm traces (Figure 3 C), 95% confidence intervals on the Vm were constructed at each sample from -2 s to 2 s. Pre-ripple confidence intervals were computed as the average of the upper/lower 95% confidence intervals from -2 to -1.5 seconds. The mean Vm was considered significantly different ($p<0.05$) from baseline if it went above/below the upper/lower baseline confidence intervals. Neurons were considered to have significant ramps if their average Vm spent at least 150 ms continuously above or below the 95% baseline confidence

intervals between -1 s and -100 ms. Linear regression was used to estimate the relationship between baseline Vm and component amplitudes (Figure 3), LFP ripple power and frequency (Figure 10 F), LFP and intracellular ripple frequency (Figure 10 G), and Vm and intracellular ripple phase (Figure 12 B). Least squares estimates of the slope (β) were used to assess significance at the $p<0.05$ level, except for Figures 5 and 6, which employed robust regression implemented using iteratively reweighted least squares and a bisquare weighting function on the residuals to mitigate the effect single ripple outliers. Averages are reported as mean $\pm$ standard error of the mean (SEM) unless otherwise stated. All circular statistics were performed using the CircStat toolbox (Berens, 2009).

3 Brain State Dependence of Hippocampal Subthreshold Activity in Awake Mice

3.1 Summary

Intracellular recordings of subthreshold activity in vivo have greatly contributed to our understanding of the cellular mechanisms underlying state-dependent processing in neocortex. In contrast, the modulation of the membrane potential of hippocampal neurons by brain state has not been systematically characterized. To address this, we combined in vivo whole-cell recordings from identified dentate granule cells and CA1 pyramidal neurons with multisite extracellular recordings and behavioral measurements in head-restrained mice. We show that membrane potential statistics (mean, variability, distance to threshold) are systematically modulated across brain states. Furthermore, within individual states, rapid variations in pupil diameter are reflected in membrane potential fluctuations. Finally, many neurons exhibit ramps in the membrane potential starting approximately one second before ripples, mirroring transitions to a network regime conducive for ripple generation. These results provide evidence that coordinated shifts in the subthreshold dynamics of individual neurons may contribute to the emergence of hippocampal activity patterns characteristic of different brain states.

3.2 Introduction

Brain circuits exhibit distinct modes of activity (brain states) that reflect complementary computational processes (Loomis et al., 1937, Saper et al., 2010, Harris and Thiele, 2011). The circuit mechanisms regulating brain state have been the subject of intense investigation

(Moruzzi and Magoun, 1949, Lee and Dan, 2012), and recent studies in neocortex have found rapid state changes in awake, behaving animals with behaviorally-relevant effects on the spiking patterns and encoding abilities of sensory and motor regions (Vyazovskiy et al., 2011, Reimer et al., 2014, McGinley et al., 2015b). Importantly, intracellular recordings of subthreshold activity during behavior have been instrumental in elucidating the cellular mechanisms contributing to the emergence of network activity patterns (Steriade et al., 2001, Poulet and Petersen, 2008, Polack et al., 2013, McGinley et al., 2015a, Schiemann et al., 2015). In contrast, the brain state-dependence of hippocampal subthreshold activity has not been systematically characterized in behaving animals.

The hippocampal formation plays a critical role in spatial navigation and the encoding, consolidation, and retrieval of new episodic memories (Squire, 1992), with different brain states thought to contribute differentially to each process. Because of this, state-dependent patterns of spiking and local field potential (LFP) oscillations have been studied extensively in the hippocampal formation (Vanderwolf, 1969, Vanderwolf, 1971, O'Keefe and Nadel, 1978, Buzsaki et al., 1983, Buzsaki et al., 1992, Wilson and McNaughton, 1994, Lubenov and Siapas, 2009, Kay et al., 2016). During wakefulness, periods of locomotion are associated with robust theta (5-12 Hz) and gamma (30-80 Hz) oscillations in the LFP. In this state, individual principal neurons, known as place cells, fire at particular spatial locations and are largely silent otherwise (O'Keefe, 1976). It has been hypothesized that memory encoding preferentially occurs during this state (Buzsaki, 1989). During quiet wakefulness, the hippocampal LFP is characterized by large irregular activity (LIA), during which trains of sharp waves often co-occur with high-frequency (80-250 Hz) ripple oscillations (Vanderwolf, 1969, O'Keefe, 1976, Buzsaki, 1986). Sharp-wave/ripples (SWRs) are

associated with population bursts that "replay" previously experienced spatial trajectories (Lee and Wilson, 2002, Foster and Wilson, 2006, Diba and Buzsaki, 2007). These replay events are hypothesized to contribute to the consolidation and retrieval of newly formed episodic memories (Carr et al., 2011). In addition to the theta and LIA states, a third state exists, during which LFPs show a decline in broadband power. This state is termed small irregular activity (SIA; Vanderwolf, 1971, O'Keefe and Nadel, 1978, Jarosiewicz and Skaggs, 2004, Kay et al., 2016), though other terms have also been used (Lapray et al., 2012, Katona et al., 2014). During periods of SIA, most principal cells stop firing, while a small subset fire robustly and may code for spatial position in the absence of locomotion (Jarosiewicz et al., 2002, Jarosiewicz and Skaggs, 2004, Kay et al., 2016). In addition to principal cells, recent work also finds strong state-dependent firing patterns in identified hippocampal interneurons during LIA, SIA, and Theta (Somogyi et al., 2014).

These findings come largely from experiments employing extracellular recording techniques. While such recordings provide valuable information regarding state-dependent neuronal firing patterns, intracellular measurements can reveal how individual neurons integrate inputs to contribute to network activity. For this reason, subthreshold activity has been investigated during ripples (Maier et al., 2011, English et al., 2014, Hulse et al., 2016) and theta/gamma oscillations (Harvey et al., 2009, Epsztein et al., 2011, Pernia-Andrade and Jonas, 2014, Bittner et al., 2015, Fuhrmann et al., 2015). Yet, the variation in membrane potential dynamics of single hippocampal neurons across states has not been systematically characterized. This characterization is of fundamental importance because the resting membrane potential and the amplitude of ongoing subthreshold fluctuations affect the recruitment of neurons by controlling the amount of depolarization required to bring them

to spike threshold. This, in turn, can contribute to the emergence of network patterns characteristic of different brain states. Finally, recent experiments in neocortex have found that rapid fluctuations in pupil diameter, reflecting the level of arousal, impact neocortical subthreshold activity during quiet wakefulness (Reimer et al., 2014, McGinley et al., 2015b). The influence of such changes on hippocampal subthreshold dynamics is unknown.

Here, we performed in vivo whole-cell recordings of the membrane potential (Vm) from identified dentate granule cells and CA1 pyramidal neurons during LIA, SIA, and theta states in awake mice. Using this approach, we demonstrate that hippocampal subthreshold activity is systematically modulated by brain state. In addition, we observe rapid fluctuations in pupil diameter, even within sustained periods of LIA, that are reflected in subthreshold activity changes. Finally, many neurons exhibit ramps in the membrane potential starting approximately one second before ripples, reflecting transitions to a network regime conducive for ripple generation.

3.3 Results

Differences in Membrane Potential Statistics Across Brain States

To investigate how hippocampal subthreshold activity changes with brain state, we combined whole-cell recordings from identified dentate granule cells and CA1 pyramidal neurons with simultaneous LFP measurements from a nearby multisite silicon probe in awake, head-fixed mice that were free to walk on a spherical treadmill (Figure 16 A-C, Hulse et al., 2016). Concurrently, behavioral activity was tracked by measuring locomotor velocity, whisking activity, and pupil diameter. LFP sites spanned neocortex, hippocampal area CA1 and the dentate gyrus (DG), and parts of thalamus. We identified periods of wakefulness

Figure 16: The subthreshold activity of hippocampal principal cells varies with brain state in awake mice (Continued on following page)

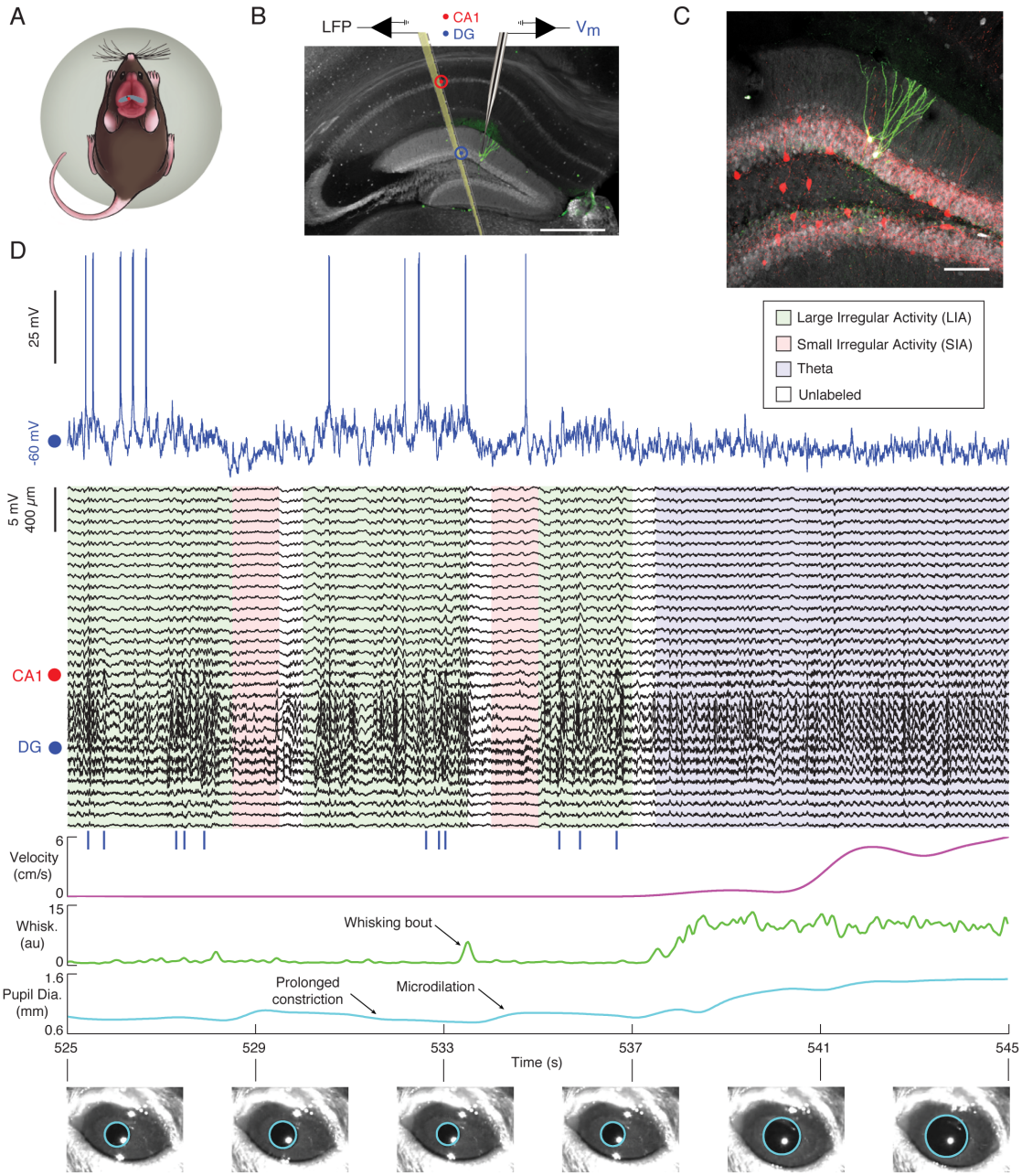

Figure 16: **(A)** Schematic of a mouse on the spherical treadmill. The approximate whole-cell (red dot) and LFP (black dot) recording locations are marked over dorsal hippocampus (blue). **(B)** Fluorescent image of 100 μm thick coronal section of dorsal hippocampus with two stained dentate granule cells (green) and immunohistochemistry against calbindin (gray) illustrating the placement of the multisite silicon probe and patch pipette. The scale bar is 500 μm. **(C)** Confocal image from section in (B) showing the two biocytin stained dentate granule cells (green) with combined immunohistochemistry against parvalbumin (red) and calbindin (gray). The scale bar is 100 μm. **(D)** Example of simultaneous intracellular (blue), multisite LFP (black), locomotor velocity (magenta), whisking (green), and pupil diameter (cyan) measurements during a period with LIA , SIA, and Theta. The legend lists each state's coloring in the LFP plot below. The red dot marks the channel within the CA1 pyramidal cell layer showing LFP ripple oscillations. Blue vertical lines below LFPs mark ripples. The blue dot marks an LFP channel in the DG. Example pupil fits are shown below.

as LIA (37%), SIA (6%), or Theta (6%) based on the spectral content of hippocampal LFPs, leaving the remaining 51% unlabeled (Figure 19 B; see methods). The objective was to identify prototypical segments of sufficient duration, as opposed to providing an exhaustive brain state assignment over the whole recording period. We then studied changes in subthreshold activity and behavior during transitions to and within periods of LIA, SIA, and Theta.

Figure 16 D shows an example whole-cell recording from a dentate granule cell with simultaneous LFP and behavioral measurements during a period with LIA, SIA, and Theta. Notice that, during periods of LIA, the pupil is constricted (or constricting), whisking and locomotor activity are low, and the hippocampal LFP shows trains of large amplitude sharp waves often co-occurring with high-frequency ripple oscillations in the CA1 pyramidal cell layer. The membrane potential appears depolarized and has large amplitude fluctuations, occasionally exceeding spike threshold. In this example, LIA was interrupted by two brief ($\sim$1 s) periods of SIA that were associated with whisking bouts and a microdilation of the pupil. During these SIA epochs, the Vm appears hyperpolarized. The segment ends with a period of theta oscillations associated with locomotion, high whisking activity, and

a dilated pupil. During this period, the membrane potential was at an intermediate level of depolarization and variability, compared to LIA and SIA. In order to investigate how general these trends were across neurons, we recorded dentate granule cells (n=20) and CA1 pyramidal neurons (n=31) across a total of 13.4 hours of spontaneous activity and studied the behavioral variables and Vm during transitions to LIA, SIA, and Theta (Figures 17, 18, and 19).

During transitions to LIA, most hippocampal neurons depolarized and the amplitude of their subthreshold fluctuations increased (Figure 17). To assess the significance of these changes, we compared the average Vm before and after transitions to LIA for each neuron individually. Most neurons significantly depolarized during transitions to LIA (n=19/20 DG; n=22/31 CA1) and a small subset significantly hyperpolarized (n=1/20 DG; n=2/31 CA1; $p<0.05$, Wilcoxon signed-rank tests). In order to assess the magnitude of subthreshold fluctuations, we first computed the standard deviation of the membrane potential irrespective of brain state. By this measure, granule cells had a larger total Vm variability (6.3 ± 0.9 mV) than CA1 pyramidal neurons (4.7 ± 0.6 mV), but these values include contributions from state-dependent shifts in the average Vm, in addition to subthreshold fluctuations. To isolate the subthreshold fluctuations from slower changes in the average Vm, we high-pass filtered the membrane potential and compared the standard deviation of the filtered trace before and after transitions to LIA. Similar to the average Vm, most neurons showed a significant increase in Vm variability after transitions to LIA (n=17/20 DG; n=25/31 CA1), while one showed a significant decrease (n=0/20 DG; n=1/31 CA1; $p<0.05$, Wilcoxon signed-rank tests). We also found notable differences between CA1 pyramidal neurons and DG granule cells. Specifically, during LIA, dentate granule cells were

Figure 17: LIA is associated with a depolarized membrane potential and large subthreshold fluctuations **(A)** Top panel shows a spectrogram of the average LFP power (z-score by frequency) triggered on transitions to LIA, which occur at time 0. Bottom panels show the average velocity, whisking, and pupil diameter (shaded regions mark mean ± SEM). Note that transitions to LIA were associated with an increase in delta (0.5-3.5 Hz) and beta (10-20 Hz) LFP power. **(B)** Scatter plots of median velocity, whisking, and pupil diameter before (Pre-LIA) and after the transition (LIA). Each point comes from a single transition. The axes labels list the time windows used for computing median values. Locomotor velocity (n=2729 transitions), whisking (n=2695 transitions), and pupil diameter (n=973 transitions) all showed a significant decrease across transitions to LIA ($p<0.001$, Wilcoxon signed-rank tests). **(C)** Left panel shows the membrane potential of granule cells triggered on transitions to LIA. Each row corresponds to a single transition, with Vm normalized by subtracting the mean from -2 to 0 s. White lines on the right separate different single neurons. The rows were sorted by each neuron's average Vm change during transitions to LIA. The right panel shows the same for CA1 pyramidal neurons. **(D)** The top left panel shows the average Vm in red (black shaded region marks mean ± SEM) triggered on transitions to LIA for a single neuron marked by the red square in (C). Grey Vm traces come from two example transitions. The top right panel shows the average Vm from the same neuron, but zoomed in to better illustrate the change occurring during LIA transitions. Two other example neurons are shown below. **(E)** The left panel shows a scatter plot of mean Vm before (Pre-LIA) versus after (LIA) transitions to LIA. Each point is the average from a single neuron. Dentate granule cells are colored blue, with filled circles marking neurons with significant changes in Vm. CA1 pyramidal neuron averages are marked in red. Similarly, the right panel shows the mean standard deviation of the Vm (high-pass filtered above 5 Hz) before and after transitions to LIA. Axis labels list the time windows used for computing means.

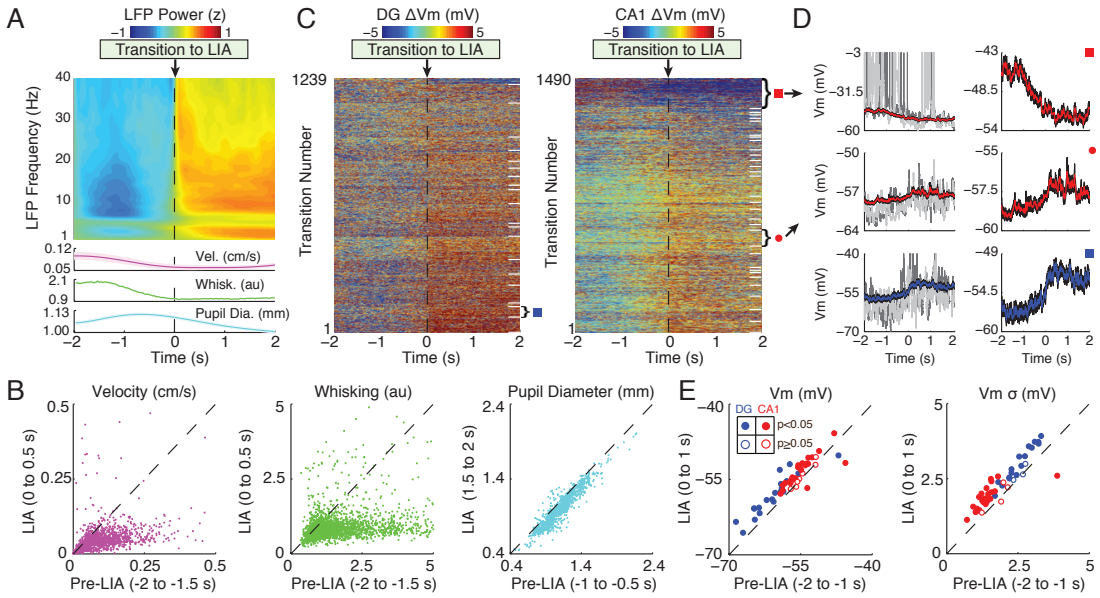

Figure 18: SIA is associated with a hyperpolarized membrane potential and small subthreshold fluctuations **(A)** The top panel shows a spectrogram of the average LFP power (z-score by frequency) triggered on transitions to SIA, which occur at time 0. The bottom panels show the average velocity, whisking, and pupil diameter (shaded regions mark mean ± SEM). Note that transitions to SIA are associated with a broadband decrease in LFP power. **(B)** Scatter plots of median velocity, whisking, and pupil diameter before (Pre-SIA) compared to after the transition (SIA). Each point comes from a single transition and axes labels list the time windows used for computing median values. Locomotor velocity (n=1856 transitions; mostly reflecting postural adjustments), whisking (n=1825 transitions), and pupil diameter (n=558 transitions) all showed a significant increase across transition to SIA ($p<0.001$, Wilcoxon signed-rank tests). **(C)** The left panel shows the membrane potential of granule cells triggered on transitions to SIA. Each row corresponds to a single transition and Vm was normalized by subtracting the mean from -2 to 0 s. White lines on the right separate different single neurons. The rows were sorted by each neuron's average Vm change during transitions to SIA. The right panel shows the same for CA1 pyramidal neurons. **(D)** The top left panel shows the average Vm in blue (black shaded region marks mean ± SEM) triggered on transitions to SIA for a single neuron marked by the blue circle in (C). Grey Vm traces come from two example transitions. The top right panel shows the average Vm from the same neuron, but zoomed in to better illustrate the change occurring during SIA transitions. Two other example neurons are shown below. **(E)** The left panel shows a scatter plot of the mean Vm before (Pre-SIA) compared to after (SIA) transitions to SIA. Each point is the average from a single neuron. Dentate granule cells are colored blue, with filled circles marking neurons with significant changes in Vm. CA1 pyramidal neuron averages are marked in red. Similarly, the right panel shows the mean standard deviation of the Vm (high-pass filtered above 5 Hz) before and after transitions to SIA. Axis labels list the time windows used for computing means.

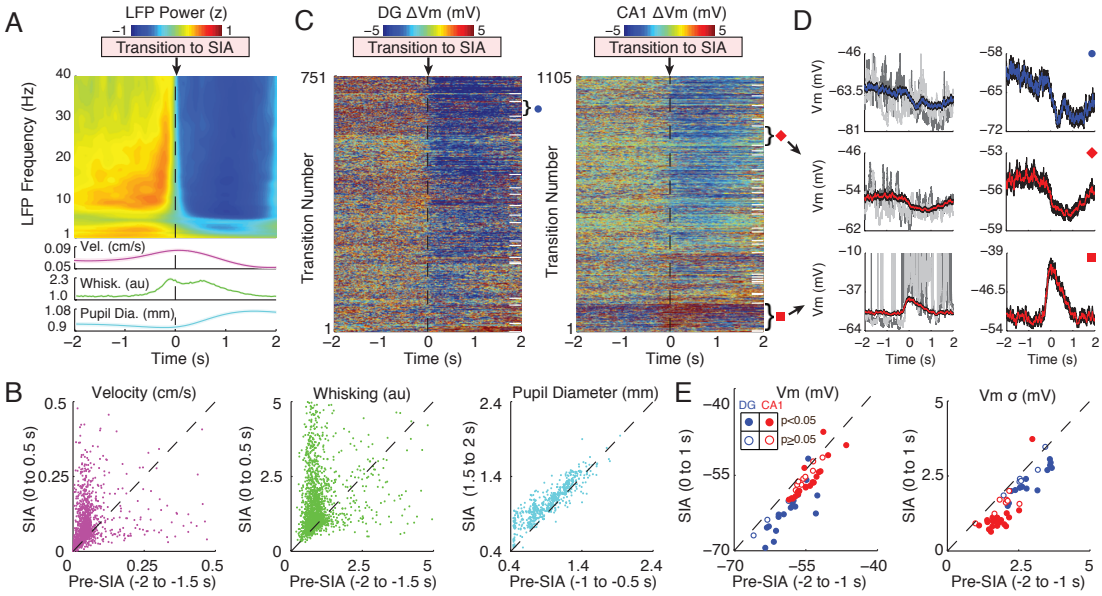

more hyperpolarized and had larger Vm fluctuations (Vm = -58.1 ± 0.9 mV, σ = 3.0 ± 0.1 mV) compared to CA1 pyramidal cells (Vm = -53.6 ± 0.5 mV, σ = 1.9 ± 0.1 mV, $p<0.001$). Across transitions to LIA, granule cells depolarized more than CA1 pyramidal neurons (DG ΔVm = 2.5 ± 0.5 mV; CA1 ΔVm = 1.2 ± 0.3 mV, $p<0.05$), with a similar increase in Vm variability (DG $\Delta\sigma$ = 0.4 ± 0.05 mV; CA1 $\Delta\sigma$ = 0.4 ± 0.07 mV; p=0.60; Mann-Whitney U tests).

Changes in Vm across transitions to SIA were largely opposite to those associated with transitions to LIA (Figure 18). Overall, most neurons significantly hyperpolarized across transitions to SIA (n=17/20 DG; n=20/31 CA1), but a few significantly depolarized (n=1/20 DG; n=2/31 CA1; $p<0.05$, Wilcoxon signed-rank tests). Similarly, most neurons showed a significant decrease in Vm variability (n=14/20 DG; n=22/31 CA1; $p<0.05$). During SIA, dentate granule cells were more hyperpolarized and had larger Vm fluctuations (Vm = -62.5 ± 1.0 mV; σ = 2.4 ± 0.1 mV) compared to CA1 pyramidal neurons (Vm = -55.9 ± 0.6 mV; σ = 1.2 ± 0.1 mV; $p<0.001$). Across transitions to SIA, dentate granule cells hyperpolarized more than CA1 pyramidal neurons (DG ΔVm = -3.3 ± 0.6 mV; CA1 ΔVm = -1.2 ± 0.3 mV; $p<0.002$) with a similar decrease in Vm variability (DG $\Delta\sigma$ = -0.5 ± 0.07 mV; CA1 $\Delta\sigma$ = -0.6 ± 0.07 mV; p=0.13, Mann-Whitney U tests). In addition, the more a neuron hyperpolarized across transitions to SIA, the more it tended to depolarize across transitions to LIA (R^2=0.78, $p<0.001$; Figure 19 C).

While transitions to Theta were associated with an increase in locomotor velocity, whisking, and pupil diameter, there were no significant changes in Vm or its variability across the transitions (Figure 19 A). Since Theta periods tended to occur away from identified LIA and SIA epochs, the resting Vm and the amplitude of subthreshold fluctuations during

Figure 19: Behavioral measures and subthreshold activity during transitions to Theta (Continued on following page)

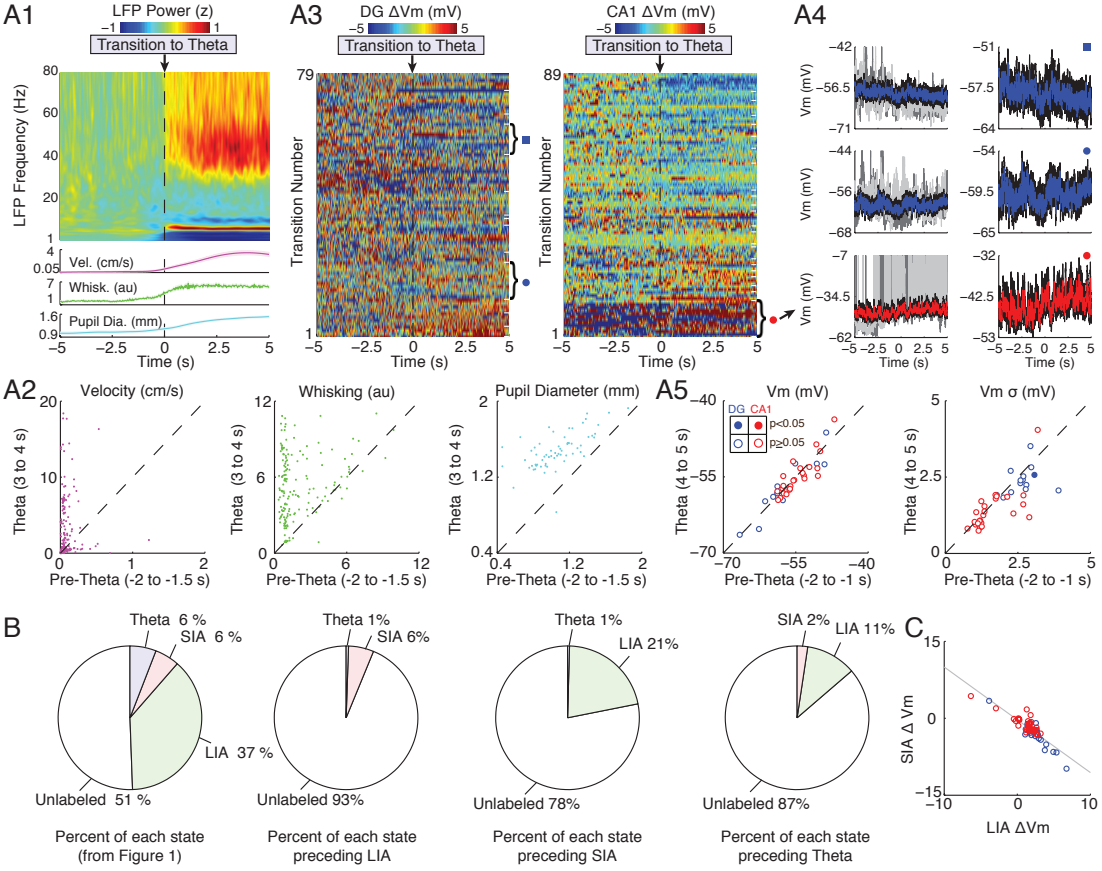

Figure 19: **(A1)** Top panel shows a spectrogram of the average LFP power (z-score by frequency) triggered on transitions to Theta, which occur at time 0. Bottom panels show the average velocity, whisking, and pupil diameter (shaded regions mark mean ± SEM). Note that transitions to Theta were associated with an increase in theta and gamma power. **(A2)** Scatter plots of median velocity, whisking, and pupil diameter before (Pre-Theta) compared to after (Theta). Each point comes from a single transition. Locomotor velocity (n=168 transitions), whisking (n=163 transitions), and pupil diameter (n=63 transitions) all showed a significant increase across transitions to Theta ($p<0.001$, Wilcoxon signed-rank tests). **(A3)** Left panel shows the membrane potential of granule cells triggered on transitions to Theta. Each row corresponds to a single transition. Vm was normalized by subtracting the mean from -5 to 0 s. White lines on the right indicated divisions between single neurons. The rows were sorted by each neuron's average Vm change during transitions to Theta. Right panel shows the same for CA1 pyramidal neurons. **(A4)** Top left panel shows the average Vm in blue (black shaded region marks mean ± SEM) triggered on transitions to Theta for a single neuron, as marked by the blue square in A3. Grey Vm traces come from two example transitions. Top right panel shows the average Vm from the same neuron, but zoomed in to better illustrate the lack of change occurring during Theta transitions. Two other example neurons are shown below. **(A5)** Left panel shows scatter plot of mean Vm before (Pre-Theta) compared to after (Post-Theta) transitions to Theta. Each point is the average from a single neuron. Dentate granule cells are colored blue, with filled circles marking neurons with significant changes in Vm (none). CA1 pyramidal neuron averages are marked in red. Similarly, the right panel shows the mean standard deviation of the Vm (high-pass filtered above 5 Hz) before and after transitions to Theta. **(B)** Pie charts showing the percent of time spent in each state across all recordings (left panel), preceding LIA (middle left panel), preceding SIA (middle right panel), and preceding Theta (right panel). **(C)** Scatter plot showing correlation between change in Vm during transitions to LIA (x-axis) compared to changes in Vm during transitions to SIA (y-axis). Each dot is the average change in Vm from a single neuron, colored according to neuron type as in (A5).

Figure 20: Membrane potential mean, variability, and distance to threshold are state-dependent **(A1)** Scatter plot showing the average Vm during LIA compared to SIA. Each point is the average from a single neuron. Dentate granule cells are colored in blue, with filled circles marking neurons with significant changes in Vm. CA1 pyramidal neuron averages are marked in red. **(A2)** Same as in A1, but comparing LIA and Theta. **(A3)** Same as in A1, but comparing SIA and Theta. **(A4)** Circles mark each state's Vm (median across neurons) after subtracting the mean Vm across states (the dotted line marking zero; absolute value reported on right) for dentate granule cells (blue) and CA1 pyramidal neurons (red). The whiskers mark the 25th and 75th percentiles. Bars above indicate significant differences ($p<0.05$) using a Mann-Whitney U test. **(B)** Same as in (A), but for Vm variability. **(C)** Same as in (A), but for distance to spike threshold. The distance to spike threshold was computed as the average spike threshold across LIA, SIA, and Theta epochs minus the membrane potential from each state.

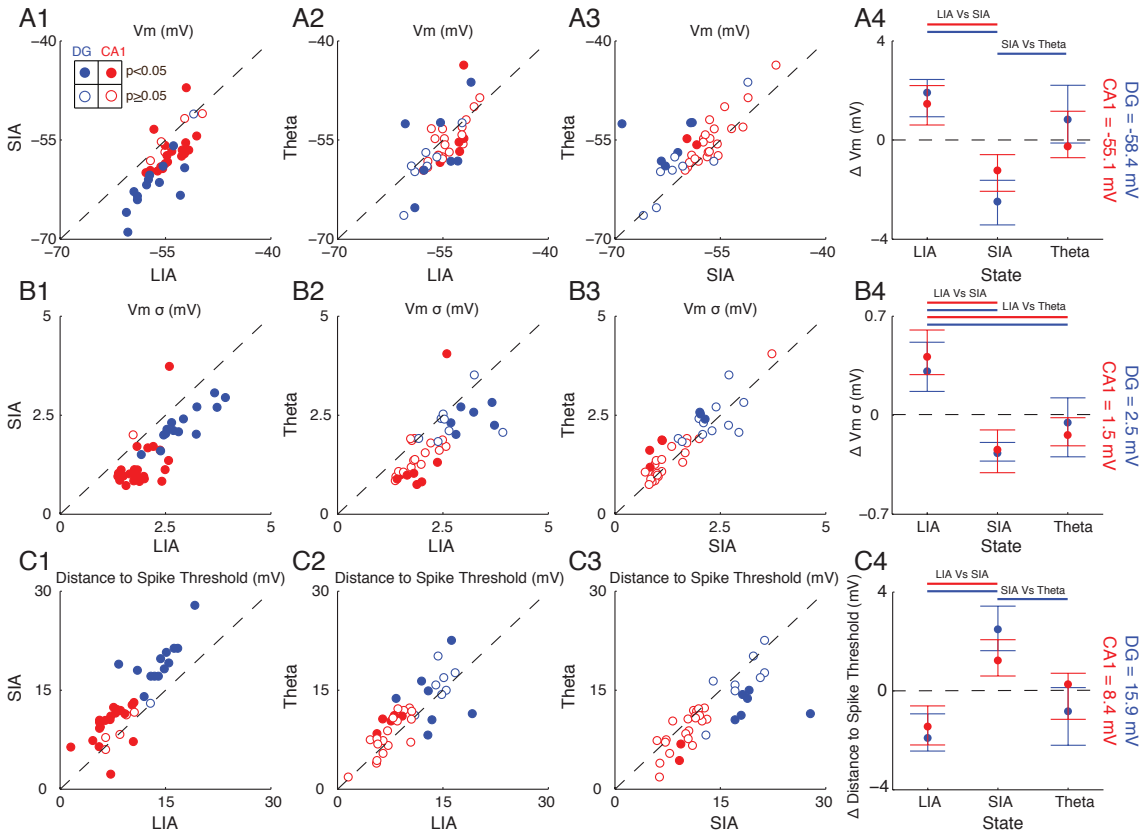

Theta may still be quite different from those of LIA and SIA. To assess this, we compared these quantities for the subset of dentate granule cells (n=14/20) and CA1 pyramidal cells (n=25/31) that we recorded during all three states (LIA, SIA, and Theta). As shown in Figure 20 A, most neurons were more depolarized during LIA and Theta compared to SIA, and tended to be more depolarized during LIA than Theta. Similarly, Vm variability was significantly larger during LIA compared to Theta and SIA, and tended to be higher during Theta than SIA (Figure 20 B).

These results demonstrate that Vm and its variability are highly brain-state-dependent. Such modulations in resting membrane potential and the amplitude of subthreshold fluctuations may affect the amount of depolarization needed to bring neurons to spike threshold. To measure this, we subtracted each neuron's average spike threshold from its state-specific average membrane potential. As shown in Figure 20 C, most hippocampal principal cells were significantly closer to spike threshold during LIA compared to SIA and tended to be closer during Theta than SIA. In addition, the spike threshold of dentate granule cells (-42.3 $\pm$ 0.6 mV) was significantly more positive than CA1 pyramidal neurons (-46.3 $\pm$ 0.6 mV; $p<0.002$, Mann-Whitney U test). Due to their higher spike threshold and hyperpolarized resting membrane potential, dentate granule cells were two times farther from spike threshold compared to CA1 pyramidal neurons during LIA, SIA, and Theta, which likely explains the sparse activity of granule cells in vivo. Together, these results provide evidence that coordinated modulations of membrane potential statistics may contribute to state-dependent network activity by controlling the amount of depolarization needed to bring neurons to spike threshold.

Origins of Pre-Ripple Ramps in the Membrane Potential of Hippocampal Neurons

Figure 21: Transitions to LIA contribute to pre-ripple ramps in the membrane potential
(Continued on following page)

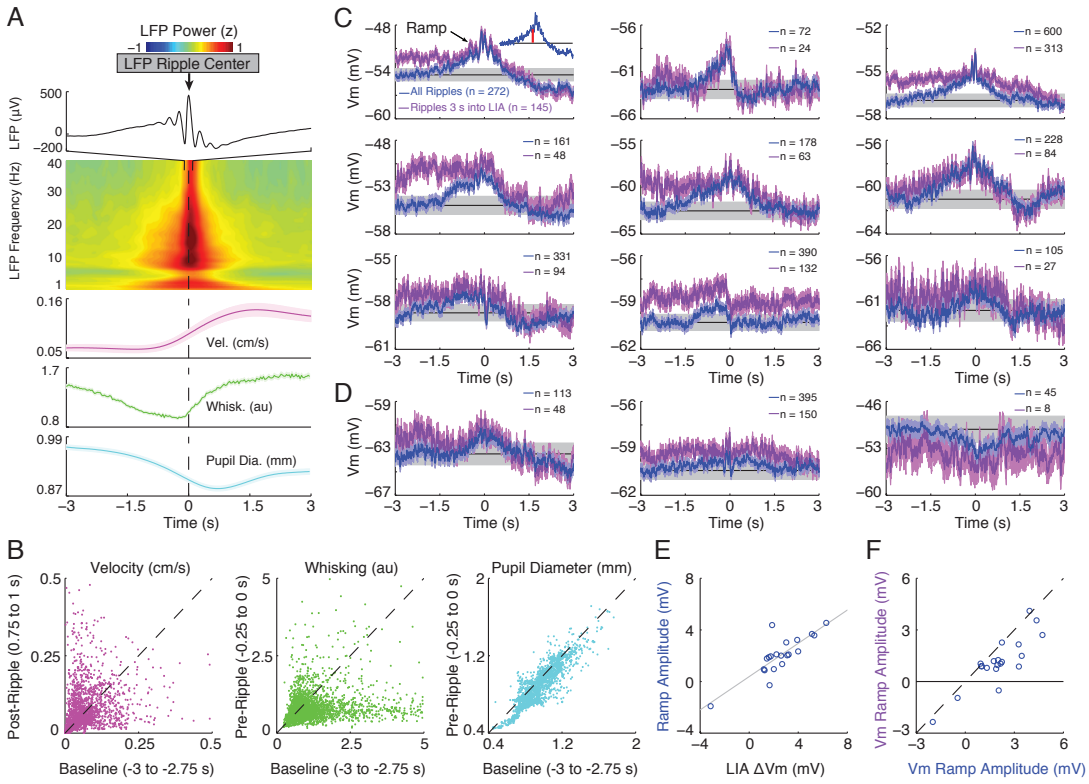

Figure 21: **(A)** The top panel displays the average ripple-triggered LFP from -100 to 100 ms showing the average ripple in the CA1 cell layer. The middle panel shows the average LFP power (z-score by frequency) from -3 to 3 s triggered on ripples, which occur at time 0. The bottom panels show the average velocity, whisking, and pupil diameter around ripple onset (shaded regions mark mean ± SEM). **(B)** Scatter plots of median velocity before (Baseline) compared after ripples (Post-Ripple), and whisking and pupil diameter well before (Baseline) compared to just before (Pre-Ripple) ripples. Each point comes from a single ripple and the axes labels list the time windows used for computing median values. Ripples were preceded by a significant decline in whisking activity (n=3705 ripples) and pupil diameter (n=1835 ripples; $p<0.001$, Wilcoxon signed-rank tests). **(C)** Ripple-triggered averages of the subthreshold Vm for individual dentate granule cells that show significant pre-ripple ramps (blue). The average Vm using only ripples occurring 3 seconds into an LIA epoch are shown in purple. Blue and purple shaded regions mark the 95% confidence intervals for each sample. The grey band marks the mean confidence intervals of the pre-ripple Vm (from -3 to -2 s) using all ripples (from the blue trace). The average Vm from this same interval is marked by the black line. The number of ripples entering each average is reported in the legends. The inset illustrates how ramp amplitude (red bar) was computed. **(D)** Same as in (C), but for three neurons showing smaller ramps that were not statistically significant. **(E)** Scatter plot of the amount each granule cell depolarizes during transitions to LIA versus the amplitude of its ramp. **(F)** Scatter plot showing the amplitude of the ramps using all ripples (x-axis) compared to using only ripples occurring greater than 3 seconds into an LIA epoch (y-axis).

In a previous study, we found that a subset of CA1 pyramidal neurons (n=5/30) show depolarizing and hyperpolarizing ramps in their Vm starting approximately one second before ripple onset (Hulse et al., 2016). Can changes in membrane potential associated with transitions to LIA contribute to these ramps? To assess this, we first triggered the LFP and behavioral variables on ripples detected in the CA1 pyramidal cell layer (Figure 21 A). Consistent with SWRs preferentially occurring during the LIA state (Figure 22 A), delta and beta power in the hippocampal LFP were high around ripples, while whisking activity and pupil diameter showed a significant decline preceding SWRs (Figure 21 A-B). Furthermore, 48% of SWRs occurred within 3 sec following transitions to LIA (Figure 22 B). These findings demonstrate that transitions to LIA are indeed a factor contributing to pre-ripple ramps in the Vm. They also make two specific predictions. First, similar ramps should be present in DG granule cells, since these cells also depolarize across transitions

Figure 22: Behavioral measures decrease leading up to ripples occurring at least 3 seconds into a period of LIA **(A)** Pie chart showing the distribution of ripples occurring in each state. **(B)** For ripples occurring within an epoch of LIA (82% overall), the distribution of times between the start of LIA and ripple occurrence is plotted. **(C)** Top panels shows the average ripple-triggered LFP from -100 to 100 ms. Middle panel shows the average LFP power (z-score by frequency) from -3 to 3 s triggered on ripples, which occur at time 0. Bottom panels show that average velocity, whisking, and pupil diameter (shaded regions mark mean ± SEM). Only ripples occurring at least 3 seconds into a period of LIA were considered. **(D)** Scatter plots of median velocity before (Baseline) compared after ripples (Post-Ripple), and whisking and pupil diameter well before (Baseline) compared to just before (Pre-Ripple). Each point comes from a single ripple. Only ripples occurring at least 3 seconds into a period of LIA were considered. Whisking (n=1499 ripples) and pupil diameter (n=659) showed a significant declines preceding ripples within sustained periods of LIA ($p<0.001$, Wilcoxon signed-rank tests). **(E)** Scatter plot showing the correlation between the amount each CA1 pyramidal neuron depolarizes during transitions to LIA (x-axis) compared to the amplitude of its ramp (y-axis).

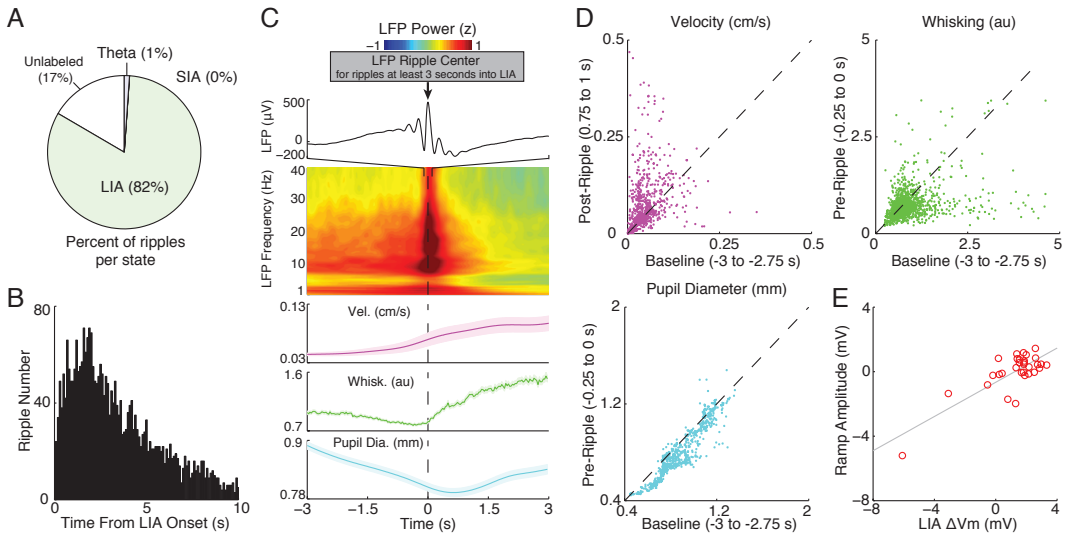

to LIA. Indeed, half of dentate granule cells showed significant depolarizing ramps in their pre-ripple Vm, and while not statistically significant, many others showed smaller ramps (Figure 21 C-D). Second, the magnitude of the ramps should correlate with the change in membrane potential associated with LIA transitions. Indeed, neurons that depolarized more across transitions to LIA had larger depolarizing ramps, both in the dentate gyrus (Figure 21 E; R^2=0.7, p<0.001) and area CA1 (Figure 22 E; R^2= 0.66, p<0.001).

Are transitions to LIA the sole driver of pre-ripple ramps? To answer this question, we restricted our analysis to ripples occurring at least 3 seconds into a period of LIA (Figure 22). Interestingly, both whisking and pupil diameter still showed significant declines preceding ripples (Figure 22 D), suggesting that behavioral activity decreases leading up to ripples even within the LIA state. In addition, though smaller, Vm ramps were still observed for ripples occurring at least 3 seconds into a period of LIA (Figure 21 F). These findings suggest that a reduction in behavioral activity preceding ripples within LIA epochs also contributes to pre-ripple Vm ramps. Importantly, they also suggest that behavioral state changes within LIA may affect network activity.

While previous studies have largely considered LIA to be a homogenous state, the above results suggest that fluctuations in behavior within LIA may affect network activity. To investigate this directly, we divided LIA epochs into periods where the pupil was constricting (72.2% of time) or dilating (27.8% of time) and compared ripple rate, the amplitude of LFP fluctuations, mean Vm, and the amplitude of Vm fluctuations (Figure 23). Figure 23 A shows a clear example where a brief microdilation during an LIA epoch is associated with a desynchronization of the LFP and a hyperpolarization and reduction in Vm variability. Consistent with this example, periods of pupil dilation during LIA had significantly lower

Figure 23: Fluctuations in pupil diameter during LIA are reflected in membrane potential fluctuations of individual neurons **(A)** Example of correlated changes in pupil diameter, LFPs, and subthreshold activity during a period of LIA. The top panel shows pupil diameter, with grey box marking the period of dilation. The middle panel shows four LFPs around the CA1 cell layer (marked by red dot). Blue ticks mark time of ripple occurrence. The bottom panel shows subthreshold activity from a dentate granule cell. Notice that pupil dilation is associated with a flattening of the LFP and a hyperpolarized Vm with low variability. **(B)** Same as in (A), but for a period of LIA with two dilation periods and subthreshold activity from a CA1 pyramidal cell. **(C)** Histogram showing the difference in ripples rates for constriction compared to dilation across LIA epochs. Positive values indicate a higher ripple rate during constriction relative to dilation. Epochs of LIA with no ripples were excluded. Periods of pupil dilation had significantly lower ripple rates (n=855 LIA epochs; $p<0.001$). **(D)** Scatter plot showing the standard deviation of the LFP from stratum radiatum of CA1 (bottom LFP channel in A/B), where sharp waves occur, during periods of constriction compared to periods of dilation. Each dot represents one LIA epoch. Periods of pupil dilation had significantly smaller LFP fluctuations (n=855 LIA epochs; $p<0.007$). **(E)** Scatter plot showing the average Vm in LIA during periods of constriction compared to periods of dilation. Each dot represents one LIA epoch and dots are color coded by cell type (blue for DG, red for CA1). Periods of pupil dilation were associated with significantly more hyperpolarized Vm (DG: n=10 granule cells from n=539 LIA epochs, $p<0.007$; CA1: n=9 CA1 pyramidal neuron from n=319 LIA epochs, $p<0.001$). **(F)** Same as in (E), but for the standard deviation of the Vm. Periods of pupil dilation had significantly smaller Vm fluctuations (DG: n=10 granule cells from n=539 LIA epochs, $p<0.001$; CA1: n=9 CA1 pyramidal cells from n=319 LIA epochs, $p<0.001$; p-values from Wilcoxon signed-rank tests).

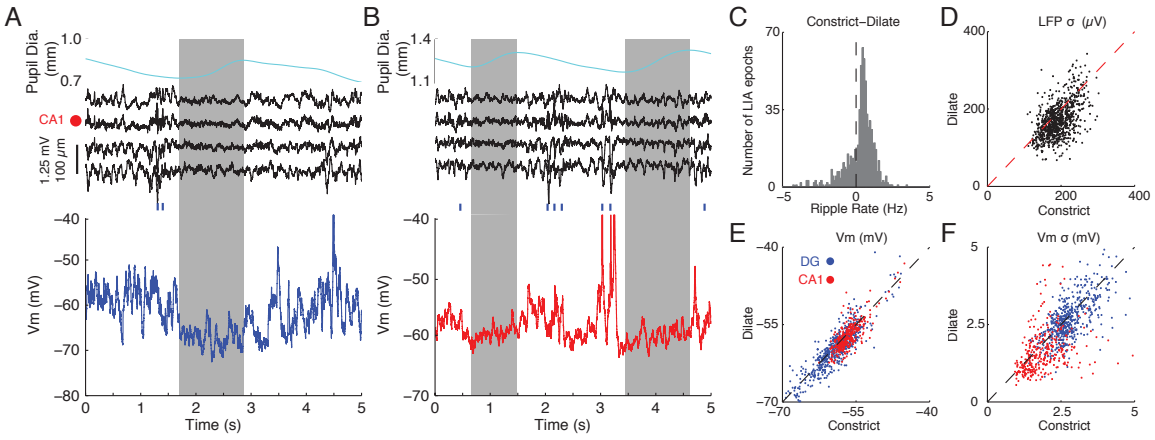

ripple rates, lower amplitude LFP fluctuations, a more hyperpolarized Vm, and smaller amplitude Vm fluctuations (Figure 23 C-F). These results demonstrate that LIA is not a homogenous state. Instead, constant fluctuations in the level of arousal drive changes in subthreshold dynamics and network activity.

3.4 Discussion

By combining in vivo whole-cell recordings from identified dentate granule cells and CA1 pyramidal neurons with multisite LFP and behavioral measurements in awake mice, we characterized how hippocampal subthreshold activity is modulated by brain and behavioral state. We show that the membrane potential of most hippocampal neurons is depolarized and has large amplitude fluctuations during LIA. In contrast, SIA is associated with a hyperpolarized membrane potential and smaller subthreshold fluctuations. During Theta oscillations, the Vm has intermediate levels of depolarization and subthreshold fluctuations. In agreement with these changes, the distance to spike threshold is brain-state-dependent. In addition, many hippocampal cells begin to depolarize approximately one second before ripple onset. These Vm ramps correlate with brain state transitions to LIA as well as smaller fluctuations in behavioral state within sustained periods of LIA. Finally, our results provide evidence that rapid fluctuations in pupil diameter during periods of LIA mirror modulations in ripple rate and subthreshold activity.

The statistics of the membrane potential reflect a combination of synaptic input patterns and single-cell properties. There is a wealth of evidence from extracellular recordings that spiking patterns, both within the hippocampus and its input areas, strongly depend on brain state (O'Keefe, 1976, O'Keefe and Nadel, 1978, Buzsaki et al., 1983, Wilson and

McNaughton, 1994, Chrobak and Buzsaki, 1996, Jarosiewicz et al., 2002, Lee and Wilson, 2002, Hafting et al., 2005, Foster and Wilson, 2006, Kay et al., 2016, Olafsdottir et al., 2016). Furthermore, previous studies have suggested that single-cell properties, such as membrane conductances or synaptic efficacy, may also be modulated by brain state (Winson and Abzug, 1977, Winson and Abzug, 1978). However, these properties have been much harder to study in vivo. Our results provide evidence that, in addition to input patterns, single-cell properties are indeed modulated by brain state, altering the characteristics of hippocampal neurons.

In particular, the gradual membrane potential depolarization starting approximately one second before ripple onset in both dentate granule cells and CA1 pyramidal neurons is difficult to account for based on the known firing properties of hippocampal neurons around ripples (O'Keefe and Nadel, 1978, Buzsaki, 1986, Buzsaki et al., 1992, Wilson and McNaughton, 1994). The predominant view is that the major source of excitatory drive during ripples is the firing of CA3 pyramidal cells (Buzsaki, 2015). While the spiking properties of these neurons have been extensively studied (Csicsvari et al., 2000), there is no evidence that activity in CA3 ramps up as early as one second before ripples. In fact, there is no evidence indicating that the spiking output of any principal neuron within the hippocampus or entorhinal cortex can be the source of synaptic input accounting for the pre-ripple ramps in the membrane potential.

Instead, the observed Vm ramps most likely reflect shifts in the properties of single hippocampal neurons, presumably mediated by state dependent changes in the neuromodulatory environment (Kalen et al., 1989, Kametani and Kawamura, 1990, Park et al., 1999, Lee and Dan, 2012). There are two observations in our data that support this interpreta-

tion. First, the amplitude of each neuron's Vm ramp is highly correlated with its change in average membrane potential across transitions to LIA. Hence, these transitions, which are known to be associated with a shift in the neuromodulatory environment (Marrosu et al., 1995), are a significant factor contributing to Vm ramps. Second, pupil diameter, which reflects fluctuations in brain state and arousal (Reimer et al., 2014, McGinley et al., 2015b), decreases starting approximately one second before ripple onset, mirroring the Vm ramps. This suggests that fluctuations in the neuromodulatory environment within LIA may be a second significant factor contributing to Vm ramps. Consistent with this interpretation, a recent study identified a subset of Median Raphe neurons that ramp down their firing a second or so before ripple onset, representing one potential source of this neuromodulatory influence (Wang et al., 2015).

Since neuromodulators are expected to act globally on the circuit, the resulting coordinated depolarization of most hippocampal neurons may reflect the network entering a regime conducive to ripple generation and transmission. Specifically, the population burst nucleated within CA3 should be able to effectively drive the CA1 network, largely in the absence of entorhinal input. One mechanism that has been suggested to enable this is an increase in the efficacy of the Schaffer collaterals during LIA (Winson and Abzug, 1977, Winson and Abzug, 1978, Hasselmo, 1999, Hasselmo and McGaughy, 2004). The large subthreshold fluctuations we observe during LIA may reflect this increase in synaptic efficacy. Our results also show that the membrane depolarization associated with LIA brings neurons closer to spike threshold, which represents an additional mechanism that may enable the effective transmission of ripples. We speculate that a depolarized and highly variable membrane potential may support the nucleation of ripples in CA3 by affecting the probability

that a subset of neurons is coactive. Shifts towards this regime occur not only during transitions to LIA, but, importantly, during smaller fluctuations in brain state ("microstates") within sustained periods of LIA. Seen in this light, pre-ripple ramps in the membrane potential reflect the network entering a state capable of generating ripples, while the intracellular depolarization and ripple oscillations observed during SWRs reflect mechanisms specific to the generation process (Ylinen et al., 1995, Hulse et al., 2016).

By combining in vivo whole-cell recordings with multisite LFP and behavioral measurements, we show that the subthreshold dynamics of hippocampal neurons are strongly modulated by brain state. These fundamental measurements reveal several novel features of hippocampal processing. First, the distance to spike threshold is state-dependent. This will affect the recruitment of neurons to network patterns by determining the amount of depolarization needed to reach spike threshold. Second, many hippocampal neurons show depolarizing ramps in their membrane potential starting approximately one second before ripple onset. These ramps reflect coordinated shifts in subthreshold activity towards a state conducive for ripple generation. Finally, even within well-characterized brain states, such as LIA, rapid fluctuations in pupil diameter mirror modulations in the membrane potential of hippocampal neurons. This suggests that fast modulations of arousal are reflected in coordinated shifts in hippocampal subthreshold activity. These results support a dynamic view of waking brain states, whereby coordinated fluctuations of single-cell properties contribute to the emergence of network patterns in the hippocampus. Furthermore, they provide a basis for future work dissecting the cellular and modulatory mechanisms supporting brain state-dependent processing in the hippocampus.

3.5 Experimental Procedures

Head fixation surgery

Male mice (n=23; C57BL/6-E; Strain Code 475; Charles River Laboratories) were surgically implanted with a light-weight, stainless steel ring embedded in dental cement, which allowed for mechanically stable head-fixation in the recording apparatus. A stainless steel reference wire was implanted over the cerebellum for LFP silicon probe recordings. The skull was leveled and the locations of the pipette and probe exposures were marked on the skull over the left hemisphere. For whole-cell recordings in CA1, the probe exposure was located -1.7 mm posterior and 2.0 mm lateral from Bregma and the patch exposure was -1.9 mm posterior and 1.5 mm lateral. For whole-cell recordings in the dentate gyrus, the probe exposure was located -1.7 mm posterior and 1.75 mm lateral from Begma, and the patch exposure was located -1.7 mm posterior and 0.65 mm lateral. Following surgery, mice were returned to their home cage, maintained on a 12 hour light/dark cycle, and given access to food and water ad libitum. Ibuprofen (0.2 mg/mL) was added to the water as a long-term analgesic. Mice were given at least 48 hours to recover before the day of the experiment.

Exposure surgery

On the day of the experiment, mice (age P28 to P37) first underwent a short surgery to expose the brain. While anesthetized with 1% isoflurane and head-fixed in the stereotaxic apparatus, two small exposures were drilled (pipette: 500 μm diameter; probe: 200 μm diameter) over the left hippocampus at the previously marked locations. A recording chamber was secured on top of the head-fixation device and filled with pre-oxygenated (95% O2, 5% CO2), filtered (0.22 μm) artificial cerebrospinal fluid (aCSF) containing (in mM): 125 NaCl, 26.2 NaHCO3, 10 Dextrose, 2.5 KCl, 2.5 CaCl2, 1.3 MgSO4, 1.0 NaH2PO4.

Awake, in vivo recordings

Mice were head-fixed on top of a spherical treadmill secured on an air table (TMC). The treadmill could rotate along a single axis, allowing the mice to run and walk freely. A potentiometer connected to the axis of the treadmill allowed for behavioral readout of locomotor velocity. To measure pupil diameter and whisker movements, the mouse was illuminated with an infrared (850 nm) LED (M85OL3, Thorlabs) and imaged with a CCD camera (scA640-70fm, Basler; with a Nikon AF Micro-Nikkor 105mm f/2.8 lens) positioned 60 degrees from the midline (mouse's left) and 30 degrees down from the horizontal plane (Sakatani and Isa, 2004). On either side of the treadmill, two platforms supporting micromanipulators (Sutter Instrument Company) allowed for precise positioning of a silicon probe (mouse's left) and glass pipettes (mouse's right). A single-shank, 32-site silicon probe (NeuroNexus) with 100 μm site spacing was inserted in the coronal plane ($\sim$15 degree angle pointing towards the midline) to a depth of 2600-3000 μm. Sites spanned all of neocortex, area CA1, the dentate gyrus, and parts of the thalamus. The probe was adjusted so that a recording site was positioned within the CA1 pyramidal cell layer for reliably recording LFP ripple oscillations. The probes were grounded to the recording table and referenced to a wire implanted over the cerebellum

To find the depth of the CA1 and dentate cell layers, we used artificial cerebrospinal spinal fluid (aCSF) filled pipettes to perform juxtacellular (Pinault, 1996) recordings from putative CA1 pyramidal and dentate granule cells. The location of the CA1 layer was signaled by the occurrence of large amplitude ripples that appeared synchronously on the pipette and probe site in the CA1 cell layer. The location of the dentate cell layer could be estimated by the appearance of dentate spikes and large amplitude gamma oscillations.

Long-taper pipettes (for juxtacellular and whole-cell recordings) were pulled from borosilicate capillaries (OD: 1.0 mm, ID: 0.58 mm; Sutter Instrument Company) using a Model P-2000 puller (Sutter Instrument Company) to an inner tip diameter of ∼0.8-1.5 μm and outer diameter of ∼2 μm (5-8 MΩ), and inserted into the brain in the coronal plane with a ∼15 degree angle pointing away from the midline. For whole-cell recordings from CA1 pyramidal neurons, the probe and patch pipette were separated by approximately 200 μm in the anterior-posterior direction and 100 μm in the medial-lateral. For whole-cell recordings from dentate granule cells, the probe and patch pipette were separated by approximately 200 μm in the medial-lateral direction. Recordings (juxtacellular and whole-cell) were made with a MultiClamp 700B amplifier (Molecular Devices). For juxtacellular recordings, the capacitance neutralization circuit was off and the output was AC coupled and amplified 100x.

Whole-cell recordings were performed after the depth of the cell layer had been identified. Pipettes were filled with an internal solution containing (in mM): 115 K-Gluconate, 10 KCl, 10 NaCl, 10 Hepes, 0.1 EGTA, 10 Tris-phosphocreatine, 5 KOH, 13.4 Biocytin, 5 Mg-ATP, 0.3 Tris-GTP. The internal solution had an osmolarity of 300 mOsm and a pH of 7.27 at room temperature. The membrane potential was not corrected for the liquid junction potential. Whole-cell recordings were obtained "blind" according to previously described methods (Margrie et al., 2002) in current clamp mode (Schramm et al., 2014). Capacitance neutralization was set prior to establishing the GΩ seal. After obtaining the whole-cell configuration, the neuron's membrane potential was recorded in current clamp mode. Access resistance was estimated online by fitting the voltage response to hyperpolarizing current steps. Recordings were aborted when the access resistance exceeded 120 MΩ or the action

potential peak dropped below 0 mV. One to five whole-cell recordings (n=31 CA1 pyramidal cells; n=20 dentate granule cells) were performed per mouse. All animal procedures were performed in accordance with National Institute of Health guidelines and with approval of the Caltech Institutional Animal Care and Use Committee.

Signal acquisition

All electrophysiological signals and video acquisition was performed with custom Labview software (National Instruments) that we developed. Electrophysiological signals were sampled simultaneously at 25 kHz with 24 bit resolution using AC (PXI-4498, internal gain: 30 dB, range: +/- 316 mV) or DC-coupled (PXIe-4492, internal gain: 0 dB, range: +/- 10 V) analog-to-digital data acquisition cards (National instruments) with built-in anti-aliasing filters for extracellular and intracellular/juxtacellular/velocity recordings, respectively. Video (640x480 pixels; 45.7 pixels/mm) was acquired at 30 Hz and timestamped to electrophysiological signals.

Histology and imaging

Following the experiment, mice were deeply anesthetized with 5% isoflurane, decapitated, and the brain extracted to 4% PFA. Staining of biocyin-filled cells for morphological identification was performed according to previously described methods (Horikawa and Armstrong, 1988). Brains were fixed at 4 C in 4% paraformaldehyde overnight and transferred to 0.01 M (300 mOsm) phosphate buffered saline (PBS) the next day. Up to one week later, brains were sectioned coronally (100 μm) on a vibrating microtome (Leica), permeabilized with 1% Triton X-100 (v/v) in PBS for 1-2 h, and incubated overnight at room temperature in PBS containing avidin-fluorescein (1:200, Vector Laboratories), 5% (v/v) normal horse serum (NHS), and 0.1% Triton X-100. Sections were rinsed in PBS between

each step. The next day, sections containing biocytin stained neurons were identified on an inverted epifluorescent microscope (Olympius IX51) for further immunohistochemical processing.

To aid in classifying recorded neurons as CA1 pyramidal or dentate granule cells, we performed immunohistochemical staining against calbindin (CB) and parvalbumin (PV). Sections containing biocytin-stained neurons were first incubated in blocking solution containing 5% NHS, 0.25% Triton X-100, and 0.02% (wt/v) sodium azide in PBS. Next, slices were incubated in PBS containing primary antibodies against CB (Rabbit anti-Calbindin D-28k, 1:2000, Swant) and PV (Goat anti-parvalbumin, 1:2000, Swant) overnight. After thorough rinsing in PBS, slices were incubated in PBS containing secondary anitbodies CF543 donkey anti-rabbit (1:500, Biotium) and CF633 donkey anti-goat (1:500, Biotium). Processed slices were rinsed and mounted in antifading mounting medium (EverBrite, Biotium).

Stained slices were imaged on an inverted confocal laser-scanning microscope (LSM 710, Zeiss). Biocytin-stained neurons were unambiguously classified as CA1 pyramidal neurons if their soma was located in the CA1 pyramidal cell layer, showed a morphology characteristic of these neurons (bifurcating apical dendrites, dendritic spines, etc.), had PV-negative soma, and showed electrophysiological properties consistent with CA1 pyramidal neurons. Similarly, granule cells had PV-negative soma located in the dentate granule cell layer and a cone-shaped dendritic tree extending into the molecular layer.

Measuring and setting access resistance

Access resistance was estimated online using custom-written software in Labview that communicated with the software (Commander, Molecular Devices) controlling the Multi-

Clamp 700B amplifier through an application programming interface (API). To estimate the access resistance, the bridge balance was temporarily turned off. Then, two -100 pA current pulses (250 ms duration, 250 ms inter-pulse interval) were delivered, the first 50 ms of the hyperpolarizing voltage responses was fit using a simple model, and if the R^2 fit exceeds 0.99, the bridge balance was set to its new value, otherwise it was returned to the previous value. This procedure was performed once every minute during whole-cell recordings. In addition, all recording parameters in the Commander software were acquired once every second using the API, time stamped to electrophysiological signals, and saved for offline review. The pipette's voltage response to hyperpolarizing current steps was fit online using a simple double exponential model (Anderson et al., 2000). The computational simplicity of this model sped online fitting. For offline estimates, we used a biophysically-inspired, single-compartment model (de Sa and MacKay, 2001). The results obtained from the two models were nearly identical under our recording conditions.

Behavioral Variable Analysis

To measure locomotor velocity, a potentiometer was connected to the axis of the treadmill and configured so its output voltage went from 0 to 5 V over the course of a single revolution. Samples where the voltage rolled over from 5 to 0 V (and 5 to 0 V) were excluded. The voltage trace was then converted from volts to distance (cm) using the circumference of the ball (63.8 cm per 5 V). The position data was downsampled from 25 kHz to 1 kHz and differentiated to obtain the velocity (in cm/s). Finally, the velocity signal was smoothed with a Gaussian (σ=0.5 s).

To measure whisking, a region of interest encompassing the mouse's whiskers was selected and the mean absolute difference in pixel intensity across frames was computed and

normalized by diving by its median. The resulting trace was smoothed with a Gaussian (σ=0.05 s). Whisking is reported in arbitrary units (AU) and reflects both movements of the whiskers and the snout.

Pupil diameter data came from a subset of recordings (n=10/20 granule cells; n=9/31 CA1 pyramidal neurons) with high-quality pupil imaging. To measure pupil diameter, a region of interest encompassing the mouse's left eye was taken. The specular reflection of the IR light source on the eye was masked and the image contrast was adjusted to emphasize the difference in pixel intensity between the pupil and the rest of the eye. Next, the image was inverted and smoothed with a 2-D Gaussian (σ = 5 pixels, 0.109 mm). Candidate circles fitting the pupil were detected using the Circular Hough Transform with two diameter ranges (20-40 pixels, 0.437-0.875 mm; and 21-60 pixels, 0.919-2.626 mm), and the circle with the largest peak in the accumulator matrix was taken as the pupil fit. The resulting pupil diameter trace was smoothed with a Gaussian (σ=0.25 s).

Intracellular spike detection, spike threshold measurement, and subthreshold Vm calculation

Spikes from whole-cell recordings were detected as peaks greater than 10 mV after high-pass filtering the Vm (Parks-McClellan optimal equiripple FIR filter, 20-50 Hz transition band, 40 dB minimum attenuation in the stop bands). Spike threshold was calculated for each spike similar to previously describes methods (Epsztein et al., 2011). In short, spike threshold was defined as the voltage where dV/dt exceeded 5 V/s or 0.33 of the spike's maximum dV/dt, whichever was smaller. Only spikes occurring greater than 100 ms after the previous spike were considered, since spike threshold increases within bursts. To compute each neuron's average spike threshold, we used all spikes occurring in LIA, SIA, or Theta. Each neuron's average spike threshold was used to compute its distance to spike

threshold by subtracting its state-dependent average Vm (Figure 20).

The subthreshold membrane potential was computed by linearly interpolating periods with action potentials from 3 ms before to 5 ms after the spike peak. For spikes occurring within 20 ms of each other, as during complex bursts, the first spike was linearly interpolated from 3 ms before its peak until the sample showing the minimum value before the next spike. This procedure provided a lower bound on complex spike waveforms, effectively revealing the slow, depolarizing component underlying them while excluding fast action potential waveforms (Epsztein et al., 2011). Following linear interpolation, the signals were low-pass filtered (Parks-McClellan optimal equiripple FIR filter, 250-350 Hz transition band, 40 dB minimum attenuation in the stop bands).

Ripple detection

LFP ripple oscillations were detected as transient increases in ripple-band power from the probe site located in the CA1 pyramidal cell layer. To compute ripple band power, LFPs were filtered between 80-180 Hz (Parks-McClellan optimal equiripple FIR filter, 80-180 Hz pass band, 50-80 and 180-200 Hz transition bands, 60 dB minimum attenuation in the stop bands), the ripple-band envelope was computed as the instantaneous amplitude from the Hilbert transform, and the envelope was low-pass filtered (Parks-McClellan optimal equiripple FIR filter, 20-30 Hz transition band, 40 dB minimum attenuation in the stop bands). From this signal, an upper threshold was set as 4.5-5.5 times the median. A lower threshold was set as half the upper threshold. Ripples were detected as peaks in the ripple band envelope above the upper threshold, and with time between positive-going and negative-going lower threshold crossings longer than 30 ms. Ripples meeting these criteria, but with peaks less than 60 ms apart, were merged. The time of ripple occurrence was

defined as the sample with the largest amplitude (positive peak) in the ripple band within the detected ripple and used as time 0.

Brain State Identification

All offline analysis was performed with Matlab (MathWorks). Brain state identification was carried out in four stages. First, the hippocampal LFPs were subdivided in contiguous 500 ms segments and represented as points in a six-dimensional feature space based on their spectral content. Second, a subset of the points were labeled as Theta or LIA using a semi-automated approach described below. Third, these labeled examples were used to initialize a K-means classifier that categorized all segments as LIA, Theta, or Unlabeled. Fourth, Unlabeled segments with low broadband power were categorized as SIA. A more detailed description of these steps is given below.

LFPs were extracted from 5 sites in the hippocampal formation, positioned between 200 μm above (in stratum oriens) to 600 μm below the CA1 pyramidal cell layer (in 200 μm increments). LFPs were low-pass filtered and downsampled from 25 kHz by a factor of 96 (to $\sim$260 Hz). A time-frequency decomposition was performed using complex Morlet wavelets with central frequencies from 0.3 to 80 Hz in 0.1 Hz steps and a bandwidth parameter of 10. Power at each sample and frequency was computed as the modulus of the complex wavelet coefficient. To obtain a single time-frequency representation for state identification, power values across the 5 sites were averaged. Next, a six dimensional feature space was created by calculating the average z-scored LFP power in contiguous 500 ms segments. The features used were: theta (6-9 Hz), delta (0.5-3.5 Hz), theta/delta, beta (10-20 Hz), gamma (30-50 Hz), and Total Power (average power between 0.3-80 Hz; before averaging, each frequency bin was z-scored across time).

A subset of the points in the feature space were labeled using the following procedure. Periods of Theta were detected as epochs with theta/delta >2.25 times the median. Theta periods less than 3 seconds apart were first joined, and then periods less than 5 seconds were excluded. Transitions out of LIA were detected by finding instances where the average Total Power in a 3 second window declined by 0.7 in the subsequent 2 seconds. Segments overlapping detected Theta periods were labeled as Theta. Segments occurring from 0 to 4 seconds before transitions out of LIA were labeled as LIA. Segments occurring 0 to 1 second following transitions out of LIA were marked Unlabeled.

The average feature vector for these 3 states was used to initialize a K-means classifier on all feature vectors. After clustering, Unlabeled segments with Total Power less than -1.25 were defined as SIA. Theta segments were merged/excluded as described above. LIA segments <500 ms apart were first merged, and then segments shorter than 2 seconds were excluded. SIA segments less than 1 second were excluded. For Figure 17-18, the LFP, behavioral variables, and Vm were triggered on transitions to LIA and SIA. Because these transitions could be fast, but our staging was done in 500 ms increments, we adjusted the start times for transitions to LIA and SIA by finding the sample where Total Power in the LFP showed the largest increase (for LIA) or decrease (for SIA) within 500 ms of the original start times.

Quantification and statistical analysis of behavioral variables and subthreshold activity

To quantify the change in behavioral variables and subthreshold activity upon transitions into LIA, SIA, and Theta (Figures 17, 18, and 19), we compared the average values in pre- and post-transition time windows. Preliminary analysis showed that different variables had different dynamics around state transitions, so slightly different windows were selected

and fixed for further analysis. For transitions to LIA and SIA, we compared the median velocity, whisking activity (Pre: -2 to -1.5 s; Post: 0 to 0.5 s), pupil diameter (Pre: -1 to -0.5 s; Post: 1.5 to 2 s), Vm mean and variability (Pre: -2 to -1 s; Post: 0 to 1 s). For transitions to Theta, we compared the median velocity, whisking, pupil diameter (Pre: -2 to -1.5 s; Post: 3 to 4 s), Vm mean and variability (Pre: -2 to -1 s; Post: 4 to 5 s). Vm variability was computed as the standard deviation of the high-pass filtered subthreshold Vm (Parks-McClellan optimal equiripple FIR filter, 4.8-5 Hz transition band, 40 dB minimum attenuation in the stop bands) to exclude the contribution of average shifts in membrane potential that occur around the transitions. Similarly, to quantify changes in behavioral variables around ripples (Figure 21 and Figure 22), we compared their median activity in time windows that reflect each signal's dynamics around ripples. We compare the velocity well before ripples (-3 to -2.75 s) to afterward (0.75 to 1 s) to assess whether there was an increase in locomotor activity after ripples. Similarly, we compared whisking and pupil activity well before (-3 to -2.75 s) to just before (-0.25 s to 0 s) ripple onset to assess whether there was a decrease in activity leading up to ripples. Wilcoxon signed-rank tests were used to assess significant differences in the above values.

To quantify the difference in neuronal activity between states (Figure 20), we computed the average subthreshold Vm and Vm variability (standard deviation of the high-pass filtered subthreshold Vm) for every epoch of LIA (0 to 1 s after transitions LIA), SIA (0 to 1 s after transitions to SIA), and Theta (4 to 5 s after transitions to theta) for each recording. Only neurons with data from all three states were included in the analysis. Mann-Whitney U tests were used to assess differences between states for each individual neuron (indicated by fill of circles in Figure 20 A1-A3, B1-B3, C1-C3), and Wilcoxon signed-rank tests were

used to test for significant difference across all neuron averages (Figure 20 A4, B4, C4).

To assess the significance of pre-ripple ramping in the neuron-averaged, ripple-triggered Vm traces (Figure 21 C-D), 95% confidence intervals on the subthreshold Vm were constructed at each sample from -3 s to 3 s. Pre-ripple confidence intervals were computed as the average of the upper/lower 95% confidence intervals from -3 to -2 seconds. The mean Vm was considered significantly different ($p<0.05$) from baseline if it went above/below the upper/lower baseline confidence intervals. Neurons were considered to have significant ramps if their average Vm spent at least 150 ms continuously above or below the 95% baseline confidence intervals at least -100 ms before the ripple.

In order to evaluate the effect of pupil diameter on neuronal activity during LIA (Figure 23), we divided every LIA epoch from all neurons into periods where the pupil was constricting and periods where the pupil was dilating. LIA epochs that did not contain both periods of constriction and dilation were excluded (31% of LIA epochs). Next, we compared the average ripple rate, LFP amplitude (standard deviation of the LFP from the channel 200 μm below the CA1 pyramidal cell layer, where sharp waves occur), mean subthreshold Vm, and Vm variability for periods of pupil constriction and dilation. Wilcoxon signed-rank tests were used to assess the significance of differences in neuronal activity between pupil states.

4 Membrane Potential Dynamics of Granule Cells During Hippocampal Ripples and Dentate LFP Spikes in Awake Mice

4.1 Summary

The hippocampal formation generates two distinct population events during quiet wakefulness and slow wave sleep, known as sharp-wave/ripples and dentate LFP spikes. Previous studies have suggested that dentate spikes have a suppressive effect on the CA1-CA3 network and may function to delay the occurrence of sharp-wave/ripples, but whether and how these two population events interact remains poorly understood. Furthermore, dentate granule cells are known to receive excitatory input during sharp-wave/ripples, but the source of this excitation is not entirely known. To address these issues, we combined whole-cell recordings from identified dentate granule cells with simultaneous LFP measurements from a nearby multisite silicon probe in awake, head-fixed mice. Our results provide evidence for coordinated interactions between sharp-wave/ripples and dentate spikes and suggest that granule cells receive their main excitatory input from CA3 during SWRs. These findings inform models of sharp-wave/ripple generation and their interaction with dentate spikes.

4.2 Introduction

During periods of quiet wakefulness and slow wave sleep, the hippocampal formation generates spontaneous activity that is thought to support memory consolidation and retrieval, but the underlying mechanisms remain poorly understood (Buzsaki, 1989, Carr et al., 2011). Two main population events have been identified: sharp-wave/ripples (SWRs) and dentate LFP spikes (DSs) (O'Keefe and Nadel, 1978, Buzsaki, 1986, Bragin et al., 1995). SWRs are

associated with population bursts throughout the hippocampal formation and associated areas, but are likely nucleated in the recurrent CA3 network (Buzsaki, 2015). The CA3 burst provides excitatory input to CA1 pyramidal neurons, producing an intracellular depolarization and associated negative sharp wave in stratum radiatum (Ylinen et al., 1995, Hulse et al., 2016). This excitatory input also generates a population burst in area CA1. During the burst, dynamic interactions between pyramidal cells and interneurons organize the firing of the network into a high-frequency oscillation (80-250 Hz), or ripple, which is thought to increase its impact on downstream brain networks (Siapas and Wilson, 1998, Wierzynski et al., 2009, Stark et al., 2014). Interestingly, the neurons that participate in these bursts often "replay" previously experienced spatial trajectories (Wilson and McNaughton, 1994). In addition, previous work in anesthetized rats suggested that the CA3 bursts can feedback to the dentate gyrus (DG) and depolarize granule cells (Penttonen et al., 1997). Similarly, the CA1 burst is inherited by the entorhinal cortex (EC) and associated areas (Chrobak and Buzsaki, 1996), which could potentially provide excitatory input to granule cells as well. However, which of these two pathways provides the major source of excitation to the dentate gyrus during SWRs remains an open question.

In addition to SWRs, brief ($\sim$20 ms), large-amplitude ($>$ 1mV) positive waves can be observed in the LFP of the dentate hilus during quiet wakefulness and slow wave sleep, and have been termed dentate spikes (Bragin et al., 1995). Because these events are associated with current sinks in the dentate molecular layer and their incidence decreases after entorhinal lesions, they are likely generated by a population burst in the entorhinal cortex (Bragin et al., 1995, Penttonen et al., 1997). Consistent with this, previous work in anesthetized rats has demonstrated that granule cells often depolarize during DSs (Penttonen

et al., 1997). Interestingly, despite providing strong excitatory drive to the dentate gyrus, DSs are often associated with decreased activity in the CA1-CA3 network. Specifically, it was reported that SWRs rarely followed DSs within 200 ms, but that SWR-associated activity in CA1 often preceded DSs by ∼100 ms (Bragin et al., 1995). Because of this, the authors hypothesized that one function of DSs may be to delay the occurrence of SWRs by providing a suppressive effect on the excitability on the CA3-CA1 network (Bragin et al., 1995, Penttonen et al., 1997). However, these analyses were based on relatively few DSs and may have missed subtle interactions between these two events. Therefore, whether there are coordinated interactions between SWRs and DSs remains unresolved.

In order to address these questions, we combined whole-cell recordings from identified dentate granule cells with simultaneous LFP measurements from a nearby multisite silicon probe in awake, head-fixed mice that were free to walk on a spherical treadmill (Figure 24 A-C). Using this approach, we found that granule cells often depolarize during and ∼100 ms before SWRs, primarily driven by feedback excitation from CA3. Similarly, DSs occur at significantly higher rates during and ∼100 ms before SWRs, but these do not contribute to the SWR-associated depolarization of granule cells on average. Finally, we provide evidence that a subset of DSs may prime the hippocampal formation for SWR generation.

4.3 Results

During periods of quiet wakefulness, ripple oscillations were commonly observed in the CA1 pyramidal cell layer and DSs were observed in the hilus. Figure 24 D shows four 1-second periods of data during which SWRs and DSs co-occurred. Granule cells often showed large depolarizations concomitant with dentate LFP spikes. In comparison, the

Figure 24: Simultaneous extracellular and intracellular recording of dentate spikes and sharp-wave/ripples **(A)** Schematic of a mouse on the spherical treadmill. The approximate whole-cell (red dot) and LFP (black dot) recording locations are marked over dorsal hippocampus (blue). **(B)** Fluorescent image of 100 μm thick coronal section of dorsal hippocampus with two stained dentate granule cells (green) and immunohistochemistry against calbindin (gray) illustrating the placement of the multisite silicon probe and patch pipette. The scale bar is 500 μm. **(C)** Confocal images showing four biocytin stained dentate granule cells (green/magenta) with combined immunohistochemistry against parvalbumin (red; left image only) and calbindin (gray). The scale bar is 100 μm. **(D)** Four 1-second examples of multisite LFP (black) and simultaneous intracellular (blue) recordings during periods when ripples and DS co-occur. Membrane potential traces are from a dentate granule cell. The location of the CA1 pyramidal cell layer is marked by the red circle and dentate granule cell layer by the blue circle. Blue and red ticks below the LFP traces mark the occurrence of dentate spikes and CA1 ripples, respectively. LFPs come from 18 channels spanning the hippocampal formation.

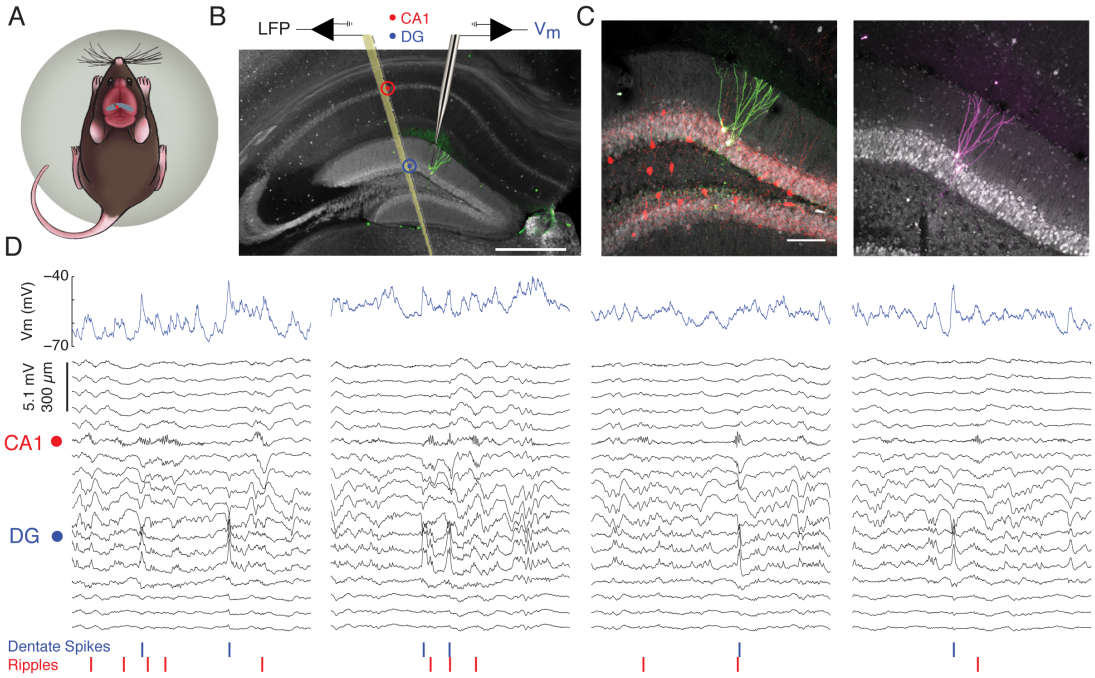

membrane potential dynamics of granule cells during SWRs were more diverse and harder to identify by looking at single SWRs. To address this, we triggered the Vm of granule cells on ripples detected in the CA1 pyramidal cell layer. The largest peak in the ripple-band LFP was used as time 0, and all times are reported relative to this point. As shown in Figure 25 A, the average granule cell response was composed of two depolarizations: one that occurred during the ripple (peak at -2.5 ms) and one that preceded the ripple by 102.5 ms. These two depolarizations could be observed in many single-neuron averages ($\sim$7 of 20 GCs) and appeared during a large fraction of single-ripples (Figure 25 A, top panel). What is driving these depolarizations? A previous intracellular study performed in anaesthetized rats reported that granule cells depolarized during SWRs and suggested this may be due to excitatory feedback from CA3 to granule cells (Penttonen et al., 1997). Similarly, this may also explain the depolarization we observe during the SWR.

The preceding depolarization, occurring approximately 100 ms before the SWR, was not reported in anesthetized animals and may therefore be specific to non-anesthetized animals. What is driving this depolarization? SWRs rarely occur in isolation. Instead, trains of sharp waves occur rhythmically at $\sim$8-10 Hz and are occasionally accompanied by a ripple oscillation in CA1. Such sharp wave trains are likely driven by rhythmic population bursts nucleated in the recurrent CA3 network, which may also provide feedback excitation to granule cells. If rhythmic population bursts in CA3 do contribute to the depolarization 100 ms before the SWR, then we should observe LFP sharp waves in CA1 that occur approximately 100 ms before the ripple as well. Indeed, as shown in Figure 25 B, sharp waves consistently preceded ripples by $\sim$100 ms. If rhythmic population bursts contribute to the peak at -100 ms, why isn't there a prominent third peak 100 ms after

Figure 25: Dentate granule cells depolarize during and 100 ms before CA1 ripples **(A)** Top: Ripple-triggered subthreshold Vm of granule cells. Each row is normalized to have zero mean (Vm Norm). Data are from 20 granule cells recorded in 8 mice. The largest peak in the LFP ripple was used as time 0. White lines on the right separate the different neurons. Bottom: Grand-average, ripple-triggered subthreshold Vm. Shaded region marks the mean±SEM. Note the two peaks in the Vm: one at -102.5 ms and one at -2.5 ms. Note also that the two peaks occur for many single-neurons and during a large fraction of ripples, as evidenced by the two yellow bands in the top panel. **(B)** Top: Ripple-triggered LFP from CA1 stratum radiatum showing the occurrence of sharp waves around the ripple. Data are from 19 mice, including the 8 used for granule cell intracellular experiments in A. White lines on the right separate the different mice. Bottom: Grand-average, ripple-triggered LFP. Note the two troughs in the LFP: one at -122.6 ms and one at 5.6 ms. A third, smaller trough can be seen at 144.3 ms. Note also that rhythmic sharp waves appear for nearly every mouse and for a majority of ripples, similar to the double peak in the granule cell Vm from A.

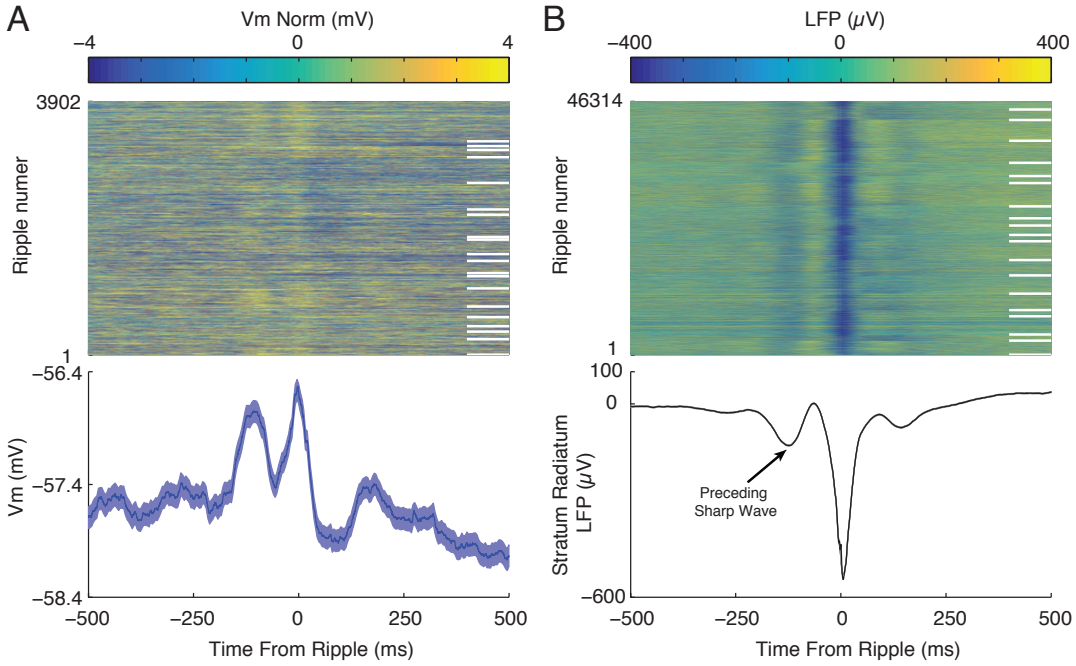

the ripple? One potential answer is that SWRs produce a long-lasting hyperpolarization that is likely responsible for terminating the population burst and may create a refractory period for SWR generation (English et al., 2014, Hulse et al., 2016), which may explain the absence of another prominent depolarization ∼100 ms after the ripple. However, it should be noted that there appears to be a much smaller depolarization and concomitant sharp wave ∼140 ms after the ripple, though their amplitudes are small. Together, these results provide circumstantial evidence that rhythmic population bursts nucleated in CA3 provide excitatory input to granule cells during quiet wakefulness.

Previous studies have suggested that SWRs and DSs rarely co-occur and that one function of DSs may be to delay the occurrence of SWRs by providing a suppressive effect on the excitability on the CA3-CA1 network (Bragin et al., 1995, Penttonen et al., 1997). Specifically, it was reported that SWR-associated activity in CA1 often preceded DSs by ∼100 ms, but that SWRs rarely followed DS within 200 ms (Bragin et al., 1995). In our raw data, we observed instances where SWRs and DSs co-occurred (Figure 24 D), raising the possibility that there may be coordinated temporal interactions between the two events. To address this, we plotted the timing of DSs around ripples and computed the average DS rate triggered on ripples (Figure 26 A). Surprisingly, the DS rate showed two large peaks: one at -101.4 ms and one at 3.3 ms, suggesting that DSs can co-occur with or precede SWRs by ∼100 ms. The double peak in the ripple-triggered DS rate could be observed for 16 of 19 mice. And for all 19 mice, the average DS rate was larger around the first and second peaks than away from ripples (Figure 26 B1-B2). To assess the precise timing between SWRs and DSs, we plotted histograms of when the peaks in the DS rate occurred for each mouse (Figure 26 C). Across mice, the first peak occurred at -101.1±3.8 ms and the second

at 5.3±1.6 ms. The timing of these peaks in the ripple-triggered DS rate nearly coincided with the timing of the two intracellular depolarizations (Figure 25 A), suggesting that, in addition to feedback excitation from CA3, DSs may also contribute to the intracellular depolarizations. If this were the case, then triggering the Vm on ripples that occur in the absence of dentate spikes should reduce the size of the two depolarizations. In contrast, we observed that the amplitude of the two depolarizations was not affected by the absence of overlapping DSs (data not shown), suggesting that DSs do not appreciably contribute to the average granule cell Vm around SWRs. This suggests that area CA3 provides the main excitatory input to granule cells during SWRs.

What is responsible for the large increase in the DS rate around ripples, and how often do DSs and SWRs co-occur? Over all 46,314 ripples, 3,970 (8.6%) were either preceded by, or occurred during, a dentate spike (Figure 26 D). A previous study provided evidence that SWRs occasionally precede DSs, and suggested that the SWR-associated population bursts in entorhinal cortex may excite the dentate gyrus and generate a DS (Bragin et al., 1995). While the delay they report (∼100 ms) is larger than what we observe (5.3 ms), it is still conceivable that the increase in the DS rate during ripples is driven by a SWR-associated population burst in entorhinal cortex. What then is responsible for the tendency of DSs to precede SWRs by 100 ms? It is well known that ripples occasionally occur as doublets, with one ripple preceding the other by ∼100 ms, which could potentially explain the first peak in the DS rate. This predicts that all DSs contributing to the peak at -100 ms should be accompanied by a SWR. To test this, we divided ripples into 6 mutually exclusive categories depending on whether a dentate spike occurred preceding or during the ripple, and whether the ripples or DSs occurred alone or as a doublet, as diagramed in the

Figure 26: Coordinated interactions between hippocampal ripples and dentate LFP spikes
(Continued on following page)

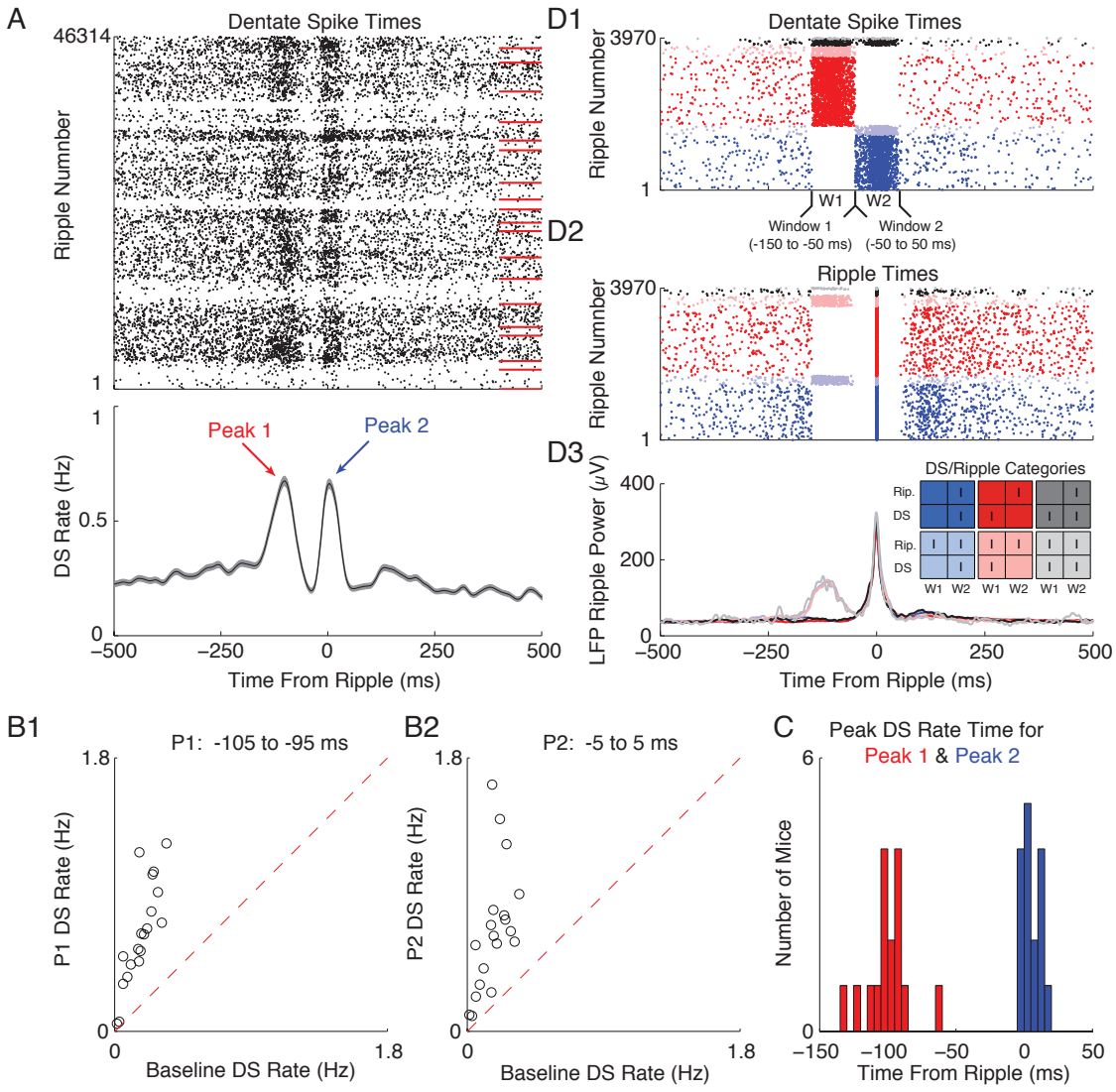

Figure 26: **(A)** Top: Ripple-triggered raster plot of dentate spike times. Red lines to the right separate the different mice. Data come from same 19 mice as in Figure 25 B. Bottom: Grand-average, ripple-triggered dentate spike rate. DS rate was computed by smoothing the DS times with a Gaussian (σ=10 ms). Note the two peaks in the DS rate: one at -101.4 ms and one at 3.3 ms. **(B1)** Scatter plot between baseline DS rate and average DS rate during the first peak (-105 to -95 ms). Each point comes from a single mouse. The baseline DS rate was computed as the average rate from -1000 to -250 ms and 250 ms to 1000 ms, which excludes periods containing the two peaks. **(B2)** Same as in B1, but for the second peak (-5 to 5 ms). **(C)** Distribution of peak times across mice. Data come from 16 out of 19 mice with clear double peaks in their ripple-triggered DS rate. Red bars are a histogram of the first peak (5.3±1.6 ms; mean±SEM). Blue bars are a histogram of the second peak (-101.1±3.8 ms). **(D1)** Ripple-triggered raster plot of dentate spike times. For D1-D3, only ripples (n=3,970 of 46,314) with a preceding DS (from -150 to -50 ms, Window 1) or simultaneous DS (from -50 to 50 ms, Window 2) were considered, as these are the DSs that produce the double peak in the DS rate, shown in A. Next, these 3,970 ripples were divided into 6 categories depending on whether a dentate spike occurred preceding (in W1) or simultaneously (in W2) with the ripple, and whether the ripples or DS occurred alone or as a doublet, as diagramed in the inset of panel D3. For example, ripples that occurred with a simultaneous DS (in W2), but without a preceding DS or ripple (in W1), are colored blue. Similarly, ripples that occurred with a preceding DS (in W1), but without a simultaneous DS (in W2) or preceding ripple (in W1) are colored dark blue. **(D2)** Ripple-triggered raster plot of ripple times, colored according to inset of panel D3. **(D3)** Ripple-triggered, ripple-band LFP power from the channel in the CA1 pyramidal cell layer, colored according to the inset showing the six DS/ripple categories. Note that most ripples with DSs are either preceded by a DS (n=1,818 of 3,970; red) or occur nearly simultaneous with a DS (n=1,433 of 3,970; blue), without ripple doublets or DS doublets. Note also that single ripples are not accompanied by an increase in the ripple-band LFP power around -100 ms, suggesting that the ripple detection did not miss ripples in this window.

Figure 27: Granule cells depolarize during dentate LFP spikes **(A)** Top: DS-triggered subthreshold Vm of granule cells. Each row is normalized to have zero mean (Vm Norm). Data are from 20 granule cells recorded in 8 mice. The largest peak in the DS was used as time 0. White lines on the right separate the different neurons. Middle: Grand-average, DS-triggered subthreshold Vm. Bottom: Grand-average, DS-triggered LFP from a channel in the dentate hilus, used for DS detection. Shaded region marks the mean±SEM. **(B)** Examples of DS-triggered subthreshold Vm for five individual granule cells. Note that every neuron shows a depolarizing peak at time 0, while most show a hyperpolarization preceding the DS. **(C)** Scatter plot showing the correlation between baseline Vm and the amplitude of the intracellular depolarization. For each neuron's DS-triggered average (as in B), the baseline Vm was computed as the mean from -300 to -200 ms. The amplitude of the peak was computed as the difference between the Vm at the peak (around time 0) and the baseline Vm. Each dot is a granule cell. Note that more hyperpolarized granule cells had a larger intracellular depolarization, consistent with excitatory input.

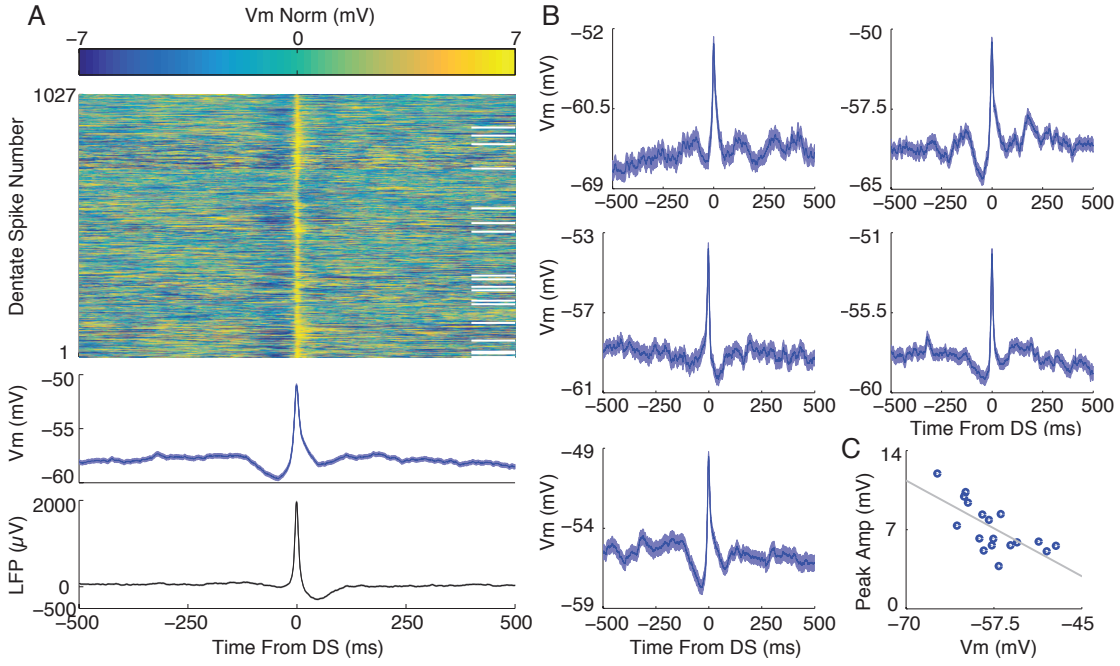

inset of Figure 26 D3. Interestingly, DSs that preceded SWRs by ∼100 ms occurred in the absence of ripple doublets greater than 86% of the time. This strongly argues against the prediction that the peak in the DS rate 100 ms before the SWR is driven by ripple doublets. Instead, it suggests that these DS, which may result from neocortical input to the entorhinal cortex, may somehow prime the CA3-CA1 network to generate a SWR with a 100 ms delay. Alternatively, the population burst in CA3 that often precedes ripples by 100 ms (Figure 25) may somehow influence the occurrence of DSs without producing a population burst in CA1 through some unknown mechanism.

While dentate spikes did not appreciably contribute to the two depolarizations in the granule cell Vm around SWRs, dentate spike may still powerfully drive granule cells. To investigate this possibility, we triggered the granule cell Vm on DSs. As shown in Figure 27 A-B, DSs were associated with a large and consistent depolarization in all granule cells. In addition, most granule cells showed a hyperpolarization beginning 100 ms before the dentate spike. In agreement with previous studies (Penttonen et al., 1997), the amplitude of the intracellular depolarization was larger at more hyperpolarized levels (Figure 27 C), providing evidence that the depolarization is driven by excitatory synaptic input. Together, these results provide evidence that granule cells receive strong excitatory input during DSs, likely producing a population burst in the dentate gyrus.

4.4 Discussion

By performing simultaneous in vivo whole-cell recordings from identified dentate granule cells and multisite LFP measurements, we investigated the interaction between SWRs and DSs and their effect on the membrane potential of granule cells and found: 1) granule

cells often depolarize during and ∼100 ms before ripple oscillations, concomitant with CA1 sharp waves, 2) DSs preferentially occur during and ∼100 ms before SWRs, but these do not appreciably contribute to the SWR-associated depolarizations in granule cells, 3) a subset of DSs precede CA1 ripples by 100 ms, in the absence of a ripple doublet, and 4) granule cells show large, consistent intracellular depolarizations during DSs.

What is driving the two depolarizations in granule cells around SWRs (Figure 25)? Previous experiments reported that granule cells depolarized during SWRs and suggested this was due to excitatory feedback from CA3 to the dentate gyrus (Penttonen et al., 1997). This may also explain the depolarization we observe during the SWR. Alternatively, the SWR-associated burst in entorhinal could also provide depolarizing input to granule cells. Indeed, DSs, which are thought to reflect excitatory input from entorhinal cortex, preferentially occur during SWRs (Figure 26). However, excluding SWRs with concomitant DSs had no affect on the amplitude of the intracellular depolarization. This strongly suggests that the depolarization is driven by feedback excitation from CA3 to the DG. What is driving the depolarization at -100 ms? Our observation that sharp waves often occur in trains, as demonstrated by the presence of a sharp wave ∼100 ms before the ripple argues that this depolarization is also driven by feedback excitation from CA3 to DG. Together, these results provide evidence that area CA3 provides the major excitatory drive to granule cells during SWRs. The functional role of such input remains an open question, but it has been suggested that CA3 and dentate may constitute a recurrent network that contributes to memory storage and recall (Lisman, 1999).

Why do DSs occasionally co-occur with SWRs (Figure 26)? A previous study provided evidence that SWR-associated activity in CA1 often preceded DSs by ∼100 ms (Bragin et

al., 1995). While this delay is larger than what we observe (5.3 ms), both studies found that DS occasionally following SWRs. Two possible mechanisms were suggested to underlie this (Bragin et al., 1995). First, a SWR-associated population burst in EC could provide the excitatory drive to trigger a DS. However, a previous study found that neurons in layer II of medial EC, which carry the excitatory projections to granule cells, do not undergo SWR-associated population bursts (Chrobak and Buzsaki, 1994, Chrobak and Buzsaki, 1996). If this is the case, then the population bursts in EC would have to reach the dentate gyrus through other pathways, such as the lateral EC. Second, it was also suggested that the long-lasting, post-ripple hyperpolarization in CA3 may reduce the excitatory drive to dentate hilus interneurons and create favorable conditions for the generation of a DS. However, given the small delay we observe between SWRs and DSs (5.3 ms), this mechanism seems unlikely. In addition, an extra-hippocampal region, such as the medial septum, could be responsible for coordinating the two events. Future work is needed to investigate these competing hypotheses.

Why do DSs occasionally occur 100 ms before SWRs (Figure 26)? One possibility is that these DSs occur as part of a ripple doublet. However, we found that when DSs preceded SWRs by ∼100 ms, they occurred without ripple doublets 86% of the time, which provides strong evidence that the peak in the DS rate at -100 ms is not driven by preceding ripples. In further support of this, these DSs also occurred without an increased in ripple-band LFP power (Figure 26 D), indicating the absence of CA1 ripples all together. Instead, it suggests that these DS may somehow prime the CA3-CA1 network to generate a SWR with a delay of 100 ms. Alternatively, the population bursts in CA3 that often precede ripples by 100 ms (Figure 25) may somehow influence the occurrence of DSs without producing a population

burst in CA1 through some unknown mechanism. Future work is needed to distinguish these possibilities. Such coordinated interactions between DSs and SWRs question the previously proposed functional role of DSs in hippocampal circuit function.

4.5 Experimental Procedures

All surgical procedures, in vivo recordings, signal acquisition, immunohistochemistry, imaging, and ripple detection were performed as detailed in Chapters 2 and 3. Dentate spikes were detected from 3 channels spanning the dentate hilus as peaks greater than 1 mV after downsampling (from 25 kHz to 1kHz) and high-pass filtering (Parks-McClellan optimal equiripple FIR filter, 6-12 Hz transition band, 40 dB minimum attenuation in the stop band) the LFPs. Previous work defined two types of dentate spikes by the presence or absence of associated gamma-band oscillations (Bragin et al., 1995). In agreement, we found that dentate spikes could occur with varying amounts of gamma-band activity. However, they did not cluster into two well-isolated classes, so we did not break them into types. Whole-cell recording data comes from 20 identified granule cells in 8 mice, from which we detected 3,902 ripples and 1,027 DSs (Figures 24 D, 25 A, and 27). For detecting interactions between the timing of DSs and SWRs (Figures 25 B and 26), we analyzed continuously recorded LFP data from 19 mice (including the 8 mice used for DG whole-cell recordings), from which we detected 46,314 SWRs.

References

Alger, B. E. and Nicoll, R. A. (1982). Feed-forward dendritic inhibition in rat hippocampal pyramidal cells studied in vitro. J Physiol. 328, 105-23.

Andersen, P. 2007. The hippocampus book, Oxford ; New York, Oxford University Press.

Anderson, J. S., Carandini, M. and Ferster, D. (2000). Orientation tuning of input conductance, excitation, and inhibition in cat primary visual cortex. J Neurophysiol. 84, 909-26.

Bahner, F., Weiss, E. K., Birke, G., Maier, N., Schmitz, D., Rudolph, U., Frotscher, M., Traub, R. D., Both, M. and Draguhn, A. (2011). Cellular correlate of assembly formation in oscillating hippocampal networks in vitro. Proc Natl Acad Sci U S A. 108, E607-16.

Berens, P. (2009). CircStat: A MATLAB Toolbox for Circular Statistics. Journal of Statistical Software. 31, 1-21.

Bittner, K. C., Grienberger, C., Vaidya, S. P., Milstein, A. D., Macklin, J. J., Suh, J., Tonegawa, S. and Magee, J. C. (2015). Conjunctive input processing drives feature selectivity in hippocampal CA1 neurons. Nat Neurosci. 18, 1133-42.

Bliss, T. V. and Collingridge, G. L. (1993). A synaptic model of memory: long-term potentiation in the hippocampus. Nature. 361, 31-9.

Bragin, A., Jando, G., Nadasdy, Z., van Landeghem, M. and Buzsaki, G. (1995). Dentate EEG spikes and associated interneuronal population bursts in the hippocampal hilar region of the rat. J Neurophysiol. 73, 1691-705.

Buzsaki, G. (1984). Long-term changes of hippocampal sharp-waves following high frequency afferent activation. Brain Res. 300, 179-82.

Buzsaki, G. (1986). Hippocampal sharp waves: their origin and significance. Brain Res. 398, 242-52.

Buzsaki, G. (1989). Two-stage model of memory trace formation: a role for "noisy" brain states. Neuroscience. 31, 551-70.

Buzsaki, G. (2015). Hippocampal sharp wave-ripple: A cognitive biomarker for episodic memory and planning. Hippocampus.

Buzsaki, G., Anastassiou, C. A. and Koch, C. (2012). The origin of extracellular fields and currents–EEG, ECoG, LFP and spikes. Nat Rev Neurosci. 13, 407-20.

Buzsaki, G., Horvath, Z., Urioste, R., Hetke, J. and Wise, K. (1992). High-frequency network oscillation in the hippocampus. Science. 256, 1025-7.

Buzsaki, G., Leung, L. W. and Vanderwolf, C. H. (1983). Cellular bases of hippocampal EEG in the behaving rat. Brain Res. 287, 139-71.

Carr, M. F., Jadhav, S. P. and Frank, L. M. (2011). Hippocampal replay in the awake state: a potential substrate for memory consolidation and retrieval. Nat Neurosci. 14, 147-53.

Chiovini, B., Turi, G. F., Katona, G., Kaszas, A., Palfi, D., Maak, P., Szalay, G., Szabo, M. F., Szabo, G., Szadai, Z., et al. (2014). Dendritic spikes induce ripples in parvalbumin interneurons during hippocampal sharp waves. Neuron. 82, 908-24.

Chorev, E. and Brecht, M. (2012). In vivo dual intra- and extracellular recordings suggest bidirectional coupling between CA1 pyramidal neurons. Journal of neurophysiology. 108, 1584-93.

Chrobak, J. J. and Buzsaki, G. (1994). Selective activation of deep layer (V-VI) retrohippocampal cortical neurons during hippocampal sharp waves in the behaving rat. J Neurosci. 14, 6160-70.

Chrobak, J. J. and Buzsaki, G. (1996). High-frequency oscillations in the output networks of the hippocampal-entorhinal axis of the freely behaving rat. J Neurosci. 16, 3056-66.

Csicsvari, J., Hirase, H., Czurko, A., Mamiya, A. and Buzsaki, G. (1999). Oscillatory coupling of hippocampal pyramidal cells and interneurons in the behaving Rat. J Neurosci. 19, 274-87.

Csicsvari, J., Hirase, H., Mamiya, A. and Buzsaki, G. (2000). Ensemble patterns of hippocampal CA3-CA1 neurons during sharp wave-associated population events. Neuron. 28, 585-94.

Cutsuridis, V. and Taxidis, J. (2013). Deciphering the role of CA1 inhibitory circuits in sharp wave-ripple complexes. Front Syst Neurosci. 7, 13.

de Sa, V. R. and MacKay, D. J. C. (2001). Model fitting as an aid to bridge balancing in neuronal recording. Neurocomputing. 38, 1651-1656.

Deuchars, J. and Thomson, A. M. (1996). CA1 pyramid-pyramid connections in rat hippocampus in vitro: dual intracellular recordings with biocytin filling. Neuroscience. 74, 1009-18.

Diba, K. and Buzsaki, G. (2007). Forward and reverse hippocampal place-cell sequences during ripples. Nat Neurosci. 10, 1241-2.

Diekelmann, S. and Born, J. (2010). The memory function of sleep. Nat Rev Neurosci. 11, 114-26.

Domnisoru, C., Kinkhabwala, A. A. and Tank, D. W. (2013). Membrane potential dynamics of grid cells. Nature. 495, 199-204.

Draguhn, A., Traub, R. D., Schmitz, D. and Jefferys, J. G. (1998). Electrical coupling underlies high-frequency oscillations in the hippocampus in vitro. Nature. 394, 189-92.

Dutar, P. and Nicoll, R. A. (1988). Stimulation of phosphatidylinositol (PI) turnover may mediate the muscarinic suppression of the M-current in hippocampal pyramidal cells. Neurosci Lett. 85, 89-94.

Ego-Stengel, V. and Wilson, M. A. (2010). Disruption of ripple-associated hippocampal activity during rest impairs spatial learning in the rat. Hippocampus. 20, 1-10.

Einevoll, G. T., Kayser, C., Logothetis, N. K. and Panzeri, S. (2013). Modelling and analysis of local field potentials for studying the function of cortical circuits. Nat Rev Neurosci. 14, 770-85.

English, D. F., Peyrache, A., Stark, E., Roux, L., Vallentin, D., Long, M. A. and Buzsaki, G. (2014). Excitation and inhibition compete to control spiking during hippocampal ripples: intracellular study in behaving mice. J Neurosci. 34, 16509-17.

Epsztein, J., Brecht, M. and Lee, A. K. (2011). Intracellular determinants of hippocampal CA1 place and silent cell activity in a novel environment. Neuron. 70, 109-20.

Epsztein, J., Lee, A. K., Chorev, E. and Brecht, M. (2010). Impact of spikelets on hippocampal CA1 pyramidal cell activity during spatial exploration. Science (New York, N Y). 327, 474-7.

Foster, D. J. and Wilson, M. A. (2006). Reverse replay of behavioural sequences in hippocampal place cells during the awake state. Nature. 440, 680-3.

Freund, T. F. and Buzsaki, G. (1996). Interneurons of the hippocampus. Hippocampus. 6, 347-470.

Froudarakis, E., Berens, P., Ecker, A. S., Cotton, R. J., Sinz, F. H., Yatsenko, D., Saggau, P., Bethge, M. and Tolias, A. S. (2014). Population code in mouse V1 facilitates readout

of natural scenes through increased sparseness. Nat Neurosci. 17, 851-7.

Fuhrmann, F., Justus, D., Sosulina, L., Kaneko, H., Beutel, T., Friedrichs, D., Schoch, S., Schwarz, M. K., Fuhrmann, M. and Remy, S. (2015). Locomotion, Theta Oscillations, and the Speed-Correlated Firing of Hippocampal Neurons Are Controlled by a Medial Septal Glutamatergic Circuit. Neuron. 86, 1253-64.

Girardeau, G., Benchenane, K., Wiener, S. I., Buzsaki, G. and Zugaro, M. B. (2009). Selective suppression of hippocampal ripples impairs spatial memory. Nat Neurosci. 12, 1222-3.

Graves, A. R., Moore, S. J., Bloss, E. B., Mensh, B. D., Kath, W. L. and Spruston, N. (2012). Hippocampal pyramidal neurons comprise two distinct cell types that are countermodulated by metabotropic receptors. Neuron. 76, 776-89.

Grienberger, C., Chen, X. and Konnerth, A. (2014). NMDA receptor-dependent multidendrite Ca(2+) spikes required for hippocampal burst firing in vivo. Neuron. 81, 1274-81.

Gulyas, A. I. and Freund, T. T. (2015). Generation of physiological and pathological high frequency oscillations: the role of perisomatic inhibition in sharp-wave ripple and interictal spike generation. Curr Opin Neurobiol. 31, 26-32.

Hafting, T., Fyhn, M., Molden, S., Moser, M. B. and Moser, E. I. (2005). Microstructure of a spatial map in the entorhinal cortex. Nature. 436, 801-6.

Harris, K. D. and Thiele, A. (2011). Cortical state and attention. Nat Rev Neurosci. 12, 509-23.

Harvey, C. D., Collman, F., Dombeck, D. A. and Tank, D. W. (2009). Intracellular dynamics of hippocampal place cells during virtual navigation. Nature. 461, 941-6.

Hasselmo, M. E. (1999). Neuromodulation: acetylcholine and memory consolidation. Trends Cogn Sci. 3, 351-359.

Hasselmo, M. E. and McGaughy, J. (2004). High acetylcholine levels set circuit dynamics for attention and encoding and low acetylcholine levels set dynamics for consolidation. Prog Brain Res. 145, 207-31.

Holt, G. R. and Koch, C. (1999). Electrical interactions via the extracellular potential near cell bodies. J Comput Neurosci. 6, 169-84.

Horikawa, K. and Armstrong, W. E. (1988). A versatile means of intracellular labeling: injection of biocytin and its detection with avidin conjugates. J Neurosci Methods. 25,

1-11.

Hu, H., Gan, J. and Jonas, P. (2014). Interneurons. Fast-spiking, parvalbumin(+) GABAergic interneurons: from cellular design to microcircuit function. Science. 345, 1255263.

Hulse, B. K., Moreaux, L. C., Lubenov, E. V. and Siapas, A. G. (2016). Membrane Potential Dynamics of CA1 Pyramidal Neurons during Hippocampal Ripples in Awake Mice. Neuron. 89, 800-13.

Isaacson, J. S. and Scanziani, M. (2011). How inhibition shapes cortical activity. Neuron. 72, 231-43.

Jadhav, S. P., Kemere, C., German, P. W. and Frank, L. M. (2012). Awake hippocampal sharp-wave ripples support spatial memory. Science. 336, 1454-8.

Jarosiewicz, B., McNaughton, B. L. and Skaggs, W. E. (2002). Hippocampal population activity during the small-amplitude irregular activity state in the rat. J Neurosci. 22, 1373-84.

Jarosiewicz, B. and Skaggs, W. E. (2004). Level of arousal during the small irregular activity state in the rat hippocampal EEG. J Neurophysiol. 91, 2649-57.

Kalen, P., Rosegren, E., Lindvall, O. and Bjorklund, A. (1989). Hippocampal Noradrenaline and Serotonin Release over 24 Hours as Measured by the Dialysis Technique in Freely Moving Rats: Correlation to Behavioural Activity State, Effect of Handling and Tail-Pinch. Eur J Neurosci. 1, 181-188.

Kametani, H. and Kawamura, H. (1990). Alterations in acetylcholine release in the rat hippocampus during sleep-wakefulness detected by intracerebral dialysis. Life Sci. 47, 421-6.

Kamondi, A., Acsady, L. and Buzsaki, G. (1998). Dendritic spikes are enhanced by cooperative network activity in the intact hippocampus. J Neurosci. 18, 3919-28.

Kandel, E. R. and Spencer, W. A. (1961). Electrophysiology of Hippocampal Neurons .2. After-Potentials and Repetitive Firing. Journal of Neurophysiology. 24, 243-and.

Kandel, E. R., Spencer, W. A. and Brinley, F. J. (1961). Electrophysiology of Hippocampal Neurons .1. Sequential Invasion and Synaptic Organization. Journal of Neurophysiology. 24, 225-and.

Katona, L., Lapray, D., Viney, T. J., Oulhaj, A., Borhegyi, Z., Micklem, B. R., Klausberger, T. and Somogyi, P. (2014). Sleep and movement differentiates actions of two types

of somatostatin-expressing GABAergic interneuron in rat hippocampus. Neuron. 82, 872-86.

Kay, K., Sosa, M., Chung, J. E., Karlsson, M. P., Larkin, M. C. and Frank, L. M. (2016). A hippocampal network for spatial coding during immobility and sleep. Nature. 531, 185-90.

Klausberger, T., Magill, P. J., Marton, L. F., Roberts, J. D., Cobden, P. M., Buzsaki, G. and Somogyi, P. (2003). Brain-state- and cell-type-specific firing of hippocampal interneurons in vivo. Nature. 421, 844-8.

Klausberger, T., Marton, L. F., Baude, A., Roberts, J. D., Magill, P. J. and Somogyi, P. (2004). Spike timing of dendrite-targeting bistratified cells during hippocampal network oscillations in vivo. Nat Neurosci. 7, 41-7.

Kowalski, J., Gan, J., Jonas, P. and Pernia-Andrade, A. J. (2016). Intrinsic membrane properties determine hippocampal differential firing pattern in vivo in anesthetized rats. Hippocampus. 26, 668-82.

Lapray, D., Lasztoczi, B., Lagler, M., Viney, T. J., Katona, L., Valenti, O., Hartwich, K., Borhegyi, Z., Somogyi, P. and Klausberger, T. (2012). Behavior-dependent specialization of identified hippocampal interneurons. Nat Neurosci. 15, 1265-71.

Le Duigou, C., Simonnet, J., Telenczuk, M. T., Fricker, D. and Miles, R. (2014). Recurrent synapses and circuits in the CA3 region of the hippocampus: an associative network. Front Cell Neurosci. 7, 262.

Lee, A. K., Epsztein, J. and Brecht, M. (2009). Head-anchored whole-cell recordings in freely moving rats. Nat Protoc. 4, 385-92.

Lee, A. K., Manns, I. D., Sakmann, B. and Brecht, M. (2006). Whole-cell recordings in freely moving rats. Neuron. 51, 399-407.

Lee, A. K. and Wilson, M. A. (2002). Memory of sequential experience in the hippocampus during slow wave sleep. Neuron. 36, 1183-94.

Lee, D., Lin, B. J. and Lee, A. K. (2012). Hippocampal place fields emerge upon single-cell manipulation of excitability during behavior. Science. 337, 849-53.

Lee, S. H. and Dan, Y. (2012). Neuromodulation of brain states. Neuron. 76, 209-22.

Lee, S. H., Marchionni, I., Bezaire, M., Varga, C., Danielson, N., Lovett-Barron, M., Losonczy, A. and Soltesz, I. (2014). Parvalbumin-positive basket cells differentiate among hip-

pocampal pyramidal cells. Neuron. 82, 1129-44.

Lisman, J. E. (1999). Relating hippocampal circuitry to function: recall of memory sequences by reciprocal dentate-CA3 interactions. Neuron. 22, 233-42.

Logothetis, N. K., Eschenko, O., Murayama, Y., Augath, M., Steudel, T., Evrard, H. C., Besserve, M. and Oeltermann, A. (2012). Hippocampal-cortical interaction during periods of subcortical silence. Nature. 491, 547-53.

Loomis, A. L., Harvey, E. N. and Hobart, G. A. (1937). Cerebral states during sleep, as studied by human brain potentials. Journal of Experimental Psychology. 21, 127-144.

Lubenov, E. V. and Siapas, A. G. (2009). Hippocampal theta oscillations are travelling waves. Nature. 459, 534-9.

Maccaferri, G. and Dingledine, R. (2002). Control of feedforward dendritic inhibition by NMDA receptor-dependent spike timing in hippocampal interneurons. The Journal of neuroscience : the official journal of the Society for Neuroscience. 22, 5462-72.

Maier, N., Tejero-Cantero, A., Dorrn, A. L., Winterer, J., Beed, P. S., Morris, G., Kempter, R., Poulet, J. F., Leibold, C. and Schmitz, D. (2011). Coherent phasic excitation during hippocampal ripples. Neuron. 72, 137-52.

Mainen, Z. F. and Sejnowski, T. J. (1995). Reliability of spike timing in neocortical neurons. Science. 268, 1503-6.

Margrie, T. W., Brecht, M. and Sakmann, B. (2002). In vivo, low-resistance, whole-cell recordings from neurons in the anaesthetized and awake mammalian brain. Pflugers Arch. 444, 491-8.

Marr, D. (1971). Simple memory: a theory for archicortex. Philos Trans R Soc Lond B Biol Sci. 262, 23-81.

Marrosu, F., Portas, C., Mascia, M. S., Casu, M. A., Fa, M., Giagheddu, M., Imperato, A. and Gessa, G. L. (1995). Microdialysis measurement of cortical and hippocampal acetylcholine release during sleep-wake cycle in freely moving cats. Brain Res. 671, 329-32.

McGinley, M. J., David, S. V. and McCormick, D. A. (2015a). Cortical Membrane Potential Signature of Optimal States for Sensory Signal Detection. Neuron. 87, 179-92.

McGinley, M. J., Vinck, M., Reimer, J., Batista-Brito, R., Zagha, E., Cadwell, C. R., Tolias, A. S., Cardin, J. A. and McCormick, D. A. (2015b). Waking State: Rapid Variations

Modulate Neural and Behavioral Responses. Neuron. 87, 1143-61.

Mcnaughton, B. L. and Morris, R. G. M. (1987). Hippocampal Synaptic Enhancement and Information-Storage within a Distributed Memory System. Trends in Neurosciences. 10, 408-415.

Mcnaughton, B. L., Okeefe, J. and Barnes, C. A. (1983). The Stereotrode - a New Technique for Simultaneous Isolation of Several Single Units in the Central Nervous-System from Multiple Unit Records. Journal of Neuroscience Methods. 8, 391-397.

Megias, M., Emri, Z., Freund, T. F. and Gulyas, A. I. (2001). Total number and distribution of inhibitory and excitatory synapses on hippocampal CA1 pyramidal cells. Neuroscience. 102, 527-40.

Miles, R. and Wong, R. K. (1986). Excitatory synaptic interactions between CA3 neurones in the guinea-pig hippocampus. J Physiol. 373, 397-418.

Mizunuma, M., Norimoto, H., Tao, K., Egawa, T., Hanaoka, K., Sakaguchi, T., Hioki, H., Kaneko, T., Yamaguchi, S., Nagano, T., et al. (2014). Unbalanced excitability underlies offline reactivation of behaviorally activated neurons. Nat Neurosci. 17, 503-5.

Moruzzi, G. and Magoun, H. W. (1949). Brain stem reticular formation and activation of the EEG. Electroencephalogr Clin Neurophysiol. 1, 455-73.

Nunez, P. L. and Srinivasan, R. 2006. Electric fields of the brain : the neurophysics of EEG, Oxford ; New York, Oxford University Press.

O'Keefe, J. (1976). Place units in the hippocampus of the freely moving rat. Exp Neurol. 51, 78-109.

O'Keefe, J. and Dostrovsky, J. (1971). The hippocampus as a spatial map. Preliminary evidence from unit activity in the freely-moving rat. Brain Res. 34, 171-5.

O'Keefe, J. and Nadel, L. 1978. The hippocampus as a cognitive map, Oxford New York, Clarendon Press; Oxford University Press.

O'Neill, J., Senior, T. and Csicsvari, J. (2006). Place-selective firing of CA1 pyramidal cells during sharp wave/ripple network patterns in exploratory behavior. Neuron. 49, 143-55.

Olafsdottir, H. F., Carpenter, F. and Barry, C. (2016). Coordinated grid and place cell replay during rest. Nat Neurosci. 19, 792-4.

Park, S. P., Lopez-Rodriguez, F., Wilson, C. L., Maidment, N., Matsumoto, Y. and Engel, J., Jr. (1999). In vivo microdialysis measures of extracellular serotonin in the rat hippocampus during sleep-wakefulness. Brain Res. 833, 291-6.

Patel, J. (2015). Network mechanisms underlying the initiation and generation of sharp-wave-associated ripple oscillations. J Neurosci. 35, 2323-5.

Penttonen, M., Kamondi, A., Sik, A., Acsady, L. and Buzsaki, G. (1997). Feed-forward and feed-back activation of the dentate gyrus in vivo during dentate spikes and sharp wave bursts. Hippocampus. 7, 437-50.

Pernia-Andrade, A. J. and Jonas, P. (2014). Theta-gamma-modulated synaptic currents in hippocampal granule cells in vivo define a mechanism for network oscillations. Neuron. 81, 140-52.

Pinault, D. (1996). A novel single-cell staining procedure performed in vivo under electrophysiological control: morpho-functional features of juxtacellularly labeled thalamic cells and other central neurons with biocytin or Neurobiotin. J Neurosci Methods. 65, 113-36.

Polack, P. O., Friedman, J. and Golshani, P. (2013). Cellular mechanisms of brain state-dependent gain modulation in visual cortex. Nat Neurosci. 16, 1331-9.

Pouille, F., Marin-Burgin, A., Adesnik, H., Atallah, B. V. and Scanziani, M. (2009). Input normalization by global feedforward inhibition expands cortical dynamic range. Nat Neurosci. 12, 1577-85.

Pouille, F. and Scanziani, M. (2001). Enforcement of temporal fidelity in pyramidal cells by somatic feed-forward inhibition. Science. 293, 1159-63.

Poulet, J. F. and Petersen, C. C. (2008). Internal brain state regulates membrane potential synchrony in barrel cortex of behaving mice. Nature. 454, 881-5.

Reimer, J., Froudarakis, E., Cadwell, C. R., Yatsenko, D., Denfield, G. H. and Tolias, A. S. (2014). Pupil fluctuations track fast switching of cortical states during quiet wakefulness. Neuron. 84, 355-62.

Sakatani, T. and Isa, T. (2004). PC-based high-speed video-oculography for measuring rapid eye movements in mice. Neurosci Res. 49, 123-31.

Saper, C. B., Fuller, P. M., Pedersen, N. P., Lu, J. and Scammell, T. E. (2010). Sleep state switching. Neuron. 68, 1023-42.

Scharfman, H. E. (2007). The CA3 "backprojection" to the dentate gyrus. Prog Brain Res. 163, 627-37.

Schiemann, J., Puggioni, P., Dacre, J., Pelko, M., Domanski, A., van Rossum, M. C. and Duguid, I. (2015). Cellular mechanisms underlying behavioral state-dependent bidirectional modulation of motor cortex output. Cell Rep. 11, 1319-30.

Schmidt-Hieber, C. and Hausser, M. (2013). Cellular mechanisms of spatial navigation in the medial entorhinal cortex. Nat Neurosci. 16, 325-31.

Schmitz, D., Schuchmann, S., Fisahn, A., Draguhn, A., Buhl, E. H., Petrasch-Parwez, E., Dermietzel, R., Heinemann, U. and Traub, R. D. (2001). Axo-axonal coupling. a novel mechanism for ultrafast neuronal communication. Neuron. 31, 831-40.

Schomburg, E. W., Anastassiou, C. A., Buzsaki, G. and Koch, C. (2012). The spiking component of oscillatory extracellular potentials in the rat hippocampus. J Neurosci. 32, 11798-811.

Schramm, A. E., Marinazzo, D., Gener, T. and Graham, L. J. (2014). The Touch and Zap method for in vivo whole-cell patch recording of intrinsic and visual responses of cortical neurons and glial cells. PLoS One. 9, e97310.

Siapas, A. G. and Wilson, M. A. (1998). Coordinated interactions between hippocampal ripples and cortical spindles during slow-wave sleep. Neuron. 21, 1123-8.

Soltesz, I., Bourassa, J. and Deschenes, M. (1993). The behavior of mossy cells of the rat dentate gyrus during theta oscillations in vivo. Neuroscience. 57, 555-64.

Soltesz, I. and Deschenes, M. (1993). Low- and high-frequency membrane potential oscillations during theta activity in CA1 and CA3 pyramidal neurons of the rat hippocampus under ketamine-xylazine anesthesia. J Neurophysiol. 70, 97-116.

Somogyi, P., Katona, L., Klausberger, T., Lasztoczi, B. and Viney, T. J. (2014). Temporal redistribution of inhibition over neuronal subcellular domains underlies state-dependent rhythmic change of excitability in the hippocampus. Philos Trans R Soc Lond B Biol Sci. 369, 20120518.

Spencer, W. A. and Kandel, E. R. (1961a). Electrophysiology of Hippocampal Neurons .3. Firing Level and Time Constant. Journal of Neurophysiology. 24, 260-and.

Spencer, W. A. and Kandel, E. R. (1961b). Electrophysiology of Hippocampal Neurons .4. Fast Prepotentials. Journal of Neurophysiology. 24, 272-and.

Spencer, W. A. and Kandel, E. R. (1961c). Electrophysiology of Hippocampal Neurons: Iv. Fast Prepotentials. J Neurophysiol. 24, 272-85.

Squire, L. R. (1992). Memory and the hippocampus: a synthesis from findings with rats, monkeys, and humans. Psychol Rev. 99, 195-231.

Stark, E., Roux, L., Eichler, R., Senzai, Y., Royer, S. and Buzsaki, G. (2014). Pyramidal cell-interneuron interactions underlie hippocampal ripple oscillations. Neuron. 83, 467-80.

Steriade, M., Timofeev, I. and Grenier, F. (2001). Natural waking and sleep states: a view from inside neocortical neurons. J Neurophysiol. 85, 1969-85.

Sullivan, D., Csicsvari, J., Mizuseki, K., Montgomery, S., Diba, K. and Buzsaki, G. (2011). Relationships between hippocampal sharp waves, ripples, and fast gamma oscillation: influence of dentate and entorhinal cortical activity. J Neurosci. 31, 8605-16.

Teles-Grilo Ruivo, L. M. and Mellor, J. R. (2013). Cholinergic modulation of hippocampal network function. Front Synaptic Neurosci. 5, 2.

Traub, R. D. and Bibbig, A. (2000). A model of high-frequency ripples in the hippocampus based on synaptic coupling plus axon-axon gap junctions between pyramidal neurons. J Neurosci. 20, 2086-93.

Ulrich, D. and Bettler, B. (2007). GABA(B) receptors: synaptic functions and mechanisms of diversity. Curr Opin Neurobiol. 17, 298-303.

Valero, M., Cid, E., Averkin, R. G., Aguilar, J., Sanchez-Aguilera, A., Viney, T. J., Gomez-Dominguez, D., Bellistri, E. and de la Prida, L. M. (2015). Determinants of different deep and superficial CA1 pyramidal cell dynamics during sharp-wave ripples. Nat Neurosci. 18, 1281-90.

Vanderwolf, C. H. (1969). Hippocampal electrical activity and voluntary movement in the rat. Electroencephalogr Clin Neurophysiol. 26, 407-18.

Vanderwolf, C. H. (1971). Limbic-diencephalic mechanisms of voluntary movement. Psychol Rev. 78, 83-113.

Varga, C., Golshani, P. and Soltesz, I. (2012). Frequency-invariant temporal ordering of interneuronal discharges during hippocampal oscillations in awake mice. Proc Natl Acad Sci U S A. 109, E2726-34.

Varga, C., Oijala, M., Lish, J., Szabo, G. G., Bezaire, M., Marchionni, I., Golshani, P. and Soltesz, I. (2014). Functional fission of parvalbumin interneuron classes during fast network

events. Elife. 3.

Vyazovskiy, V. V., Olcese, U., Hanlon, E. C., Nir, Y., Cirelli, C. and Tononi, G. (2011). Local sleep in awake rats. Nature. 472, 443-7.

Wang, D. V., Yau, H. J., Broker, C. J., Tsou, J. H., Bonci, A. and Ikemoto, S. (2015). Mesopontine median raphe regulates hippocampal ripple oscillation and memory consolidation. Nat Neurosci.

Wierzynski, C. M., Lubenov, E. V., Gu, M. and Siapas, A. G. (2009). State-dependent spike-timing relationships between hippocampal and prefrontal circuits during sleep. Neuron. 61, 587-96.

Wilson, M. A. and Mcnaughton, B. L. (1994a). Dynamics of the Hippocampal Ensemble Code for Space (Vol 261, Pg 1055, 1993). Science. 264, 16-16.

Wilson, M. A. and McNaughton, B. L. (1994b). Reactivation of hippocampal ensemble memories during sleep. Science. 265, 676-9.

Winson, J. and Abzug, C. (1977). Gating of neuronal transmission in the hippocampus: efficacy of transmission varies with behavioral state. Science. 196, 1223-5.

Winson, J. and Abzug, C. (1978). Dependence upon behavior of neuronal transmission from perforant pathway through entorhinal cortex. Brain Res. 147, 422-7.

Yang, S., Yang, S., Moreira, T., Hoffman, G., Carlson, G. C., Bender, K. J., Alger, B. E. and Tang, C. M. (2014). Interlamellar CA1 network in the hippocampus. Proc Natl Acad Sci U S A. 111, 12919-24.

Ylinen, A., Bragin, A., Nadasdy, Z., Jando, G., Szabo, I., Sik, A. and Buzsaki, G. (1995). Sharp wave-associated high-frequency oscillation (200 Hz) in the intact hippocampus: network and intracellular mechanisms. J Neurosci. 15, 30-46.